# Ab initio Characterization of anharmonic materials

Ibrahim Buba Garba

SORBONNE UNIVERSITÉ

# THÈSE DE DOCTORAT
# DE SORBONNE UNIVERSITÉ

## Spécialité : Physique

École doctorale nº564: Physique en Île-de-France

réalisée

Institut de Minéralogie, de Physique des Matériaux et de Cosmochimie (IMPMC)

sous la direction de
Lorenzo PAULATTO

présentée par


# Ibrahim Buba GARBA


pour obtenir le grade de :

DOCTEUR DE SORBONNE UNIVERSITÉ

Sujet de la thèse :

# Caractérisation ab initio des materiaux anharmoniques

soutenue le 5/09/2023

devant le jury composé de :

| | | |
|---|---|---|
| M. | Marco Pala | Rapporteur |
| M. | Nicolas Horny | Rapporteur |
| Mme | Magali Benoit | Examinatrice |
| Mme | Nedjma Bendiab | Examinatrice |
| M. | Fabio Finocchi | Examinateur (président ) |
| M. | Francois Bottin | Invité |
| Mme | Giorgia Fugallo | Invitée |
| M. | Lorenzo Paulatto | Directeur de thèse |

# Contents

# List of Figures

# List of Tables

# 1 – Introduction

## 1.1 Significance of phonon anharmonicity in solids

Great effort is devoted to the study of thermal properties of materials with interesting applications in thermoelectricity, superconductivity, astrophysics, geoscience, electronics, and the aerospace industry. Theoretical models and computer simulation become useful in this regard, either to complement experimental efforts, where an experiment is possible, or to provide predictive insight where it is not. Density functional theory (DFT) [14] is one of the most powerful predictive methods used in exploring many properties of materials. It is based on quantum-mechanical laws, with the only required input information being the chemical composition and physical constants. However, DFT is a ground-state theory and therefore characterizes materials at 0 K and the effect of temperature on ionic motion is neglected.

Lattice Dynamics theory developed by Born and Huang [15] describes the effects of temperature in solids in terms of atomic vibrations within the crystal lattice. Thus, when combined with *ab initio* calculation like DFT, ab-initio lattice dynamics can be used as a powerful tool for a fundamental understanding of vibrational, thermodynamic, and transport properties of materials, without any empirical parameter [16].

The relationship between electronic and lattice-dynamical properties of materials within the DFT framework took off in the 1970s and has emerged as an important cornerstone of condensed matter physics to this day. Perhaps the first application of DFT to obtain phonon spectra and force constants (FCs) was by Walden and Martin in the late 70s, the so-called frozen phonon method [17]. Density functional perturbation theory (DFPT) is an alternative efficient technique for computing FCs by diagonalizing the dynamical matrix at an arbitrary reciprocal space point [18].

The simplest lattice model for computing phonon is the harmonic approximation (HA), in which the potential energy is expanded in Taylor series up to second order in powers of atomic displacements about their equilibrium positions. Thermal properties are derived from a system of non-interacting phonons, whose frequencies are independent of temperature.However, the small displacement assumption becomes invalid at high temperatures, especially near a phase transition, or even at low temperatures if the energy profile is shallow, or if the quantum nature of nuclei cannot be disregarded, which warrants the need for anharmonic methods. Furthermore, the perturbative treatment of anharmonicity can be problematic in the presence of imaginary phonons, i.e. harmonic approximation has no suitable ground state upon which a perturbative expansion can be built. Quasiharmonic approximation (QHA) is the simplest extension, where several harmonic calculation are performed as a function of an external parameter (i.e. volume) and the vibrational energy at

finite temperature taken into account [19, 20].

Although non-perturbative anharmonic lattice models, particularly the self-consistent phonon (SCP) theory, have been developed as early as the 1950s by Born and Hooton [21, 22] and others [23, 24], these models have originally been applied to rare gases, like Ne, with simple interaction potentials based on *ad hoc* parameters, thereby limiting their application and predictive power. Over the last two decades, there has been increasing interest in anharmonic methods based on density functional theory (DFT). These anharmonic approaches are non-perturbative and seek to build an *effective potential* at the temperature at which the potential energy surface (PES) is probed. While these methods are diverse in their formulation and implementation, they mainly differ on (i) the method of computing the forces acting on ions or force constants, and (ii) how the potential energy landscape of the nuclear dynamics is sampled. *Ab initio* molecular dynamics (AIMD) simulations sample the potential energy surface including full anharmonicity. In the latter framework, dynamical and transport properties can be computed as time averages over trajectories using either normal-mode analysis (NMA) [25, 26] or velocity autocorrelation function (VACF) method. NMA and VACF have the advantage that both renormalized phonon frequencies and phonon lifetime are obtained from AIMD non-perturbatively and without explicitly computing higher-order force constants. The main disadvantage of these methods is the long simulated time required to reach ergodicity and/or targeted frequency resolution. In the case particle exchange is relevant, an additional drawback is the lack of well-defined quantum statistics. Nevertheless, the efficiency of VACF can be substantially improved by projecting the atomic velocities (or displacements) of atoms in a supercell on harmonic phonons modes from DFT in a commensurate unit cell [27, 28]. Note that the displacement of the atoms associated with a mode only depend on symmetry.

The early contribution in the family of self-consistent phonon (SCP) methods was the self-consistent *ab initio* lattice dynamics (SCAILD) by Souvatzis *et al.* [29], which is based on thermal mean square displacements of atoms in a supercell. Roekeghem *et al.* [30, 31] extended SCAILD to QSCAILD, which uses a quantum mean square thermal displacement matrix. The temperature-dependent effective potential (TDEP) approach involves fitting force constants to *ab initio* DFT forces sampled along MD trajectories [32, 33] or stochastically [34]. Other SCP-based methods include SCPH proposed by Tadano *et al.* [10], where anharmonic frequencies are computed from the pole of the Green's function and higher order effective force constants from "compressive sensing" [35]. The vibrational self-consistent-field (VSCF) method that expand the Born-Oppenheimer PES using harmonic phonon basis [36]. Anharmonicity using special displacement method (A-SDM) [37]. The stochastic self-consistent harmonic approximation (SSCHA) [38] minimizes the free energy of a system within a harmonic density matrix ansatz, rigorously capturing both nuclear quantum effects (NQE) and anharmonicity. Anharmonic effects can also be sampled using a classical Langevin dynamics based on the algorithm by Bussi and Parrinello [39] and a recent path integral LD (PILD) scheme using classical and quantum correlators [6, 40]. In PILD, including NQE implies a significant expense due to the requirement to simulate many replicas of the system in parallel. Details of these methods are in the original articles of the authors and also in recent reviews by Esfarjani *et al.* [41], and Hong *et al.* [42].

## 1.2 Objectives and scope

The aim of the thesis is to develop an anharmonic non-perturbative method that works beyond the limits of the standard quasiharmonic approximation, where perturbation theory breaks down, and apply the method to study properties of technologically relevant materials where proper understanding and description of anharmonic effects at low, intermediate or high temperature is significant.

## 1.3 Organization of thesis

In Chapter 2, the theoretical framework based on first-principles density functional theory is derived from a detailed discussion of the electronic structure theory and the approximations necessary for obtaining the ground state properties of a crystalline solid. In Chapter 3, methods of simulating the dynamics of the nuclei at finite temperature are discussed, including molecular dynamics, Langevin dynamics, and lattice dynamics within harmonic approximation and beyond, as well as the algorithms employed in our calculation. For the last part of Chapter 3, Section 3.3.4 presents advanced methods developed over the years for studying anharmonic phonons, discussing their strengths and limitations.

An efficient method of computing anharmonic effects is developed and implemented in Chapter 4, which is based on the temperature-dependent effective potential (TDEP) technique proposed by Esfarjani et al. [32] and Hellman et al. [33]. Unlike TDEP, the temperature-dependent phonon (TDPH) method [43] uses the symmetry of the crystal to reduce the reciprocal-space $\mathbf{q}$-point sampling of phonons to its irreducible wedge and then, for each $\mathbf{q}$-point to reduce the dynamical matrix $D(\mathbf{q})$, to its irreducible representations, expressed as a basis of symmetric hermitian dynamical matrices. In Section 4.7, we performed extensive convergence tests using different thermodynamic ensembles (MD-NVE, MD-NVT, and LD). We showed how energy autocorrelation could be used to determine an appropriate sampling interval (decorrelation time) and demonstrated the robustness of the TDPH method against randomization of the initial guess of force constants.

In Chapter 5-7, the TDPH technique is applied to study anharmonic effects in technologically relevant materials, and where available, the results are compared to experimental measurements or other anharmonic phonon methods. Chapter 5 focuses on temperature-evolution of phonons and anharmonic correction to quasiharmonic free energy in fcc Al. Chapter 6 shows how the TDPH method gives renormalized phonons in entropy-stabilized high-temperature group IV bcc metals, with Zr as representative. Chapter 7 investigates phonon anharmonicity in $SrTiO_3$, a representative $ABO_3$ perovskite with an interesting phase diagram and many technological applications. In Section 7.3.4, we applied the Curie-Wess law to predict the cubic to tetragonal transition temperature, $T_c$, via linear fit to the temperature dependence of the soft antiferrodistortive mode. In Section 7.3.5, we built perturbation on the TDPH potential to compute phonon lifetimes and linewidths from the three-phonon scattering process and the lattice thermal conductivity of cubic $SrTiO_3$ using the Boltzmann transport equation (BTE) within the single-mode relaxation approximation.

Finally, Chapter 8 provides a summary of our main results, and proposes potential avenues for future research direction.

# 2 – Electronic Structure

## 2.1 The many-body problem

Consider a quantum solid system containing N electrons and M nuclei interacting with each other. One can characterize such a system by solving for stationary states of the time-independent many-body Schrödinger equation:

$$\hat{H}|\Psi\rangle = E|\Psi\rangle. \tag{2.1}$$

$|\Psi\rangle$ and $E$ are the eigenfunctions and the eigenvalues of the hamiltonian operator, $\hat{H}$, describing the kinetic energies (T) and the Coulomb interactions (V) between electrons and nuclei:

$$\begin{aligned}\hat{H} =& \ \hat{T}_n + \hat{T}_e + \hat{V}_{n-n} + \hat{V}_{e-e} + \hat{V}_{e-n} \\ =& -\sum_i^N \frac{{\nabla_i}^2}{2} - \sum_I^M \frac{{\nabla_I}^2}{2M_I} + \frac{1}{2}\sum_{i\neq j}^N \frac{1}{|\mathbf{r}_i - \mathbf{r}_j|} + \frac{1}{2}\sum_{I\neq J}^M \frac{Z_I Z_J}{|\mathbf{R}_I - \mathbf{R}_J|} - \sum_{i,I} \frac{Z_I}{|\mathbf{r}_i - \mathbf{R}_I|}\end{aligned} \tag{2.2}$$

where in Eq. 2.2 above, we adopted atomic units i.e. $\frac{1}{4\pi\epsilon} = e = \hbar = m_e = 1$. The indices i,j and I,J run from 1 to $N$ (electrons) and 1 to $M$ (nuclei). $\mathbf{R}$ ($\mathbf{r}$) represent the position vector of nuclei (electrons) and $Z_I$ is atomic number of atom $I$.

The solution of Eq. 2.2 with the lowest energy, $\Psi_0$, corresponds to the ground state of the system, from which all equilibrium properties can be derived. However, solving this equation is impossible analytically (beyond diatomic He) and therefore one resort to approximations in an effort to simplify the problem.

## 2.2 Born-Oppenheimer approximation

Since electrons move much faster than nuclei owing to their small masses ( $M_I \approx 10^3\ m_e$) it is reasonable to decouple the motions of the electrons and the nuclei. This idea was first used by Marx Born and Robert Oppenhiemer in 1927 [44], it is known as the *Born-Oppenheimer* or *adiabatic approximation*.

Thus, instead of treating the nuclei and electrons on equal quantum mechanical footing, one can solve the electronic problem assuming the nuclei to be clamped (fixed): the many-body problem is reduced to solving the electronic problem in their ground state for a given

nuclear configuration.

$$\Psi(\mathbf{r},\mathbf{R}) = \sum_i \psi_i(\mathbf{R})\Phi_i(\mathbf{r},\mathbf{R}) \tag{2.3}$$

which give raise to decoupled SE for electrons and nuclei:

$$\left[\hat{T}_n + \hat{V}_{ion-ion} + E_i(\mathbf{R})\right]\psi_i(\mathbf{R}) = E_n\psi_i(\mathbf{R}) \tag{2.4}$$

$$\left[\hat{T}_e + \hat{V}_{e-e} + \hat{V}_{e-n}\right]\Phi_i(\mathbf{r},\mathbf{R}) = E_i(\mathbf{R})\Phi_i(\mathbf{r},\mathbf{R}) \tag{2.5}$$

where $\Phi_i(\mathbf{r},\mathbf{R})$ are the electronic states of the electrons at a given fixed nuclear configurations. The nuclei evolve in the *BO energy surface* which is the sum of the electronic ground state "*total energy*" at a particular nuclear coordinate and the nuclear-nuclear interaction : $E_{BO}(\mathbf{R}) = V_{n-n} + E(\mathbf{R})$. By fixing $\mathbf{R}$, $\hat{V}_{n-n}$ can be regarded as a shift on the electronic energy. Thus:

$$\hat{H}_{BO} = \hat{H}_e(\mathbf{r},\mathbf{R}) + \hat{V}_{n-n} \tag{2.6}$$

where $\hat{H}_e$ is given by Equation 2.5 above.

## 2.3 Density functional theory

Density functional theory (DFT) is an approximation method for solving many body Schrödinger equation where the Hamiltonian is expressed in terms of groundstate electron density, instead of wave function. DFT was originally initiated by Thomas [45] and Fermi [46] in 1927, where they expressed the kinetic energy as a functional of the electron density but neglected the exchange and correlation energy. Dirac [47] in 1930 extended the Thomas-Fermi theory by including the local exchange term. It was also reported that Kato in 1957 rigorously proved mathematically, that all parameters defining the Hamiltonian of a system can be expressed in terms of electron density. But it was W. Kohn and P. Hohenberg that developed the version of what is today known as density functional theory in two theorems. Later in 1965, Walter Kohn and his post-doc student L. J. Sham made DFT a practical tool based on the Kohn-sham equations. It is important to note that in DFT any property of a system is defined by the groundstate density $n_0(\mathbf{r})$. Today, many properties of atoms and molecules in condensed matter can be quantitatively calculated with remarkable accuracy. What made DFT particularly popular is the balance it provide between computational cost and accuracy.

### 2.3.1 Kohn-Hohenberg theorems

In 1964, Walter Kohn and P. Hohenberg made a remarkable contribution, in the form of two theorems, that revolutionize our understanding of condensed matter systems.

- Thorem 1: For a system of interacting particles, the ground state electronic density $n_0(\mathbf{r})$, uniquely determine the external potential of the system $V_{ext}(\mathbf{r})$, to within a cosnstant.

- Thorem 2: A functional of the energy $E[n(\mathbf{r})]$ can be defined in terms of the density $n(\mathbf{r})$ of the system. The ground state density $n(\mathbf{r})$ that minimizes the functional $E[n(\mathbf{r})]$ is the exact ground state density $n_0(\mathbf{r})$.

Based on these two theorems, the energy can be expressed as a functional of wavefunction using Eq. 2.5

$$\begin{aligned} E[n] &= \langle \Phi[n] \hat{T}_e \Phi[n] \rangle + \langle \Phi[n] \hat{V}_{e-e} \Phi[n] \rangle + \langle \Phi[n] \hat{V}_{ext} \Phi[n] \rangle \\ &= T[n] + V_{e-e}[n] + \int V_{ext}(\mathbf{r}) n \mathbf{r} d\mathbf{r} \\ &= F[n] + \int V_{ext}(\mathbf{r}) n \mathbf{r} d\mathbf{r} \end{aligned} \tag{2.7}$$

where we replaced $V_{e-ion}$ with $V_{ext}$, and defined the universal functional as $F[n] = T[n] + V_{e-e}[n]$. So far, we have not exactly stated how to get the density from the wave function, and the universal functional, $E[n]$, which is dependent on the electronic density $n(\mathbf{r})$, has no known form. The Kohn Sham equations handle these two problems.

### 2.3.2 Kohn-Sham equation

The main idea behind of Kohn-Sham equation is to replace the exact system of many-interacting electrons with an auxiliary system of non-interacting electrons in an effective potential $V_{KS}$, by assuming that the exact and the auxiliary system of non-interacting electrons have the same ground state. The KS equation can be expressed as:

$$\left[ -\frac{1}{2} {\nabla_i}^2 + V_{KS}(\mathbf{r}) \right] \phi_i(\mathbf{r}) = \varepsilon_i \phi_i(\mathbf{r}) \quad . \tag{2.8}$$

It is clear that Eq. 2.8 is another rendition of Eq. 2.5 with many-electron wavefunction replaced by single-particle orbitals $\phi_i$, $i = 1, 2, ..N$, and density

$$n(\mathbf{r}) = \sum_i |\phi_i|^2 \tag{2.9}$$

It follows that solving the non-interacting system gives the ground state density, which can subsequently be utilized to solve the exact problem. Next, we rewrite the functional defined in Eq. 2.7

$$E[n(\mathbf{r})] = T_0[n(\mathbf{r})] + E_H[n(r)] + E_{XC}[n(\mathbf{r})] + V_{ext}[n(\mathbf{r})] \tag{2.10}$$

where $T_0[n(\mathbf{r})]$ is the non-interacting kinetic energy o the auxiliary system, $E_H[n(r)]$ is the Hartree energy due to classical Coulombic interaction of electron density

$$E_H[n(r)] = \int \frac{n(\mathbf{r}) n(\mathbf{r}')}{|\mathbf{r} - \mathbf{r}'|} d\mathbf{r} d\mathbf{r}'$$

and $E_{XC}[n(\mathbf{r})]$ is the exchange-correlation energy added in order to make Equ. 2.10 formally exact. The effective or auxiliary potential of Equ. 2.8 can be found by minimizing Equ. 2.10 with respect to the Kohn-Sham states $\phi_i$ given an appropriate form of the exchange-correlation [48]:

$$\frac{T_0[n(\mathbf{r})]}{\delta \phi_i^*} + \left[ \frac{E_H[n(r)]}{\delta n(\mathbf{r})} + \frac{E_{XC}[n(\mathbf{r})]}{\delta n(\mathbf{r})} + \frac{V_{ext}[n(\mathbf{r})]}{\delta n(\mathbf{r})} \right] \frac{\delta n(\mathbf{r})}{\delta \phi_i^*}, \tag{2.11}$$

subject to:

$$\langle \phi_i | \phi_j \rangle = \delta_{ij}, \text{ and}$$

$$\frac{\delta T_0[n(\mathbf{r})]}{\delta \phi_i^*} = \frac{1}{2}\nabla_i^2 \phi_i$$
$$\frac{\delta n(\mathbf{r})}{\delta \phi_i^*} = \phi_i$$

yields the expression for the Kohn-Sham potential

$$V_{KS}(\mathbf{r}) = V_{ext}(\mathbf{r}) + V_H(\mathbf{r}) + V_{XC}(\mathbf{r}) \tag{2.12}$$

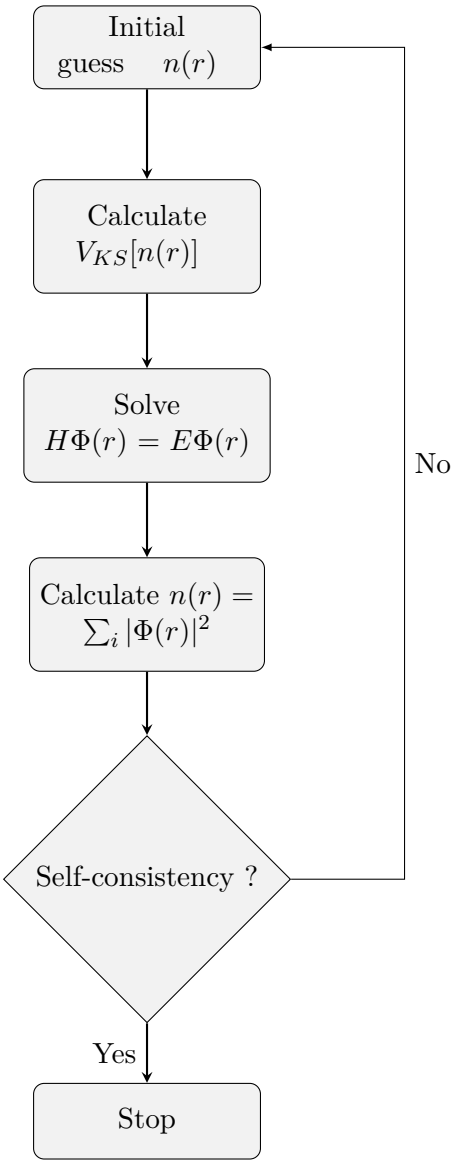


Figure 2.1: The Kohn-Sham self-consistency cycle in DFT calculation, like the Hartree-Fock approach, minimizes the system's electronic Hamiltonian. It starts with an estimate of electronic charge density and ends when the self-consistency requirement is satisfied ($n(\mathbf{r}) = n^*(\mathbf{r})$) within the pre-determined threshold.

### 2.3.3 Exchange-correlation functionals

No meaningful progress can be made with KS equation without the knowledge of the exchange correlation energy, $E_{XC}$, which accounts for all the corrections to the other exact terms in Equ. 2.10. The exact form of $E_{XC}$ is not known, and therefore must be approximated in order to use DFT as a complete theory. Ironically, the fact that $E_{XC}$ can be approximated is largely responsible for the success of DFT, but the approximation itself poses limitations.

The two most widely used approximations to $E_{XC}$ are Local density approximation (LDA) [49, 50] and Generalized gradient approximation (GGA) [51, 52].

#### Local density approximation

LDA assumes that the exchange-correlation energy at a point is equal to the exchange-correlation of a uniform electron gas (jellium) with the same density

$$E_{XC}^{LDA}(n(\mathbf{r})) \approx \int d\mathbf{r}\ n(\mathbf{r})\ \epsilon_{XC}[n(\mathbf{r})]\ , \tag{2.13}$$

where the quantity $\epsilon_{XC}[n(\mathbf{r})]$ is the exchange-correlation energy per electron and can be obtained from highly accurate Monte Carlo methods, with the most popular methods being that of Ceperley and Alder [53] and Perdew and Zunger [50].

#### Generalized gradient approximation

As the name implies, the generalized gradient approximation (GGA) assumes that the exchange-correlation functional cab be replaced by the local density and its gradient

$$E_{XC}^{GGA}(n(\mathbf{r})) \approx \int d\mathbf{r} n(\mathbf{r}) \epsilon_{XC}[n(\mathbf{r})] F_{XC}[n(\mathbf{r}, \nabla n(\mathbf{r}))]\ , \tag{2.14}$$

where $F_{XC}$ is the enhancement factor, which can be obtained with different schemes leading to different flavors of GGA. The most widely used GGA exchange-correlation functionals, and the ones used in this work, are PBE [54] and PBEsol [55].

Both LDA and GGA functionals have been found to be successful in predicting material properties, but have not been without limitations. For instance, LDA have been known to overestimate binding energy, leading to short bond lengths and compressed lattice parameters while GGA have the opposite effect. Also, both LDA and GGA underestimate the band gap of semiconductors especially in strongly correlated materials with partially occupied $d$ and $f$ orbitals that are localized.

The most common corrective methods to overcome these challenges include Hubbard-modeled corrections on DFT (DFT+U or historically LDA+U) [56, 57], dynamical mean field theory (DMFT) [58, 59] and other many-body techniques. DFT+U is particularly appealing because of its simplicity and direct access to the energy derivatives (forces and stress), and comparable computational cost to standard DFT [60]. Although it can obtained self-consistently [61, 60], the Hubbard U parameter is often chosen *semi-empirically* to match some experimental quantity, i.e. the electronic band gap, thus limiting the predictive power of DFT+U.

### 2.3.4 Plane-wave basis set

In order to solve the KS equations, an appropriate basis set to describe electronic wavefunctions must be chosen. A popular choice in the quantum chemistry community are the Gaussian basis functions, which are centered at the atomic positions. Plane wave basis set, which are periodic and delocalized in space, are commonly used in the solid-state physics community. The latter is employed in all DFT calculations performed in this thesis using the Quantum Espresso software. The underlying periodicity of the crystals implies that the KS orbitals can expressed, based on Bloch theorem

$$\psi_{i\mathbf{k}}(\mathbf{r}) = e^{i\mathbf{k}\cdot\mathbf{r}} u_{i\mathbf{k}}(\mathbf{r}) \tag{2.15}$$

where $u_{i\mathbf{k}}(\mathbf{r})$ has the periodicity of the cell, and it is given as:

$$u_{i\mathbf{k}}(\mathbf{r}) = \frac{1}{\sqrt{\Omega}} \sum_n c_{in}(\mathbf{k}) e^{i\mathbf{G}_n\cdot\mathbf{r}}. \tag{2.16}$$

$\Omega$ is the unit cell volume, $\mathbf{G}_n$ is the reciprocal lattice vector of the crystal, $k$ is the wave vector, $i$ is the electronic band index, and $c_{in}$ are expansion coefficients. In practice, the number of plane waves in the expansion of 2.15 at a given $\mathbf{k}$-point is determined by the cutoff off of the plane wave kinetic energy ($E_{cut}$), that satisfies

$$\frac{1}{2}|\mathbf{G} + \mathbf{k}|^2 < E_{cut} \tag{2.17}$$

### 2.3.5 Pseudopotential

Most physical properties of depends on outermost valence electrons of atoms and the core-electrons are environment-independent. The valence electrons wavefunctions oscillate rapidly within the core region, due to orthonalty with the wavefunctions of the core electrons. The pseudopotential theory attempts to replace the nuclear potential with an altered potential that provides smooth wavefunctions at the nuclear core while matching the original wavefunctions beyond a given radius.

# 3 – Dynamics of the Nuclei

## 3.1 Molecular Dynamics

Classical molecular dynamics integrate Newton's equation of motion (EOM) for an ensemble of point-like particles representing atoms in real materials. Once initial conditions are defined, such as the positions and velocities of particles, and a physical model that describes the interatomic interactions, the motion of atoms as a function of time is used to generate trajectory. Constraints, such as temperature (thermostats) or pressure (barostats), define how the phase space is sampled and, consequently, the macroscopic properties that can be extracted from the trajectory[62]. In contrast to the Phonon gas model, MD offers a more practical way to study the effects of temperature. Normal mode analysis (NMA) can be used to calculate the phonon density of states as a Fourier transform of the velocity autocorrelation, and the Green-Kubo theory can be employed to compute the thermal conductivity from the autocorrelation of the heat flux [63, 26]. However, the predictive power and transferability of interatomic potentials is constrained by the fact that they are either basic analytical functions, fitted to experiment, or parametrized using ab initio calculations[64]. Quantum or ab initio MD is a major advancement that follows Car and Parinello's unification of MD and DFT [65].

In molecular dynamics the simulation the aim is typically to explore the phase space $(\mathbf{p}, \mathbf{r})$ exhaustively so that the time average $\langle . \rangle_t$ approximately represented the ensemble average $\langle . \rangle_{(\mathbf{p},\mathbf{r})}$, for an observable $A(\mathbf{p}, \mathbf{r})$, i.e.

$$\langle A \rangle = \lim_{t\to\infty} \int_0^t A(t')dt' \approx \frac{1}{N_{steps}} \sum_{i=1}^{N_{steps}} A(\mathbf{p}(t_i), \mathbf{r}(t_i)) \ . \tag{3.1}$$

I.e. an integral over the thermodynamic ensemble, which we cannot compute, is replaced with an integral over time. *Ab initio* MD implies solving the static electronic structure problem and simultaneously propagating the nuclei classically, according to the equations of motion

$$\begin{cases} \dot{\mathbf{p}}_i(t) = \mathbf{f}_i = -\nabla_i V(\mathbf{r}) \\ \dot{\mathbf{r}}_i(t) = \frac{\mathbf{p}_i(t)}{m_i} \end{cases} . \tag{3.2}$$

The potential energy $V(\mathbf{r})$ depends, either parametrically or from the explicit *ab initio* solution of the electronic problem, on atomic positions $\{\mathbf{r}_i\}_{i=1}^N$. The right-hand side of Equation 3.2 gives the forces $\mathbf{f}_i$ acting on each atom $i \in \{1, 2, ...N\}$, from static electronic structure problem on clamped nuclei. Thus, only electrons coupled with classical nuclei are subjected to quantum mechanical treatment.

### 3.1.1 Thermostats

The simplest *microcanonical* approach to AIMD keeps the total internal energy (E), the number of particle (N) and the volume (V) constant and does not try to control the other thermodynmic observables, for this reason it is often referred as NVE. It is easy to implement and bias-free, but has the main drawback that the instantaneous temperature can fluctuate wildly, and the average one can only be enforce approximately from initial conditions. For this reason, a canonical (NVT, because T is controlled) approach can be preferable [62, 66, 67, 68, 69, 70]. In velocity rescaling method, the desired temperature is enforced by multiplying the atomic velocities with a factor $\alpha$, defined as the ratio of target $T'$ to the instantaneous temperature $T$, $\alpha = \sqrt{T'/T} = \sqrt{K'/K}$, where K is the kinetic energy. The most widely used velocity re-scaling thermostat is Berendsen thermostat [66]. Although simple, very fast, and easy to implement, it leads to wrong distribution of temperature and hence do not sample the desired canonical ensemble.

Anderson thermostat [67] on the other hand, replace the atomic velocity of an atom by that of a particle randomly drawn from a Maxwell-Boltzmann distribution at a desired temperature, for every $n^{th}$ time-step. Although stochastic in nature, the Anderson thermostat is too sensitive to n, and gives no conserved quantity.

In the case of Nose-Hoover thermostat [68] [69], an extended Hamiltonian is employed where a *fictitious oscillator*, which damps the momenta of atoms, is added to the original system. While this thermostat gives conserved quantities, the system may remain a region of the phase space, leading to ergodicity problems. Adding additional fictitious oscillators gives more ergodic canonical sampling with Nose-Hoover chains thermostats.

An advance concept that combines fast velocity rescaling and stochastic thermostats was developed, called stochastic-velocity rescaling (SVR) also known as Bussi-Donadio-Parrinello thermostats [70], named after the authors. The temperature follows a stochastic differential equation that conserve the pseudo-Hamiltonian of the system:

$$\frac{dK}{K'} = \underbrace{\left[1 - \frac{K(t)}{K'}\right]\frac{\Delta t}{\tau}}_{Rescaling} - \underbrace{2\sqrt{\frac{K(t)}{K'N\tau}}dW(t)}_{Stochastic}. \tag{3.3}$$

The characteristic time of the thermostat, $\tau = n_{raise} \times \Delta t$, is a multiple of the time-step, and is the same as in Berendsen method. $dW(t)$ is Wiener noise termed "white noise" that represents the stochastic force term, similar to the one seen in Langevin or Brownian dynamics. In the absence of the stochastic term, i.e. $W(t) = 0$, Equ. 3.3 reduces to the standard Berendsen thermostat, and in the limit $\tau \to 0$, the stochastic velocity re-scaling is enforced, yielding quick thermalization. We adopted SVR thermostat in our calculation and compare its performance (average temperature, equilibration time, and autocorrelation of the total energy)

## 3.2 Langevin Dynamics

Langevin dynamics (LD) is a stochastic method of describing the Brownian motion of particles in a solvent. Since heavy particles move much more slowly than the smaller solvent

particles, the degrees of freedom of the solvent can then be replaced by a frictional force that opposes the velocity of the heavy particles, and an additional stochastic term due to frequent collisions with (smaller) particles of the solvent, to ensure Brownian motion is ensued even in the absence of external force [62] [71]. In our case, we are want to use Langevin dynamics to model motion of atoms in an extended solid system at fixed temperature, within the DFT framework, i.e. as a thermostat in AIMD. The Langevin equation is expressed as follows:

$$\begin{cases} \dot{\mathbf{p}}_i(t) = -\underbrace{\boldsymbol{\gamma}\mathbf{p}_i(t)}_{\text{damping}} + \underbrace{\mathbf{f}_i(\mathbf{r}(t))}_{\text{Hellmann-Feymann}} + \underbrace{\sqrt{2m_i k_B T}\boldsymbol{\eta}_i(t)}_{\text{stochastic}} \\ \dot{\mathbf{r}}_i(t) = \frac{\mathbf{p}_i(t)}{m_i} \end{cases} . \tag{3.4}$$

In Equ. 3.4, $\boldsymbol{\gamma}$, $\mathbf{f}(\mathbf{q}(t))$ and $\boldsymbol{\eta}(t)$, are respectively, the Langevin friction, the deterministic force, and the stochastic force represented by the white-noise. Following the fluctuation-dissipation theorem (FDT) [63], the dissipative Langevin damping $\boldsymbol{\gamma}$ is compensated by fluctuations induced by the stochastic forces $\boldsymbol{\eta}(t)$ via temperature dependence, such that

$$\langle \boldsymbol{\eta}(t)\boldsymbol{\eta}(t')\rangle = \delta(t-t')\boldsymbol{\alpha}(\tau) \quad \text{with } \boldsymbol{\alpha} = 2k_B T\boldsymbol{\gamma}. \tag{3.5}$$

The equations of motion in Equation 3.4 can be expressed in terms of the probability density $P(\Gamma, t)$ that evolves according to the Fokker-Planck equation [72] which reads as

$$\frac{\partial P(\Gamma, t)}{\partial t} = iL_{FP}P(\Gamma, t), \tag{3.6}$$

where $iL_{FP} = iL_p + iL_q + iL_\gamma$ is the Fokker-Planck Liouvillian, evolving the momenta, the coordinates and defining the thermostat, respectively.

### 3.2.1 Bussi-Parinello algorithm

Langevin equation can be integrated in a number ways [62]. In our case, we adopted the recent implementation of the Bussi-Parrinello [39] algorithm by Moressi et al, [6]. The Fokker-Planck plank equation derived from Eq. 3.4, allows Trotter-splitting of a propagator into multiple subspaces

$$\begin{aligned} e^{-\Delta t L} &\approx e^{-(\Delta t/2)L_\gamma} e^{-\Delta t L_{\mathbf{pr}}} e^{-(\Delta t/2)L_\gamma} \\ &\approx e^{-(\Delta t/2)L_\gamma} e^{-(\Delta t/2)L_{\mathbf{p}}} e^{-\Delta t L_{\mathbf{r}}} e^{-(\Delta t/2)L_{\mathbf{p}}} e^{-(\Delta t/2)L_\gamma} \end{aligned} \tag{3.7}$$

where $e^{-(\Delta t/2)L_\gamma}$ is a step in momenta subspace that provides ergodicity and is propagated analytically, while $e^{-\Delta t L_{\mathbf{pr}}}$ is a step in the mixed momenta-coordinates subspace propagated similar to velocity-Verlet algorithm. The Bussi-Parrinello algorithm consists of the followinng steps:

$$\mathbf{p}(t^+) = c_1\mathbf{p}(t) + c_2 R(t) \tag{3.8a}$$

$$\mathbf{r}(t+\Delta t) = \mathbf{r}(t) + \frac{\mathbf{p}(t^+)}{m}\Delta t + \frac{\mathbf{f}(r(t))}{m}\frac{\Delta t^2}{2} \tag{3.8b}$$

$$\mathbf{f}(t+\Delta t) = -\nabla V(t+\Delta t) \tag{3.8c}$$

$$\mathbf{p}(t^- + \Delta t) = \mathbf{p}(t^+) + \frac{\mathbf{f}(r(t)) + \mathbf{f}(r(t+\Delta t))}{2}\Delta t \tag{3.8d}$$

$$\mathbf{p}(t^+ + \Delta t) = c_1\mathbf{p}(t^- + \Delta t) + c_2 R'(t+\Delta t) \tag{3.8e}$$

Here, Eqs. 3.8a and 3.8e are thermostating steps where damping and random forces appear, while Eqs .3.8b and 3.8d are velocity-Varlet steps. $R$, $R'$ are Gaussian numbers and $c_1$, $c_2$ are coefficients related to the damping $\gamma$ and inverse temperature $\beta$ according to $c_1 = e^{-\gamma(\Delta t/2)}$ and $c_2 = \sqrt{(1-c_1^2)\frac{m}{\beta}}$.

LD has been used to describe the thermodynamical behavior of more diverse systems [39] [73] [6]. In the absence of damping ($\gamma = 0$), LD reduces to NVE, and in the absence of deterministic Born-Oppenheimer forces it reduces to Brownian motion. In the intermediate range its behavior depends on the ratio of $\gamma$ and the time step ($\Delta t$), with a large range of acceptable good values which can be determined by testing and computing the correlation time of $V$, on a case by case basis. In Chapter X, this method is employed to sample uncorrelated AIMD snapshots. The small correlation time and fast equilibration of this approach over MD considerably decrease computing time and allow efficient canonical sampling of the Born-Oppenheimer PES.

## 3.3 Lattice Dynamics

We presented the Born-Oppenheimer approximation in Section 2.2, which separates the electronic and nuclear degrees of freedom for a many-body Schrodinger equation, yielding the equation for electrons at fixed nuclear coordinates. However, because of translational invariance in a crystal, the collective motions of nuclei are the natural framework to describe the vibration associated This type of motion constitutes Lattice dynamics, a theory developed in the 1930s, but especially by Born and Huang in their 1954 book [15], which provides fundamental formulations and properties of dynamical matrices. Lattice dynamics is responsible for many properties of materials, including thermal expansion, resistivity, superconductivity, optical properties, Infrared, Raman, Neutron diffraction spectra, and so on [16]. The connection between lattice dynamics and electronic structure was made in 1969 by De Cicco *et al*. [74] and in 1970 by Pick *et al* [75]. Since then, remarkable progress has been made. Due to advances in algorithms and progress in computing power, nowadays, it is possible to compute the vibrational properties of materials with remarkable accuracy. In this Sections we introduce Harmonic approximation, its quasi-harmonic extension, and phonon anharmonicity from the perturbation theory and beyond. The expressions presented here will be used throughout the thesis.

### 3.3.1 Harmonic approximation

The simplest model that describes lattice dynamical properties in solids is the *harmonic approximation*. The hamiltonian function that describes the motion of the nuclei depends on the shape of the BO potential energy, which can be very complex. However, as long as the range of vibration of the nuclei remains small w.r.t their interatomic distance, we can try to expand the BO energy $U$ as a Taylor series around the equilibrium in terms of the nuclei displacements $\mathbf{u}$ from their equilibrium positions, as:

$$U = U_0 + \sum_{i,\alpha} \frac{\partial U}{\partial u_i^\alpha} u_i^\alpha + \frac{1}{2!} \sum_{ij,\alpha\beta} \frac{\partial^2 U}{\partial u_i^\alpha \partial u_j^\beta} u_i^\alpha u_j^\beta + \frac{1}{3!} \sum_{ijk,\alpha\beta\gamma} \frac{\partial^3 U}{\partial u_i^\alpha \partial u_j^\beta u_k^\gamma} u_i^\alpha u_j^\beta u_k^\gamma + ..., \qquad (3.9)$$

where the composite index $a = (i, \alpha)$ indicate both atomic $(ijk)$ and Cartesian $(\alpha, \beta, \gamma)$ indices. $U_0$ is constant and the first-derivative give vanishing forces at equilibrium. The

second (third) derivative of the potential energy with respect to the displacements give the second-order (third-order) interatomic force constants (IFCs):

$$\Phi_{ij}^{\alpha\beta} = \frac{\partial^2 U}{\partial u_i^\alpha \partial u_j^\beta}, \quad \Phi_{ijk}^{\alpha\beta\gamma} = \frac{\partial^2 U}{\partial u_i^\alpha \partial u_j^\beta \partial u_k^\gamma}, \ldots \tag{3.10}$$

The harmonic approximation consists in neglecting the third and higher-order terms so that the BO potential in Eq. 3.9 around the equilibrium is reduced to its second order:

$$U \approx \frac{1}{2} \sum_{ij,\alpha\beta} \Phi_{ij}^{\alpha\beta} u_i^\alpha u_j^\beta. \tag{3.11}$$

The classical equation of motion for the atoms in the harmonic potential is given as:

$$M_i \ddot{u_i^\alpha} = -\frac{\partial U}{\partial u_i^\alpha} = -\sum_{j\beta} \Phi_{ij}^{\alpha\beta} u_j^\beta \ . \tag{3.12}$$

In crystalline solid materials, one can define the position of an atom $i$, in a unit cell $l$, occupying the lattice site $n$, as $\mathbf{R}_i = \mathbf{r}_l + \mathbf{r}_n + \mathbf{u}_{ln} = \mathbf{r}_{ln} + \mathbf{u}_{ln}$. Assuming that all atomic displacements are coherently connected by a plane wave with wave vector, $\mathbf{q}$ and angular frequency, $\omega$, then the displacement is given as

$$\mathbf{u}_{ln} = \frac{1}{N} \sum_{\mathbf{q}s} A_{\mathbf{q}s} e^{i(\mathbf{q}\cdot\mathbf{r}_{ln} - \omega_{\mathbf{q}s} t)} \tag{3.13}$$

$A_{\mathbf{q}s}$ is the normal-mode coordinate and $\varepsilon_{\mathbf{q}s}$ is the polarization vector. Therefore, the equations of motion for atoms in Eq. 3.12 are then transformed into a set of decoupled algebraic equations,

$$\sum_{j\beta} D_{ij}^{\alpha\beta}(\mathbf{q}) = \omega_{\mathbf{q}s}^2 u_{ln}^\alpha \tag{3.14}$$

where

$$D_{ij}^{\alpha\beta}(\mathbf{q}) = \frac{1}{\sqrt{M_i M_j}} \sum_{\mathbf{R}} \Phi_{ij}^{\alpha\beta} e^{-i\mathbf{q}\cdot\mathbf{R}} \tag{3.15}$$

We can invoke second quantization and express the atomic displacements and momenta in terms of phonon creation $\hat{a}_{\mathbf{q}s}^\dagger$ and annihilation $\hat{a}_{\mathbf{q}s}$ operators (see Appendix A), in terms of which the harmonic Hamiltonian becomes

$$\begin{aligned} \hat{H} &= \sum_{\mathbf{q}s} \hat{h}_{\mathbf{q}s} = \sum_{\mathbf{q}s} \hbar\omega_{\mathbf{q}s} (\hat{a}_{\mathbf{q}s}^\dagger \hat{a}_{\mathbf{q}s} + \frac{1}{2}) \\ &= \sum_{\mathbf{q}s} \hbar\omega_{\mathbf{q}s} (n_{\mathbf{q}s} + \frac{1}{2}) \end{aligned} \tag{3.16}$$

The energy of a quantum harmonic oscillator is given by $E = \hbar\omega_{\mathbf{q}s}(n_{\mathbf{q}s} + \frac{1}{2})$ where $\hbar\omega_{\mathbf{q}s}/2$ is the zero-point energy of the atoms as they move around their equilibrium points, in the absence of thermal excitation. Thermodynamic properties can be determined from the partition function of N atoms, $Z_N = \prod_i^N Z_i$, where for each oscillator,

$$Z = \frac{e^{-\beta\hbar\omega_{\mathbf{q}s}}}{1 - e^{-\beta\hbar\omega_{\mathbf{q}s}}}$$

### 3.3.2 Quasi-Harmonic approximation

In the harmonic approximation (HA), the vibrational contribution to the internal energy of a crystal does not depend on volume because the vibrational frequencies are independent of interatomic distances. The HA also has a number of limitations, including the fact that it predicts no thermal expansion, an infinite thermal conductivity, due to absence of phonon-phonon interactions, and that vibrational spectra, and related properties, are independent of temperature. Furthermore, the heat capacities at constant pressure ($C_P$) and volume ($C_V$) would be identical, and neither the force-constants nor the elastic constants would change with temperature or pressure. The description of the anharmonic effect and its role in static and dynamic properties of materials would require computing phonon-phonon interaction coefficients for all modes in the BZ, which is a daunting task. Quasiharmonic approximation (QHA) is the simplest method of computing free energy without the need for explicit computation of anharmonic interaction coefficients [76], [19], [20]. Helmholtz free energy ($F(X,T)$) is the fundamental quantity from which all thermal properties are derived. Within the adiabatic approximation, $F(X,T)$ can be expressed as:

$$F(X,T) = E_0(X) + F_{vib} = E_0(X) + E_{vib}(X,T) - TS \tag{3.17}$$

where $E_0$ is the static total energy from first principles DFT in our case, $S_{vib}$ is the vibrational entropy from the lattice vibration (non-vibrational entropy such as electronic, magnetic, and configurational, depend on the system and require careful treatment) and $X$ is a global constraints that the vibrational frequencies can depend on, e.g., volume, internal distortion, external field, etc. In the case $X = V$, then $F(V,T)$ is given as:

$$F(V,T) = E_0(V) + k_B T \sum_{\mathbf{q},s} \ln\left[2\sinh\left(\frac{\hbar\omega_{\mathbf{q},s}(V)}{2k_B T}\right)\right]. \tag{3.18}$$

$\omega_{\mathbf{q},s}(V)$ is the phonon frequency from harmonic approximation at a given volume $V$, and $\mathbf{q}, s$ represent the phonon wave vector and branch, respectively. $k_B$ and $\hbar$ are Boltzmann's and Planck's constants, respectively. Computing $F(V,T)$ at different volumes and then fitting the calculated value to the equation of state (EOS) gives finite temperature properties. Standard thermodynamic relations [76] are then employed to get the entropy $S_{vib}$ and pressure $P$:

$$P = -\frac{\partial F(V,T)}{\partial V}, \quad S = -\frac{\partial F(V,T)}{\partial T} \tag{3.19}$$

These thermodynamic quantities ($E, T, V, S$ and $P$) are then used to obtain *Gibbs Free energy*:

$$G = E - TS + PV = F + PV \tag{3.20}$$

At finite temperature, these quantities have contribution due to both zero-point and thermal excitation. For instance, the QHA pressure is given as

$$\begin{aligned} P &= -\frac{\partial F(V,T)}{\partial V} \\ &= \frac{\partial E_0(V)}{\partial V} + \frac{1}{V}\sum_{\mathbf{q},s} \hbar\omega_{\mathbf{q},s}\gamma_{\mathbf{q},s}\left[\frac{1}{2} + \frac{1}{e^{\frac{\hbar\omega_{\mathbf{q},s}}{k_B T}} - 1}\right] \end{aligned} \tag{3.21}$$

where

$$\gamma_{\mathbf{q},s} = -\frac{V}{\omega_{\mathbf{q},s}}\frac{\partial \omega_{\mathbf{q},s}}{\partial V}$$

are called the *Grüneisen parameters* of the mode $(\mathbf{q}, s)$. The thermal expansion coefficient $\beta_T$ is given as:

$$\begin{aligned}\beta_T &= \frac{1}{V}\frac{\partial V}{\partial T} = \frac{1}{V}\frac{(\partial P/\partial T)}{(\partial P/\partial V)} \\ &= \frac{1}{B}\frac{\partial P}{\partial T} \\ &= \frac{1}{B}\sum_{\mathbf{q},s}\hbar\omega_{\mathbf{q},s}\gamma_{\mathbf{q},s}n'_{\mathbf{q},s},\end{aligned} \tag{3.22}$$

where $B$ is the bulk modulus of the crystal and $n'_{\mathbf{q},s}$ is the derivative of the Bose-Einstein occupation number.

QHA, in the framework of DFT, with harmonic phonons computed either from finite difference in supercell or linear response (DFPT), results in a powerful simulation method that has been shown to be successful over a wide range of temperatures and different classes of materials [19, 20] The early applications of QHA with ab initio phonons addressed the negative thermal expansion of tetrahedrally coordinated elemental and binary semiconductors [77], [78], [79]. Subsequently, QHA has been applied to study metals, surfaces, and minerals. It is possible to predict many materials' pressure-temperature phase diagrams (P-T phase diagrams), and compare to experiments [20].

The QHA method can be reliably accurate, particularly in cases where DFPT can be used to calculate phonon frequencies on a finer grid. However, its validity can be questioned if the anharmonic effect is strong. QHA requires dynamic stability and, therefore, cannot describe phase transition in cases involving imaginary frequencies. Furthermore, the QHA has to be used for temperatures lower than the melting point. Self-consistent quasiharmonic approximation (SC-QHA)[80, 81] is a new improvement on QHA that reduces the number of volumes needed to only three.

### 3.3.3 Anharmonicity from perturbation theory

The phonon quasiparticle picture allows one to add higher-order terms in the expansion of the BO energy given by Eq. 3.9. Thus, the Hamiltonian in operator formalism up to fourth order can be expressed as:

$$\hat{H} = \hat{H}_2 + \hat{H}_3 + \hat{H}_4 \tag{3.23}$$

where the constant energy is neglected and

$$\begin{aligned}\hat{H}_2 &= \sum_{\lambda}\hbar\omega_{\lambda}(\hat{a}^{\dagger}_{\lambda}\hat{a}_{\lambda} + \frac{1}{2}), \\ \hat{H}_3 &= C_3\sum_{\lambda\lambda'\lambda''}\Phi_{\lambda\lambda'\lambda''}(\hat{a}_{\lambda} + \hat{a}^{\dagger}_{-\lambda})(\hat{a}_{\lambda'} + \hat{a}^{\dagger}_{-\lambda'})(\hat{a}_{\lambda''} + \hat{a}^{\dagger}_{-\lambda''}), \\ \hat{H}_4 &= C_3\sum_{\lambda\lambda'\lambda''\lambda'''}\Phi_{\lambda\lambda'\lambda''\lambda'''}(\hat{a}_{\lambda} + \hat{a}^{\dagger}_{-\lambda})(\hat{a}_{\lambda'} + \hat{a}^{\dagger}_{-\lambda'})(\hat{a}_{\lambda''} + \hat{a}^{\dagger}_{-\lambda''})(\hat{a}_{\lambda'''} + \hat{a}^{\dagger}_{-\lambda'''}),\end{aligned} \tag{3.24}$$

where we used condensed index $\lambda = (\mathbf{q}s)$. $\hat{H}_3$ is the lowest order anharmonic perturbation, and correspond to the three-phonon interaction (two phonons coalescing into a third or one phonon splitting into two). Similarly, $\hat{H}_4$ represent a four-phonon processes. $\Phi_{\lambda\lambda'\lambda''}$ and $\Phi_{\lambda\lambda'\lambda''\lambda'''}$ are the three and four phonon matrix elements obtainable from real-space three- and four-body force constants, respectively.

$$\Phi_{\lambda\lambda'\lambda''} = \sum_{ijk}\sum_{\alpha\beta\gamma} \frac{\varepsilon_{\lambda}^{\alpha,i}\varepsilon_{\lambda'}^{\beta,j}\varepsilon_{\lambda''}^{\gamma,k}}{\sqrt{M_i M_j M_k}\sqrt{\omega_\lambda\omega_{\lambda'}\omega_{\lambda''}}}\Phi_{ijk}^{\alpha\beta\gamma} e^{i(\mathbf{q}\cdot\mathbf{r}_i+\mathbf{q}'\cdot\mathbf{r}_j+\mathbf{q}''\cdot\mathbf{r}_k)} \tag{3.25}$$

$$\Phi_{\lambda\lambda'\lambda''\lambda'''} = \sum_{ijkl}\sum_{\alpha\beta\gamma\delta} \frac{\varepsilon_{\lambda}^{\alpha,i}\varepsilon_{\lambda'}^{\beta,j}\varepsilon_{\lambda''}^{\gamma,k}\varepsilon_{\lambda'''}^{\delta,l}}{\sqrt{M_i M_j M_k M_l}\sqrt{\omega_\lambda\omega_{\lambda'}\omega_{\lambda''}\omega_{\lambda'''}}}\Phi_{ijkl}^{\alpha\beta\gamma\delta} e^{i(\mathbf{q}\cdot\mathbf{r}_i+\mathbf{q}'\cdot\mathbf{r}_j+\mathbf{q}''\cdot\mathbf{r}_k+\mathbf{q}'''\cdot\mathbf{r}_l)} \tag{3.26}$$

In many-body perturbation theory, the complex frequency-dependent phonon self-energy [82] is expressed as the sum of the real and imaginary part

$$\begin{aligned} \Sigma_\lambda &= \Delta_{\mathbf{q}s} + i\Gamma_{\mathbf{q}s} \\ \Delta_{\mathbf{q}s} &= \Delta^3_{\mathbf{q}s} + \Delta^4_{\mathbf{q}s} \end{aligned} \tag{3.27}$$

where $\Delta_{\mathbf{q}s}$ is the anharmonic shift in the phonon frequencies, with contribution from three- and four-phonon processes, while $\Gamma_{\mathbf{q}s}$ is the imaginary part of the self-energy that correspond to broadening, inversely related to the phonon lifetime, $\Gamma_{\mathbf{q}s} = \frac{1}{\tau_{\mathbf{q}s}}$, and computed using Fermi's golden rule [83, 84]

$$\Gamma_{\mathbf{q}s} = \frac{\pi}{\hbar^2 N_{\mathbf{q}}}\sum_{\lambda'\lambda''} F(\omega_\lambda, \omega_{\lambda'}, \omega_{\lambda''})|\Phi_{\lambda\lambda'\lambda''}|^2 \tag{3.28}$$

where

$$F(\omega_\lambda, \omega_{\lambda'}, \omega_{\lambda''}) = (1 + n_{\lambda'} + n_{\lambda''})\delta(\omega_\lambda - \omega_{\lambda'} - \omega_{\lambda''}) + 2(n_{\lambda'} - n_{\lambda''})\delta(\omega_\lambda + \omega_{\lambda'} - \omega_{\lambda''})$$

$N_{\mathbf{q}}$ is the total number of $\mathbf{q}$-points sampled in the 1BZ of the phonon $(\mathbf{q}s)$, $\delta(y)$ is the Dirac delta function, and $n_\lambda$ is the phonon Bose-Einstein occupation number. However, $n_\lambda$ can differ from the equilibrium phonon distribution in an iterative solution but serve as an initial guess. In cases where comparison needs to be made with classical MD, $n_\lambda$ is set to follow the classical distribution $n_\lambda = k_B T/\hbar\omega$.

Anharmonic lattice dynamics using the three-phonon scattering developed in the 1960s by Maradudin et al. [83] finds application in the first principles method following the development of DFPT and the "2n+1" theorem [85]. It states that the derivative of the wavefunction and charge density to order n gives the derivative of the total energy to order "2n+1". This development paved the way for the prediction of three-phonon scattering coefficients and linewidth for Insulators and semiconductors for the zone-center (Γ-point) phonons and later for metals [86], which can be compared directly to Raman and Infrared measurements. Subsequent development allows the computation of three-phonon scattering coefficients at arbitrary $\mathbf{q}$-points, applicable to metals and insulators of any geometry [84], as well as other techniques based on finite difference in supercells [87, 88].

Once anharmonic scattering coefficients and the harmonic phonon spectra are obtained from FCs, the thermal conductivity can be readily computed. In 1929, Peierls [89] developed

the first microscopic description of the thermal conductivity in insulators by "heat carrying particles", known as the Boltzmann transport equation (BTE), which was later solved by Omini and Sparavigna iteratively [90]. In the single mode approximation (SMA) [91], which is the most widely used method, the thermal conductivity tensor along Cartesian direction $\alpha$, in the presence of thermal gradient along $\beta$ direction, is given by

$$\kappa_{\alpha\beta} = \frac{\hbar^2}{N_0 \Omega k_B T^2} \sum_j v_{\alpha,\lambda} v_{\beta,\lambda} \omega_\lambda^2 n_\lambda (n_\lambda + 1) \tau_\lambda, \tag{3.29}$$

where $N_0$ is the total number of $\mathbf{q}$-points that sample the Brillouin zone, $\lambda$ is the index for both phonon wave vector $\mathbf{q}$ and the branch $s$, $\Omega$ is volume of the unit cell, $v_{\alpha,\lambda} = \nabla_{\mathbf{q}} \omega_{\mathbf{q}s}$ is the phonon group velocity, $n_\lambda$ is the Bose-Einstein distribution function, and $\tau_\lambda$ is the phonon lifetime obtainable from Eq. 3.28.

In real materials, however, phonon transport is impeded not only by three-phonon interaction in bulk but also by multiple scattering mechanisms. These include higher-order scattering (four-phonon), phonon-isotope scattering, phonon-boundary scattering, phonon-impurity, electron-phonon scattering, etc. Matthiessen's general rule [92] gives the total scattering rates as a sum, assuming all scattering events are independent, as

$$\frac{1}{\tau} = \frac{1}{\tau_{3ph}} + \frac{1}{\tau_{4ph}} + \frac{1}{\tau_{e-ph}} + \frac{1}{\tau_{ph-iso}} + \frac{1}{\tau_{ph-boundary}} + ... \tag{3.30}$$

In recent years, it has been shown that four-phonon scattering plays an important role in forecasting the lattice thermal conductivity of materials. For instance, including it can result in a decrease of up to 60% percent in the $\kappa_l$ of BAs [93].

Anharmonic Lattice dynamics using the BTE approach (ALD-BTE) is a powerful method of choice that is gaining increasing popularity due to the development of new theoretical techniques and implementation in freely accessible codes. These enable parameter-free *ab initio* characterization of materials ranging from 3D, to 2D and 1D nanostructures as well as intercalated and other complex materials [94, 95]. Popular examples include codes such as D3Q+thermal2 [84], Phono3py [88], ShengBTE [87], ALAMODE [96], etc.

### 3.3.4 Anharmonicity beyond perturbation theory

So far, we have introduced phonons as independent harmonic oscillators (harmonic approximation), with temperature dependence only via volume (quasiharmonic approximation), and weakly interact with each other, where the temperature only changes their population via the occupation number $n_\lambda$ (perturbation theory). These formulations described the standard phonon quasiparticle picture of solid materials.

However, these formulations cannot describe materials stabilized by temperature or in the vicinity of phase transition. The harmonic approximation breaks down, and the small displacement assumption in the perturbation theory, which allows Taylor expansion, becomes invalid. We refer to these materials as strongly anharmonic. As early as the 1950s, Born and Hooton [21, 22], and later others [23, 24], recognized this issue, and their subsequent work led to the development of a theory, the self-consistent phonon theory, which has since been successfully adopted for the description of strongly anharmonic materials [41]. In the last two decades, there has been increasing interest in non-perturbative anharmonic methods

[27, 29, 32, 33, 35, 38, 6, 96], each with its unique formulation in how anharmonic effects are reintroduced, and we shall discuss some of them that are based on density functional theory. Consequently, we will move the discussion of the temperature-dependent effective potential approach (TDEP) to Chapter 4 prior to our TDPH method.

#### 3.3.4.1 Velocity autocorrelation function (VACF) method

Ab initio molecular dynamics (AIMD) simulations sample the potential energy surface, including full anharmonicity. Normal-mode analysis (NMA) [25, 26] approaches have been used to calculate dynamic and transport properties as time averages over trajectories. NMA benefits from not having to compute higher-order force constants directly, helpful in treating large systems, and their use of AIMD to derive renormalized phonon frequencies and lifetimes, allowing renormalized frequencies and phonon lifetime to be obtained from non-perturbatively. The fundamental drawback of these approaches is the extended time needed in simulation to achieve ergodicity and/or the desired frequency resolution and the absence of nuclear quantum effects. However, since harmonic phonons from finite difference or linear response methods in DFT have zero-point energy, a quantum effect, but lack explicit temperature dependence, which can be accounted for in AIMD, the combination of the two methods complements each other.

The first contribution in this direction was by de Koker [27], using the power spectrum of the velocity autocorrelation to obtain phonon frequencies and linewidths and a fit to exponentially decaying function to extract lifetime from the power spectrum. The predicted lattice conductivity for MgO periclase agrees with the experiment. However, there are several phonon modes in materials with large unit cells having comparable frequencies. The difficulty arises when the spectra of these modes overlap.

Renata and coworkers [28] proposed that solving this problem requires determining the power spectra of all 3N possible modes, each with its unique wave vector $\mathbf{q}$ and polarization branch $s$. Also, harmonic phonon spectra computed in a unit cell are projected to the atomic velocities from AIMD in a supercell. Within this formalism, the VACF is given by

$$\langle \mathbf{V_q}(0) \cdot \mathbf{V_q}(t) \rangle = \lim_{\tau \to \infty} \frac{1}{\tau} \int_0^{\tau} V_{\mathbf{q}}(t') V_{\mathbf{q}}(t'+t) dt \tag{3.31}$$

where the $\mathbf{q}$-mode mass-weighed projected velocity $V_{\mathbf{q}}(t)$ is given by

$$V_{\mathbf{q}}(t) = \sum_i^N \sqrt{m_i} \mathbf{v}_i(t) e^{i\mathbf{qR}} \cdot \hat{e}_{\mathbf{q}}$$

$m_i$, $\mathbf{v}_i$ and $\mathbf{r}_i$ (i=1,2,..N) are mass, velocity and equilibrium coordinate atoms in an N-atom supercell computed from AIMD. The symbol, $\mathbf{q}$ represent both normal mode and the $s = 3n$ phonon branches i.e. $\mathbf{q} = (\mathbf{q}, s)$.

The VACF is also phenomelogically described by an exponentially decaying cosine function

$$\langle \mathbf{V_q}(0) \mathbf{V_q}(t) \rangle = A_{\mathbf{q}} cos(\tilde{\omega}_{\mathbf{q}} t) e^{-\Gamma_{\mathbf{q}} t} \tag{3.32}$$

$\tilde{\omega}_{\mathbf{q}}$ and $A_{\mathbf{q}}$ represent renormalized phonon frequencies and oscillation amplitude, respectively. In this case, finite temperature phonon shift is $\Delta_{\mathbf{q}} = \tilde{\omega}_{\mathbf{q}} - \omega_{\mathbf{q}}$.

The phonon lifetime, $\tau_{\mathbf{q}}$ is inversely proportional to the linewidth $\Gamma_{\mathbf{q}}$

$$\tau_{\mathbf{q}} = \frac{1}{2\Gamma_{\mathbf{q}}} \tag{3.33}$$

In VACF method, anharmonic properties can computed non-perturbatively, similar to the many-body formalism where strong anharmonic phonon-phonon interaction causes phonon-quasiparticles to acquire self-energy (frequency shift and linewidth): $\Sigma_{\mathbf{q}s} = \Delta_{\mathbf{q}s}\omega_{\mathbf{q}s} + i\Gamma_{\mathbf{q}s}$. The VACF has been implemented (`phq code`) and successfully applied to study lattice thermal conductivity in MgO periclase [27], phonon shift in Si and $MgSiO_3$ [28], anharmonic thermodynamics in $CaSiO_3$ [97], giant anharmonicity in thermoelectric PbTe [98], phase-transition in SnSe [99], among others.

#### 3.3.4.2 Force-force correlators method

Here we shall describe the classical correlators, to limit our discussion within the framework of DFT since quantum correlators require path-integral molecular dynamics simulation (PIMD). For the classical correlators consider an N-partcle Hamiltonian given by positions ($\mathbf{x}$) and momenta ($\mathbf{p}$) vectors that defines the kinetic $K$ and potential $V$ energy of the particles as

$$H(\mathbf{x},\mathbf{p}) = \sum_{i=1}^{3N}\Big[\frac{\mathbf{p}_i^2}{2m_i} + m_i\omega_i^2(\mathbf{x}_i - \mathbf{x}_j)^2\Big] = K + V \tag{3.34}$$

Eq. 3.34 is the classical limit of the path-integral Hamiltonian for 3NP-distinguishable particles with P=1 [6]. At a given temperature one can define a the force-constant matrix or the effective Hessian [100] [101], as

$$\Pi_{ij} = \Big\langle \frac{\partial^2 V}{\partial \mathbf{x}_i, \partial \mathbf{x}_j} \Big\rangle \tag{3.35}$$

where the brackets represent averages computed in canonical ensemble. $i,j = 1,2,...3N$ Cartesian coordinates. The matrix $\Pi_{ij}$, can go into the standard eigenvalue problem

$$\Pi_{ij}\tilde{e}_{j,k} = \omega_k^2\tilde{e}_{i,k}, \tag{3.36}$$

where the $\omega_k$ is the $k^{th}$ frequency of the mode with eigenvector $\tilde{e}_{i,k}$. At statistical equilibrium, their is an exact relationship between force fluctuation and the potential that can be leveraged to obtain atomic forces [101], [100]:

$$\begin{aligned}\langle F_i F_j\rangle &= \int d^N\mathbf{p}\; e^{-\beta K}\int d^N\mathbf{x}\;\frac{\partial V}{\partial \mathbf{x}_i}\frac{\partial V}{\partial \mathbf{x}_j}\frac{e^{-\beta V}}{Z} \\ &= \frac{1}{\beta}\Pi_{ij}\end{aligned} \tag{3.37}$$

where $F_i$ represent the $i^{th}$ component of the force acting on atom 1, $\beta = 1/kT^{-1}$, and $Z$ is the configuration partition function. Eq. 3.37 can also be obtained from the velocity autocorrelation [101], and can be generalized to third-order term [100]. Importantly, the equation is exact and independent of the form of the potential. An additional or alternative

way of computing the force-constant matrix in Eq. 3.35 is the displacement-displacement correlators:

$$\begin{aligned}\langle \delta x_i \delta x_j \rangle &\approx \int d^N\mathbf{p}\, e^{-\beta K} \int d^N\mathbf{x}\, \delta x_i \delta x_j \frac{e^{-\frac{\beta}{2}\delta\mathbf{x}^T\cdot\Pi\cdot\delta\mathbf{x}}}{Z} \\ &\approx \beta[\Pi^{-1}]_{ij}\end{aligned} \tag{3.38}$$

where $\delta\mathbf{x} = \mathbf{x} - \overline{\mathbf{x}}$ is the displacement from the equilibrium positions extracted from the trajectory.

The force-force <ff> and displacement-displacement <xx> correlators have been tested extensively on toy models, with simple potentials, and also on a number of real system including diamond and high-pressure atomic hydrogen $I41/amd$ [6], accurately predicting the anharmonic Raman shift in agreement with the expensive Quantum Monte-Carlo result [102]. The correlators method have also been implemented in QUANTUM ESPRESSO, using PIOUD algorithm for both classical and quantum (PIMD) correlators [6]. We compared this method to our own in subsequent Chapters.

#### 3.3.4.3 Self-consistent phonon methods

Self-consistent phonon approximation is the most popular theory of obtaining renormalized phonons, and it has many variants. In its original formulation, the true Gibbs-free energy $F$ satisfies Gibbs-Bogoliubov principle

$$F \leq F_H + \langle V(\mathbf{R}) - \mathcal{V}_H(\mathcal{R})\rangle_H \tag{3.39}$$

where $F_H$ is a trial free energy, $\mathcal{V}_H(\mathbf{R})$ is the trial harmonic potential.

The earliest contribution in the family of SCP-based methods is the self-consistent ab initio lattice-dynamical method (SCAILD) by Souvatzis et al. [29]. Atomic forces $\mathbf{F_R}$ are computed for atoms in a supercell and used to calculate initial trial phonon dispersion. The eigenmodes are then used to displace atoms with an amplitude $\mathcal{A}$, at the target temperature, T. Atomic forces are computed, Fourier transformed $\mathbf{F_q}$, and then used to generate new phonon frequencies $\omega_{\mathbf{q}s}$ with eigen mode $\varepsilon_{\mathbf{q}s}$. Atoms are then moved with displacements $U_{\mathbf{R}}$. The set of self-consistent equations are:

$$\mathcal{A}_{\mathbf{q}s} = \pm\sqrt{-\hbar(2n_{\mathbf{q}s}+1)/2M\omega\mathbf{q}s} \tag{3.40}$$

$$U_{\mathbf{R}} = \frac{1}{\sqrt{M}} \sum_{\mathbf{q}s} \mathcal{A}_{\mathbf{q}s}\varepsilon_{\mathbf{q}s} e^{i\mathbf{q}\cdot\mathbf{R}} \tag{3.41}$$

$$F_{\mathbf{R}} = -\sum_{\mathbf{R}'} \Phi(R-R')U_{\mathbf{R}'} \tag{3.42}$$

$$F_{\mathbf{q}} = -\sum_{s} M\omega^2_{\mathbf{q}s}\mathcal{A}_{\mathbf{q}s}\varepsilon_{\mathbf{q}s} \tag{3.43}$$

$$\omega_{\mathbf{q}s} = \left[ -\frac{1}{M}\frac{\varepsilon_{\mathbf{q}s}F_{\mathbf{q}}}{\mathcal{A}_{\mathbf{q}s}} \right]^{1/2} \tag{3.44}$$

SCAILD have been successfully applied predict phonon spectra of high temperature BCC phases of Zr, Ti, and Hf [29], and their free energy [103]. Roekeghem et al. extended the

method to QSCAILD [31] by using quantum covariance of atomic displacement in canonical sampling [30], similar to SSCHA, and generalizing to third-order force constants.
In the stochastic self-consistent harmonic approximation (SSCHA) [38], the free energy is minimized variationally with respect to the the trial force constants $\Phi(q)$, and centroids $\mathcal{R}$, where

$$\mathcal{V}_H(\mathcal{R}) = \frac{1}{2}\sum_{q}\sum_{ss',\alpha\beta} u_s^{\alpha^*}(\mathbf{q})\Phi_{ss'}^{\alpha\beta}u_{s'}^{\beta}(\mathbf{q}) \tag{3.45}$$

SSCHA has been employed to study anharmonicity due to both thermal and nuclear quantum effects in several materials, including superconducting hydrides, transitional metal dichalcogenides, ferroelectric and charge density wave transition (CDW), and high-pressure phases of hydrogen [38, 104]. The success of SCCHA can be attributed to its rigorous theoretical formulation, and its limitation is the large number of canonical configurations required for self-consistency.

In the SCPH method of Tadano et al. [10], the lowest even-order term (i.e. the quartic) is considered in solving the self-consistent equations:

$$\Omega_{\mathbf{q}}^2 = \omega_{\mathbf{q}}^2 + 2\Omega_{\mathbf{q}}I_{\mathbf{q}}^a \tag{3.46}$$

$$I_{\mathbf{q}}^a = \frac{1}{2}\sum_{\mathbf{q}_1}\frac{\hbar\Phi(\mathbf{q},-\mathbf{q};\mathbf{q}_1;-\mathbf{q}_1)}{4\Omega_{\mathbf{q}}\Omega_{\mathbf{q}_1}}[1+2n(\Omega_{\mathbf{q}_1})] \tag{3.47}$$

where $\Phi(\mathbf{q},-\mathbf{q};\mathbf{q}_1;-\mathbf{q}_1)$ is the fourth-order force-constants in $\mathbf{q}$-space and $n(\Omega)$ is the phonon Bose-Einstein distribution function. SCPH employed sparse representation-based compressive sensing with the least absolute shrinkage and selection operator (LASSO) or elastic-net technique to enhance computational speed in extracting higher-order force constants.

# 4 – Temperature-dependent phonon method (TDPH)

Part of this Chapter appeared in the Journal article: Garba, I. B., Morresi, T., Bouillaguet, C., Casula, M., & Paulatto, L. *Journal of Physics: Condensed Matter (2023).*

It is clear that true vibrational properties of a system cannot be obtained from the harmonic approximation since we neglect higher order terms in the expansion of Eq. 3.9 that give rise to anharmonic effects. Anharmonic effects play important role in properties of materials with weak bonding, light elements, close to phase transition or at higher temperature. Any or a combination of these effects manifest in materials leading to large vibrational amplitude that render the harmonic approximation invalid, preventing also perturbative methods. In this case, anharmonic (and non-perturbative) methods becomes important. The temperature dependent effective potential method (TDEP) is a method of computing anharmonic properties of materials non-perturbatively from force constants by fitting ab initio MD forces [32, 33]. In this section, we describe in details our implementation of the TDEP technique in reciprocal-space and give results for convergence tests. Real-space TDEP approaches have been implemented in a variety of codes, including the popular`TDEP` [33], `ABINIT` (`A-TDEP`) [105] and `ALAMDODE` (`TEP`) [96]. To the best of our knowledge, our reciprocal-space technique is the first contribution in this regard.

## 4.1 Temperature-dependent effective potential (TDEP)

Temperature-dependent effective potential (TDEP) is a method of computing finite-temperature force constants (FCs) from a sampling of *ab initio* forces. This method was first proposed by Esfarjani and Stokes [32], where the FCs (harmonic, cubic, and quartic) of Si were extracted from *ab initio* MD force-displacement data. Hellman and coworkers [33] introduced a similar procedure, but starting instead with zero-temperature harmonic FCs to obtain the best effective FCs at a given temperature by a least-square fit to *ab initio* MD forces at that temperature.

The TDEP method was tested on entropy-stabilized bcc phases of Zr and Li by Hellman *et al.* [33], and then later extended to treat anharmonic free energy correction in $^4$He [106] and cubic FCs in Si and FeSi [107]. The TDEP formalism starts with a model Hamiltonian

$$H = U_0 + \sum_i \frac{\mathbf{p}_i^2}{2m_i} + \frac{1}{2}\sum_{ij\alpha\beta} \phi_{ij}^{\alpha\beta} u_i^\alpha u_j^\beta, \tag{4.1}$$

where $U_0$ is the ground state energy, and $\mathbf{u}$ and $\mathbf{p}$ denote displacement and momentum, respectively, of atom $i$ ($j$) in Cartesian direction $\alpha$ ($\beta$). Based on the Hamiltonian above, one can define a harmonic approximation of the force $\mathbf{F}^H = -\nabla V$ as

$$\mathbf{F}^H \equiv \mathbf{F}_i^\alpha = -\sum_{j\beta} \phi_{ij}^{\alpha\beta} u_j^\beta. \tag{4.2}$$

The model Hamiltonian in Equation 4.1 is then fitted to a Born-Oppenheimer energy surface, sampled at finite temperature, by minimizing the residual mean squared difference between $\mathbf{F}^H$ and the *ab initio* (Hellman-Feynman) force, $\mathbf{F}^{AI}$, at each time step $t$:

$$\begin{aligned} \chi^2 &= \frac{1}{N_{step}} \sum_{t=1}^{N_{step}} |\mathbf{F}_t^{AI} - \mathbf{F}_t^H|^2 \\ &= \frac{1}{N_{step}} \sum_{t=1}^{N_{step}} |\mathbf{F}_t^{AI} - \Theta\mathbf{U}|^2. \end{aligned} \tag{4.3}$$

The least-square determination of $\mathbf{F}^H$ is then provided by the pseudoinverse solution that gives the lowest residual force:

$$\Theta = \mathbf{U}^\dagger \mathbf{F}^{AI} = \begin{pmatrix} \mathbf{u}_1 \\ : \\ \mathbf{u}_N \end{pmatrix}^\dagger \begin{pmatrix} \mathbf{F}_1^{AI} \\ : \\ \mathbf{F}_N^{AI} \end{pmatrix}.$$

The fitted FCs, $\Theta = \phi_{ij}^{\alpha\beta}(T)$ can then be used to compute temperature-dependent properties. Due to the computational cost of AIMD, stochastically initialized temperature-dependent effective potential (s-TDEP) [34] was proposed in which atoms in a supercell are displaced with a stochastic thermal displacement [108, 38] to allow sampling the canonical ensemble. While s-TDEP enables the inclusion of both anharmonic and quantum effects in a similar fashion to SSCHA [38], its stochastic nature results in phase space that is not necessarily consistent with the requested temperature. In this work, we adopted the Langevin dynamics based on the algorithm by Bussi and Parrinello [39, 6], where instead of using an acceptance probability, as in Monte Carlo algorithms, the additional knowledge of deterministic forces is used to construct a chain of dynamic steps that allows for optimized sampling efficiency.

In the case of polar materials, the long-range contribution to FCs due to dipole-dipole interactions, $\Phi_{ij}^{LR}$, are computed using *ab initio* Born effective charges $\mathbf{Z}^*$, and dielectric constant $\epsilon^\infty$ from density functional perturbation theory (DFPT). Long-range effects are impossible to compute unless one uses a very large supercell. However, it is possible to separate forces into short- and long-range contributions $\mathbf{F}^{AI} = \mathbf{F}^{SR} + \mathbf{F}^{LR}$, and then fit only the rapidly decaying short-range forces $\mathbf{F}^{SR}$. Detail explanation will be provided in Section 4.4.

## 4.2 Our implementation of reciprocal-space TDEP

The temperature-dependent phonon (TDPH) method is a reciprocal space implementation of the TDEP technique described in Section 4.1. Our method is similar to the TDEP

technique described above. However, instead of fitting the FCs directly to *ab initio* forces, we decompose the dynamical matrices $D(\mathbf{q})$ on symmetrized basis $\mathbf{B}_i(\mathbf{q})$ at each $\mathbf{q}$-point [83]. This procedure is inspired to the one used in SSCHA[38] and ensures that an irreducible set of parameters is employed to describe the full phonon dispersion. These minimum phonon parameters (MPP) can be used to recompose the FCs and thus be fitted to the *ab initio* forces.

We will see in Sec. 4.3 how the basis $\mathbf{B}_i(\mathbf{q})$ is built. Here, we detail the fitting procedure, which can be summarized in the following steps:

1. Compute harmonic phonons on a $\mathbf{q}$-grid and decompose the dynamical matrices $D(\mathbf{q})$ on symmetrized basis $\mathbf{B}_i(\mathbf{q})$ at each $\mathbf{q}$-point

$$D(\mathbf{q}) = \sum_{i}^{N_{\mathbf{B}}} c_i(\mathbf{q}) \mathbf{B}_i(\mathbf{q}) \ ,$$

$$c_i(\mathbf{q}) = \langle D(\mathbf{q}) | \mathbf{B}_i(\mathbf{q}) \rangle = \mathrm{Tr}[D(\mathbf{q}) B B_i(\mathbf{q})] \ .$$

2. Read N configurations of AIMD force-displacement data in a supercell ($\{\mathbf{F}_i^{AI}, \mathbf{u}_i\}_{i=1,\dots,N}$), and compute harmonic forces $\mathbf{F}_{i,\alpha}^{H} = -\sum_{j\beta} \phi_{ij}^{\alpha\beta} \mathbf{u}_j^{\beta}$. The supercell size must be commensurate with the phonon $\mathbf{q}$-grid.

3. If polar material, remove the long-range forces $\mathbf{F}^{LR}$ (due to dipole-dipole interaction) from the AIMD forces before fit. $\mathbf{F}^{LR} = -\sum_{uc} \sum_{j\beta} \phi_{ij}^{\alpha\beta(LR)} \mathbf{u}_j^{\beta}$. $\phi_{ij}^{\alpha\beta(LR)}$ is the long-range contribution to FCs due to dipole-dipole interaction defined based on Born effective charges $\mathbf{Z}^*$ and dielectric constants $\epsilon^{\infty}$ using DFPT (see Sec. 4.4).

4. Minimize the residual force by LMDIF (Modified Levenberg-Marquardt) method

$$\chi^2 = \mathtt{min}\left\{ \frac{1}{N} \sum_{i=1}^{N} |\mathbf{F}_i^{AI} - \mathbf{F}_i^{H}|^2 \right\}$$

.

5. Reconstruct the dynamical matrices from the minimal parameters $c_i(\mathbf{q})$.

The procedure outlined above may be applied generally to energy, where harmonic energy, $E^H$, will replace $\mathbf{F}^H$ in *steps 2* and *4* and is defined as $E^H = \sum_{ij,\alpha\beta} \phi_{ij}^{\alpha\beta(LR)} \mathbf{u}_i^{\alpha} \mathbf{u}_j^{\beta}$. In Appendix B, we conducted calculations, and the results for a few test instances were compared. However, it is more efficient to use atomic forces-displacement data since it considerably reduces the number of calculations required to achieve convergence.

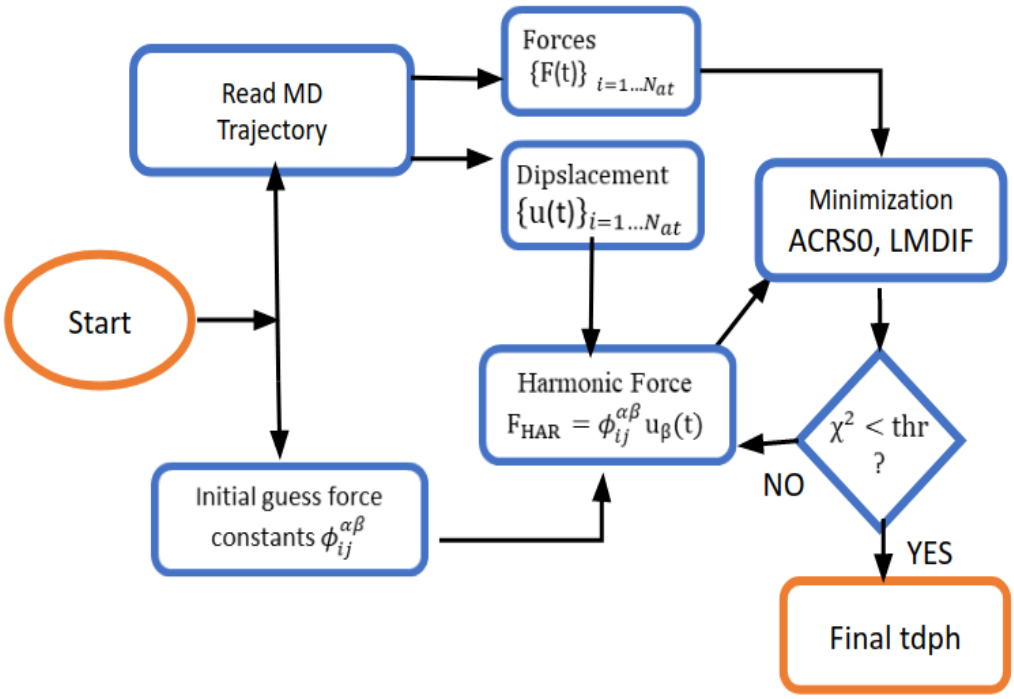


Figure 4.1: A flowchart describing the TDPH procedure is outlined in Section 4.2 using $\chi^2$ as a convergence criteria. The default minimization convergence threshold is 10-12, but can be made stricter.

## 4.3 Symmetric basis for dynamical matrices

The phonon dispersion over a grid of $n \times n \times n$ **q**-points is described by a $3N_{at} \times 3N_{at}$ Hermitian dynamical matrix at each **q**-point in the grid. In order to reduce the dimension of this space from $n^3 \times N_{at}^2$ down to something more manageable, we can use symmetries in two ways. First, we can reduce the grid of **q**-point to its irreducible wedge, i.e. from every set of **q**-points which are linked by a symmetry operation of the crystal, namely a "star of q-points", we only take one. Second, we observe that at each **q**-point the dynamical matrix is fully determined by the subset of symmetry operations that leave the **q**-point unchanged, minus a reciprocal space vector [109].

For every **q**-point in the irreducible wedge, we apply a symmetrization and orthogonalization procedure that from a trial Hermitian matrix of dimensions $N_{at}^2$, with no specific symmetry, returns a minimal orthonormal basis which has the correct symmetry. The symmetrization and orthogonalization algorithm proceeds as follows:

1. Start with an initial guess of Hermitian matrices of dimension $(3N_{at})^2$ for each point in the irreducible list. Possible choices are, random matrices, matrices with a single non-zero element, or matrices constructed from the eigenvectors of the zero-temperature DFPT calculation.

2. The elements of this trial basis are symmetrized, according to the symmetry of the **q**-point. If any element is zero, they are discarded, the others are normalized.

3. Reduce the basis with the Gram-Schmidt algorithm, because the initial basis is over-complete; if a zero-norm element appear during the procedure it has to be discarded.

Finally, what will be left is a set of symmetry-compatible matrices 1,2,...,$N_B(\mathbf{q})$ $\forall$ **q**, such that any dynamical matrix from a simulation of a real crystal at each **q**-point can be decomposed in the following way:

$$D(\mathbf{q}) = \sum_{i=1}^{N_{\mathbf{B}}(\mathbf{q})} \langle D(\mathbf{q}) \mid \mathbf{B}_i(\mathbf{q}) \rangle \, \mathbf{B}_i(\mathbf{q}) \qquad \forall \, \mathbf{q} \in 1\text{BZ}. \tag{4.4}$$

$\mathbf{B}_i(\mathbf{q})$ are the symmetrized basis, defined as the minimal phonon parameters. $N_{\mathbf{B}}(\mathbf{q})$ is also the number of irreducible representation in the point group of **q**. The total number of such parameters is given by

$$N_{\mathbf{B}} = \sum_{\mathbf{q}} N_{\mathbf{B}}(\mathbf{q}) \tag{4.5}$$

In practice, $N_{\mathbf{B}}$ is significantly smaller than $(3N_{at})^2$ and can be as small as 4 for highly symmetric crystals such as fcc Al on $2 \times 2 \times 2$ **q**-grid. Table 4.1 below gives the phonon parameters of different materials. The number of phonon parameters $N_{\mathbf{B}}$, depends on the symmetry of the crystal structure and the size of the phonon **q**-grid (which determine the size of the supercell in real space). For instance, $N_{\mathbf{B}}$ of *orthorhombic* $MgSiO_3$ is 19 times bigger than that of *cubic* MgO, although the latter have 1.6 times more atoms than the former.

Table 4.1: Size dependence of phonon parameters for a 5,000 MD snapshots. Space group (SG), supercell size, number of atoms in supercell ($N_{at}$), minimal phonon parameters ($N_{\mathbf{B}}$), *ab initio* forces for $N_{steps}$ ($F_{AI}$), and `TDPH`$_{\texttt{time}}$ CPU time (Machine specification: Personal computer with 2.20GHz (x12) Intel Core i7-8750H ).

| System | SG | Supercell | $N_{at}$ | $N_{\mathbf{B}}$ | $F_{AI}$ | `TDPH`$_{\texttt{time}}(s)$ |
|---|---|---|---|---|---|---|
| Al | *Fm3m 225* | $(2 \times 2 \times 2)$ | 8 | 4 | $2.00 \times 10^5$ | 3 |
| CsI | *Pm3m 221* | $(2 \times 2 \times 2)$ | 16 | 13 | $1.20 \times 10^5$ | 9 |
| Zr | *Im3m 229* | $(4 \times 4 \times 4$ | 64 | 17 | $9.60 \times 10^5$ | 3 |
| $SrTiO_3$ | *Pm3m 221* | $(2 \times 2 \times 2)$ | 40 | 49 | $6.00 \times 10^5$ | 42 |
| MgO | *Fm3m 225* | $(4 \times 4 \times 4)$ | 128 | 51 | $1.92 \times 10^6$ | 98 |
| $MgSiO_3$ | *Pbnm 62* | $(2 \times 1 \times 2)$ | 80 | 994 | $1.20 \times 10^6$ | 28152 |
| $CeMoN_3$ | *R3c 161* | $(2 \times 2 \times 2)$ | 80 | 2720 | $1.20 \times 10^6$ | – |

## 4.4 Dealing with polar materials

In polar materials, the long-range nature of the Coulomb forces is responsible of a macroscopic electric field for longitudinal optical phonons (LO), giving rise to the LO-TO splitting

as $\mathbf{q} \to 0$ [18]. Thus, in polar crystals, the force constants can be separated into an exponentially decaying short-range part $\Phi^{SR}$, and a long-range dipole-dipole term $\Phi^{LR}$ [15, 110] that decays polynomially ($\sim d^{-3}$, where $d$ is the interatomic distance):

$$\Phi_{ij}^{\alpha\beta} = \Phi^{SR} + \Phi^{LR}. \tag{4.6}$$

The long-range FCs are given by the general form in terms of the Born effective charge tensor $\mathbf{Z}_i^*$ of the $i$-th atoms in a unit cell and the macroscopic dielectric tensor $\epsilon^{\infty}$ which can be routinely computed within DFPT [18, 111, 112]

$$\Phi^{LR} \equiv \phi_{ij}^{\alpha\beta(LR)} = \frac{4\pi e^2}{\Omega} \frac{(\mathbf{q}\cdot\mathbf{Z}_i^*)_\alpha (\mathbf{q}\cdot\mathbf{Z}_j^*)_\beta}{\mathbf{q}\cdot\epsilon^{\infty}\cdot\mathbf{q}} \tag{4.7}$$

Although the description of the $\Phi^{LR}$ in terms of the dipole-dipole term yields accurate results in the majority of materials, it has been demonstrated that generalizing to higher order multipolar terms is required in some cases [113]. From Equation 4.6, the atomic forces can also be separated into short-and long-range terms

$$\begin{aligned} \mathbf{F}^{AI} &= \mathbf{F}^{SR} + \mathbf{F}^{LR} \\ &= -\sum_{j\beta} \Phi_{ij}^{\alpha\beta,SR} \mathbf{u}_j^{\beta} - \sum_{j\beta} \Phi_{ij}^{\alpha\beta,LR} \mathbf{u}_j^{\beta} \end{aligned} \tag{4.8}$$

Following Ref. [114, 115], the short-range FCs, $\Phi^{SR}$, are fitted to the short-range forces $\mathbf{F}^{SR}$ only (see Figure 4.2 for comparison to DFPT and TDPH in handling with polar and non polar crystals ). The effective charges $\mathbf{Z}^*$ and dielectric constants $\epsilon^{\text{inf}}$ are computed in a unit cell, therefore, $\mathbf{F}^{LR}$ is summed over all the unit cells in the supercells

$$\mathbf{F}^{LR} = -\sum_{uc}\sum_{j\beta} \Phi_{ij}^{\alpha\beta,LR} \mathbf{u}_j^{\beta} \tag{4.9}$$

Long-range effects on FCs require a very large supercell, which is not feasible in practice. We tested fitting the effective charges (the long-range forces) and observed weak temperature dependence. This is expected since any change in $\mathbf{Z}^*$ would require a considerable change in the electronic structure (which can be treated at the QHA level), but the temperature does not significantly affect the electronic occupations. Note that Eq. 4.7 is in reciprocal space, in order to bring it to real space we compute it for $\mathbf{q} = 0$ in the supercell dual to the $\mathbf{q}$-grid.

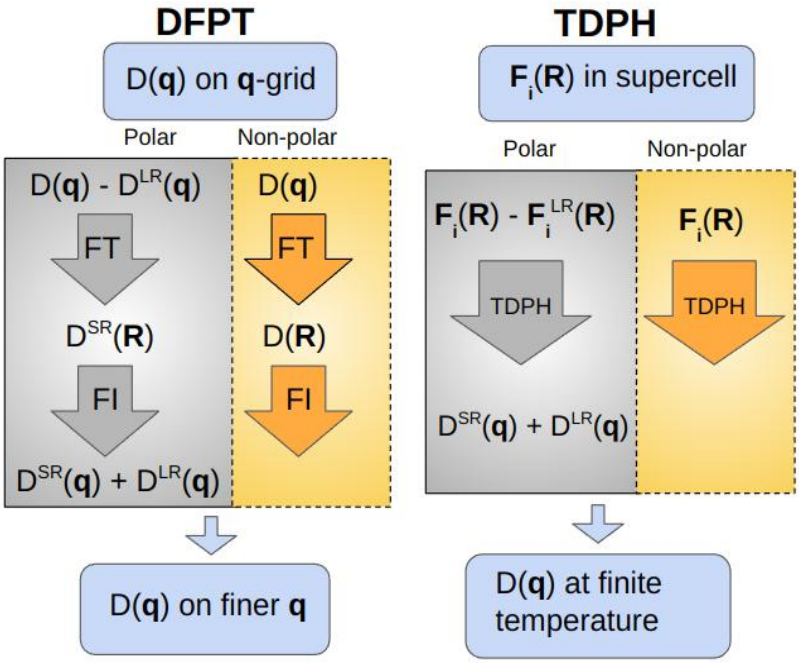


Figure 4.2: Comparison of DFPT and TDPH for polar and non-polar crystals

## 4.5 Features of TDPH

The initial guess for FCs could come from DFPT or frozen phonons in a supercell. In the case of DFPT, this implies, among other factors, handling polar materials in one integrated way without the need for a separate or complementary calculation of the long-range dipole-dipole term. For this reason, no arbitrary real-space cutoff has to be imposed to keep the calculation fast. We have verified that after starting with initial symmetric random phonon parameters the fitting procedure converged to the correct result in all of our test cases. In principle, it is possible to start with no initial guess at all (other than the crystal geometry).

As we have described in Sec. 4.3, the dynamical matrices are decomposed on a set of symmetrized minimal basis at each **q**-point in the 1BZ, whose linear coefficients are the parameters that are minimized during the fitting. Thus, this reciprocal-space approach is highly efficient and ensures very fast convergence.

Effective charges can be considered fixed or minimized. We verified that finite temperature effects on the effective charges beyond the QHA level are vanishingly small.

TDPH, as part of the D3Q [84] code, is fully integrated into the Quantum Espresso (QE) package [116, 117], which computes both FCs and MD configurations. This unique synergy, as well as faster convergence, makes it easier and more efficient to compute anharmonic properties. To decorrelate more quickly the sampled configurations, TDPH can be integrated with both classical and quantum Langevin dynamics, the latter implemented via the PIOUD engine [73] (also based on QE) which is currently still in closed development.

## 4.6 Numerical minimization

As we have seen in Table 4.1, the number of phonon parameters can be of the order of 1000 for relatively large systems, which may require a few thousand MD steps for the TDPH procedure to accurately converge. The Levenberg-Marquardt[118, 119] minimization algorithm needs to solve linear least squares problems repeatedly. More precisely, this means finding a vector $x$ that minimizes $\|Ax - b\|$, where $A$ is a rectangular matrix of dimension $N_p$ (number of parameters) times $N_{data} = 3 \times N_{at} \times N_{steps}$ (number of Cartesian direction, atoms in the supercell, and of steps, respectively). The latter can be of the order of one million. Solving linear least square problems is done by computing a QR factorization of the matrix — this is the most computationally expensive step. This takes hours using the naive serial algorithm implemented in MINPACK [45]. For this reason, we parallelized the existing sequential MINPACK package from 1980. The main modification consists in using ScaLAPACK [46] to compute QR factorizations. The implementation we used, minimizes the $N_{data}$ residual forces simultaneously, using their gradient from numerical differentiation. The algorithm is very robust and can converge, even from randomly initialized FCs, in a few (typically less than 10) iterations.

## 4.7 Convergence Tests

The decay time of autocorrelation is the most important parameter in determining the efficiency of a dynamic algorithm to provide thermodynamic sampling. For instance, if the MD steps remain correlated for a long time, then more steps need to be sampled and this will eventually skyrocket the computational cost. Weakly correlated configurations, on the other hand, imply that less computing time will be sufficient to sample the PES by keeping the same target accuracy. Finite-size effects, MD integrators, and thermostats are other factors worth observing. Therefore, we perform the following convergence tests:

- Study the performance of TDPH (i.e. convergence of phonon frequencies, $\chi^2$,for a given set of minimal phonon parameters $N_{\mathbf{B}}$) with sampling time

$$\tau_{\texttt{sampling}} = \texttt{n\_skip} \times dt \ , \tag{4.10}$$

  where $dt$ is the AIMD time step and `n_skip` is the sampling interval.

- Compare the TDPH results for different supercell sizes.

- Study the dependence of the sampling efficiency on $\tau_{\texttt{sampling}}$ in MD versus LD, and the optimal $\tau_{\texttt{sampling}}$ to achieve reasonable convergence for properties of interest in both cases.

- Universality of FCs fitted over different dynamics methods.

Note that from a numerical point of view, what matters is to have `n_skip` as small as possible, i.e. to use the computed DFT data efficiently. This can be achieved by increasing the time step, but if it is too large, other properties of the simulation will suffer: the simulation temperature may go out of control, or a bias could be introduced. We will see these points in detail as we study specific cases.

### 4.7.1 Convergence of phonons with AIMD sampling

Taking a simple example as a benchmark, we examine the phonon frequency convergence by sampling 200 MD snapshots over different simulations lengths (corresponding to five different sampling times: $\tau_{\texttt{sampling}} = 0.1, 0.2, 0.5, 1.0$ ps) at 300K. Details of calculations are provided in Appendix A. As shown in Figure 4.3, the phonon spectra converged at $\tau_{\texttt{sampling}} = 0.2$ps for a $2 \times 2 \times 2$ fcc Al supercell.

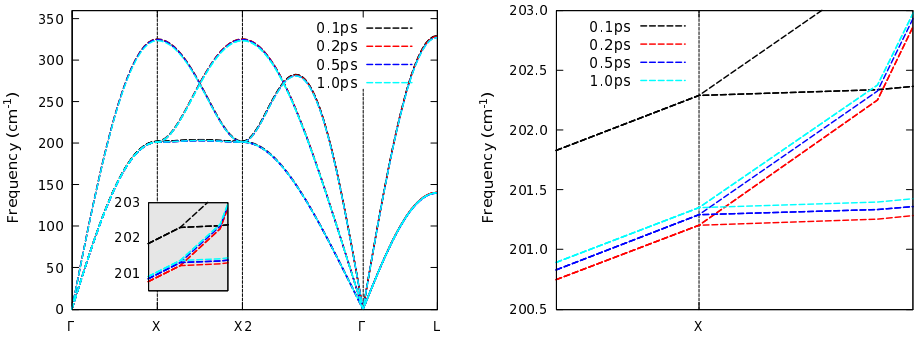


(a) (b)

Figure 4.3: Convergence of phonon spectra with respect to the AIMD correlation time. The full phonon dispersion is given in panel (a) and zoomed-out around X in panel (b)

As a way to check how TDPH improves the description of atomic forces, we compare the *ab initio* and harmonic forces before and after fitting the configurations along the MD trajectory. In Figure 4.4, this exercise is done for 400 AIMD snapshots. Before the fit, the harmonic forces deviate from the *ab initio* ones represented by the dashed circles. After fitting, the TDPH forces become closer to the *ab initio* determination. Figure 4.4 gives the same result at 775K. We observe that the *ab initio* and model forces are closer at a lower temperature (300K), Figure 4.4(a), than at a higher temperature (775 K), Figure 4.4(b). The residual spread around the *ab initio* reference (red line in Fig. 4.4) gives an idea of the system anharmonicity.

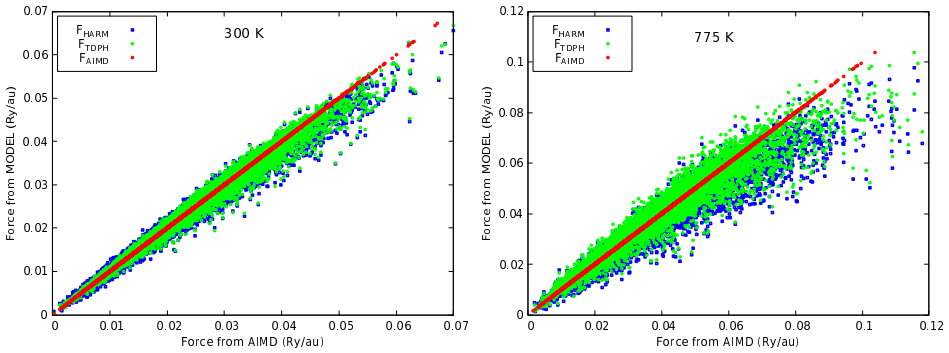


(a) (b)

Figure 4.4: Comparison of the modulus of AIMD force and model (harmonic and TDPH) forces at 300 K (panel (a)) and at 775 K (panel (b))

.

We also examine the robustness of phonon convergence with respect to arbitrary initial conditions, by analyzing different randomly initialized MD runs. Two configurations (system I and II) were initialized with different random atomic velocities, and the TDPH phonons were compared. The result is shown in Figure 4.5, where a nice agreement is found between the two calculations.

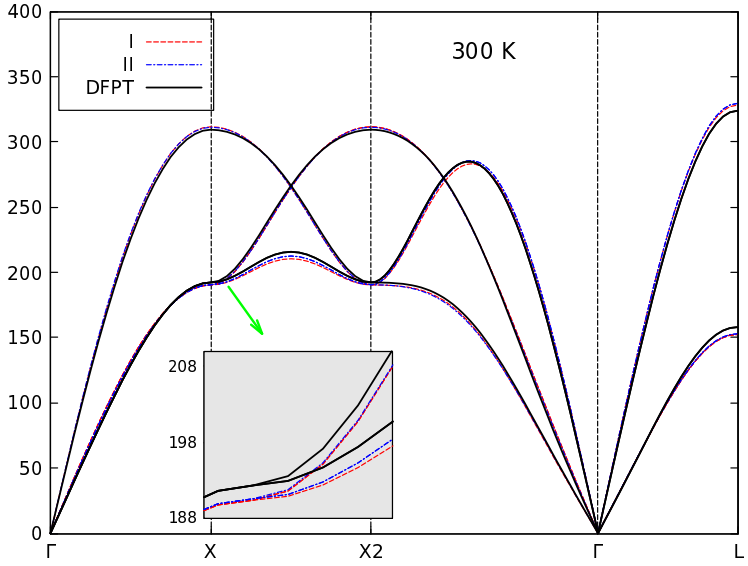


Figure 4.5: Comparison of phonons dispersions from two randomly-initialized MD simulations and DFPT for a $3 \times 3 \times 3$ Al supercell.

### 4.7.2 Phonon parameters versus supercell Size

We test the TDPH performance with different supercells to examine the dependence of the number of phonon parameters $N_{\mathbf{B}}$ on the supercell size. Different supercells were considered using the same temperature, i.e. $T = 300K$, and same correlation time, namely $\tau_{\texttt{sampling}} =$

0.2$ps$. The result for fcc Al is given in Table 4.2. Also shown in Figure 4.6, is the dependence of $N_{\mathbf{B}}$ on the number of atoms corresponding to different supercell sizes. Note that larger supercells do not necessarily require longer simulations time, since the ratio $N_{F_{AI}}/N_{\mathbf{B}}$, where $N_{F_{AI}}$ is the number of force components in the supercell, does not change significantly, thanks to the full exploitation of symmetry relations in TDPH.

Table 4.2: Phonon parameters versus supercell size in Al.

| Supercell | $N_{at}$ | $N_{\mathbf{B}}$ | $N_{F_{AI}}$ | $N_{F_{AI}}/N_{\mathbf{B}}$ |
|---|---|---|---|---|
| $2 \times 2 \times 2$ | 8 | 4 | 24 | 6 |
| $3 \times 3 \times 3$ | 27 | 7 | 81 | 11.6 |
| $4 \times 4 \times 4$ | 64 | 17 | 192 | 11.3 |
| $6 \times 6 \times 6$ | 216 | 45 | 684 | 14.4 |
| $8 \times 8 \times 8$ | 512 | 94 | 1536 | 16.3 |

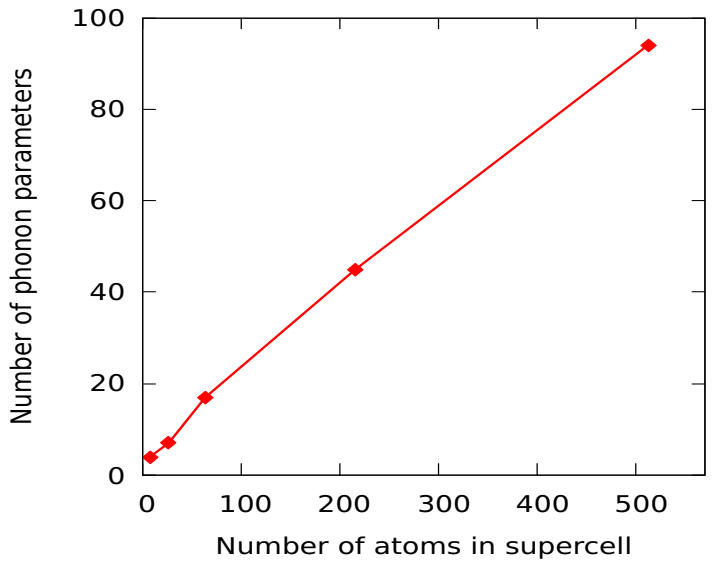


Figure 4.6: Dependence of the number of phonon parameters $N_{\mathbf{B}}$, on the number of atoms $N_{at}$, for Al as reported in Table 4.2 .

### 4.7.3 Convergence of phonon parameters with PES sampling

As described in Section 3, two schemes were employed to sample the PES in the NVT ensemble, namely MD and LD. For MD, a stochastic velocity rescaling (SVR) thermostat was used, since it has been shown to have no effects on dynamical and transport properties [70] (see Appendix A for computational details).

The second method is the classical Langevin dynamics (LD), which integrates the equations of motion with deterministic (in our case DFT-based) and stochastic forces at a given temperature, stabilized by an appropriate friction, determined though the FDT. It is based on Bussi and Parrinello algorithm [39, 6] using a Trotter factorization of the Liouvillian

operator, as already described in Section 3 and Ref. [73]. Within this formalism, fully anharmonic quantum dynamics can be investigated. By replacing LD with PILD, it is possible to take into account both temperature and nuclear quantum effects (NQE), as recently demonstrated in diamond and high-pressure atomic phase of hydrogen [6]. For our purpose, only thermal effects are considered and the classical LD algorithm is used, since NQE are less significant at higher temperature in the systems studied here. As shown in Figure 4.7(a), for weakly anharmonic materials like fcc Al, both MD and LD give reasonably converged phonons with fewer (i.e. $\sim 100$) snapshots and no interval between subsequent steps (i.e. using $\tau_{\texttt{sampling}} = 1$). In the case of cubic $SrTiO_3$, a strongly anharmonic perovskite, each dynamic simulation gives converged phonons only when an *appropriate* sampling time is used. We choose this sampling time to be the autocorrelation time $C(t, t')$ of the *ab initio* energy (see Appendix C). Using a large time step can considerably reduce $C(t, t')$ (and hence computation time) at the expense of large temperature fluctuations, but this impact is more pronounced in MD. In the case of LD, FDT guarantees that temperature and friction are coupled, keeping the temperature near to its intended value.

For a material with dynamical instability, finite-temperature sampling of the PES with NVE will directly descend to the minima and hence give fast convergence of those parameters that correspond to soft phonons. However, sampling the PES using NVT (LD or MD with SVR thermostat) will allow the system to explore the phase space more exhaustively before descending into the minima. They are therefore more ergodic than NVE. In both cases, the effective harmonic Hamiltonian is constructed to give converged phonon parameters and phonon dispersion representative of the sampling temperature. Figure 4.7(b) displays the comparison of phonon dispersions yielded by the three different methods.

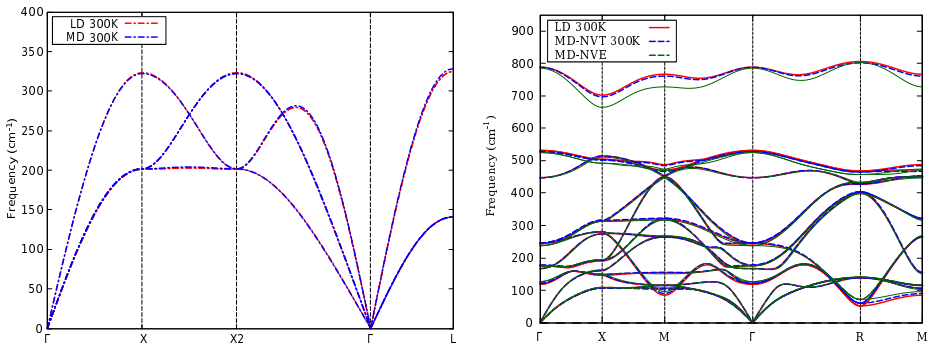


(a) (b)

Figure 4.7: Temperature-dependent phonon dispersion at 300K for fcc Al (panel (a)) and cubic $SrTiO_3$ (panel (b)) using LD (red line), MD-NVT (blue-dotted line) and MD-NVE (dark-green dotted line).

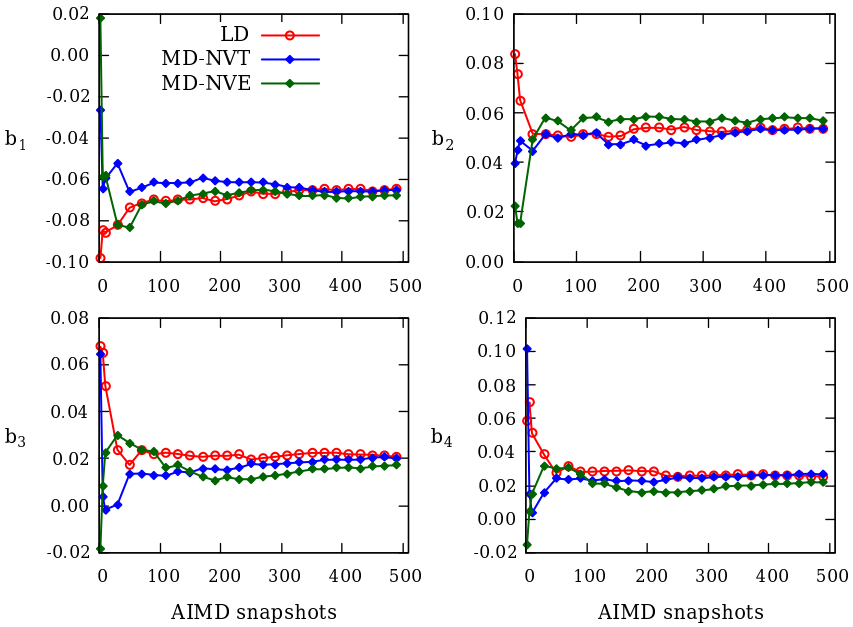


Figure 4.8: Convergence of the first four phonon parameters in $SrTiO_3$ with TDPH minimization steps. All methods are in a reasonable agreement after a 2ps long simulation, with LD yielding the smoothest convergence as a function of the number of AIMD snapshots.

### 4.7.4 Universality of the FCs in different dynamics

Another factor to take into account is the absence of sampling bias and the ergodicity of the dynamics trajectory i.e. the property of the trajectory to sample the phase space in a way that is consistent with the thermodynamic average. To ascertain this property, we cross-tested FCs from the different dynamics methods (LD, MD- NVT, MD-NVE). To do so, on the one hand we define $\chi^2_{fit}$ of the FCs as the value of $\chi^2$ obtained at the end of the minimization (step 5 in the procedure we detailed at the beginning of Sec. 4). On the other hand, we define $\chi^2_{test}$ as the $\chi^2$ value obtained by applying the FC obtained on a given trajectory to a different trajectory, without further minimization. If there is no sampling bias, $\chi^2_{fit}$ and $\chi^2_{test}$ should be very close.

Our assumption is that a good quality trajectory produces universal TDPH FCs, which would work equally well on any other trajectory, i.e. $\chi^2_{fit}$ from a good trajectory should not be significantly smaller than that obtained by applying the final FCs to *a different* trajectory.

Conversely, the fact that the $\chi^2$ obtained from a trajectory is too small, does not imply that the trajectory is good. In the best case it indicates that the system is weakly anharmonic, while in the worst case it suggests that the sampling has a bias. This last point is particularly important: a biased trajectory, which does not explore the entire phase space, may have a smaller $\chi^2$, as the phonon parameters that describe the unexplored degrees of freedom will be unconstrained.

Figure 4.9 gives a measure of the universality of FCs in $SrTiO_3$ extracted with the TDPH method from different dynamics: LD, MD-NVT, MD-NVE. In each case, the tested chi-square ($\chi^2_{test}$) is rescaled by the baseline ($\chi^2_{fit}$). For a sufficiently large number of steps, all three methods seem to give comparable results. We remark however that a tiny difference

remains between LD and NVT, which may indicate an equally tiny bias in the exploration of the phase space. On the other hand, there is a larger discrepancy between the uncontrolled NVE and the two other methods. The fact that the NVE $\chi^2$ is higher (panel d of Figure 4.9) indicates that it explores a less harmonic region of the phase space.This seems in contradiction with the NVE property of exploring the PES minima more frequently than the other dynamics. In fact, we have verified that, for this specific test, the average temperature of the NVE simulation drifts from the initial one and settles around 315 K. This is because, in a microcanonical ensemble, the total energy drifts due to error accumulation from the MD integrator, which tends to increase with simulation length [120]. This discrepancy can be particularly problematic when studying the temperature evolution of a system, or when volume expansion is taken into account non-self consistently (i.e. from the equation of state), which is the most common approach. Nevertheless, the temperature drift of NVE can be mitigated by using the average temperature instead of the target one, or by repeating the simulation until the correct temperature is achieved, but this is expensive and labor-intensive. Therefore, it turns out that using a stochastic thermostat can achieve a good result in a much simpler and efficient way.

We can conclude that all methods produce universal FCs, but NVT and LD are more accurate and consistent to each other, as the real trajectory temperature is consistent with the desired one (299 K for LD and 298 K for NVT). The $\chi^2$ of the NVE simulation remains consistently higher, which is related to the fact that, for this specific test, the effective temperature reached in NVE was larger, leading to the exploration of a more anharmonic region.

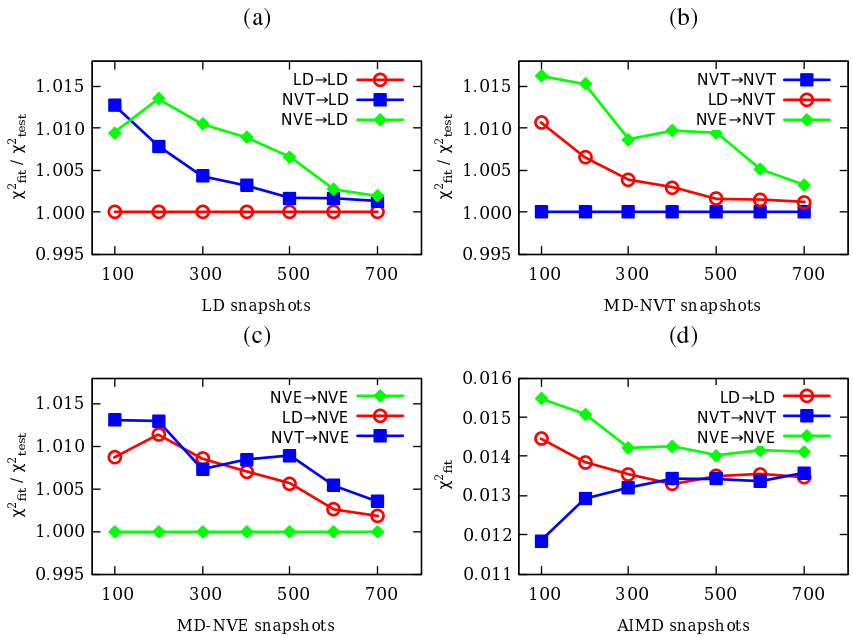


Figure 4.9: Measure of the universality of FCs extracted via TDPH from different dynamics. Horizontal lines are obtained by the baseline dynamics that generates the ensemble against which each set of FCs is tested. Red, blue and green lines indicate FCs fitted on LD, MD-NVT, and MD-NVE trajectories, respectively.

In order to speed up phase-space sampling and convergence of phonon parameters, especially in the case of crystals with low symmetry, the TDPH method can benefit from AIMD with machine learning force interatomic potentials (MLIP). Generally, MLIP are based on descriptors or features that represent the local atomic environment and a regression model (e.g. from artificial neural networks, kernel-based methods, or linear regression). In this context, our method is a kind of machine learning "linear regression" technique, where the "descriptors" for the atomic forces are defined by the effective harmonic force constants with the symmetrized phonon parameters serving as the "fitting coefficients", in contrast to hyperparameters in the other mentioned methods. The initial application of TDEP method as established by Esfarjani was indeed to be used as a force field [121].

### 4.7.5 Randomization of phonon parameters

The decomposition of the dynamical matrices on symmetrized phonon basis described in Section 4.1 gives yet another opportunity to examine TDPH's dependence on the values of the phonon coefficient. The choice of the basis coefficients, for example, is not unique, and the initial estimate of the force constant may differ from the harmonic one. As a result, we add or remove to each coefficient, a randomization parameter $\zeta$, such that Eq. 4.4 becomes

$$\begin{aligned} D(\mathbf{q}) &= \sum_{j}^{N_\mathbf{B}} c_j^r(\mathbf{q})\mathbf{B}_j(\mathbf{q}) \\ c_j^r(\mathbf{q}) &= 2\ b_j(\mathbf{q})(\texttt{rand} - 0.5) \end{aligned} \tag{4.11}$$

where

$$b_j(q) = \frac{2\sum_j^{N_\mathbf{B}} |c_j(\mathbf{q})|}{N_\mathbf{B}|\zeta|}$$

and `rand` is a random number generator between 0 and 1.

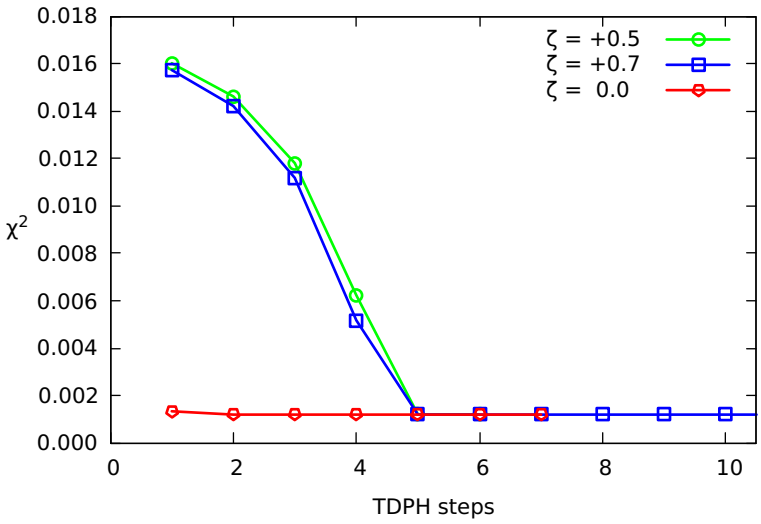


Figure 4.10: Convergence of $\chi^2$ with TDPH minimization steps for different (initial) randomization of phonon parameters.

In Figure 4.10, we show the convergence of $\chi^2$ for different randomization parameters with TDPH minimization steps. At the 5th iteration, the randomized curves converged to the case initialized with harmonic FCs. In order to generate randomized FCs matrices, initial guess of harmonic FCs (T= 0 K) from DFPT are decomposed on $c_j$ and then recomposed on $c_j^r$, without minimization. The phonon dispersion corresponding to these randomized FCs are presented in Figure 4.11.

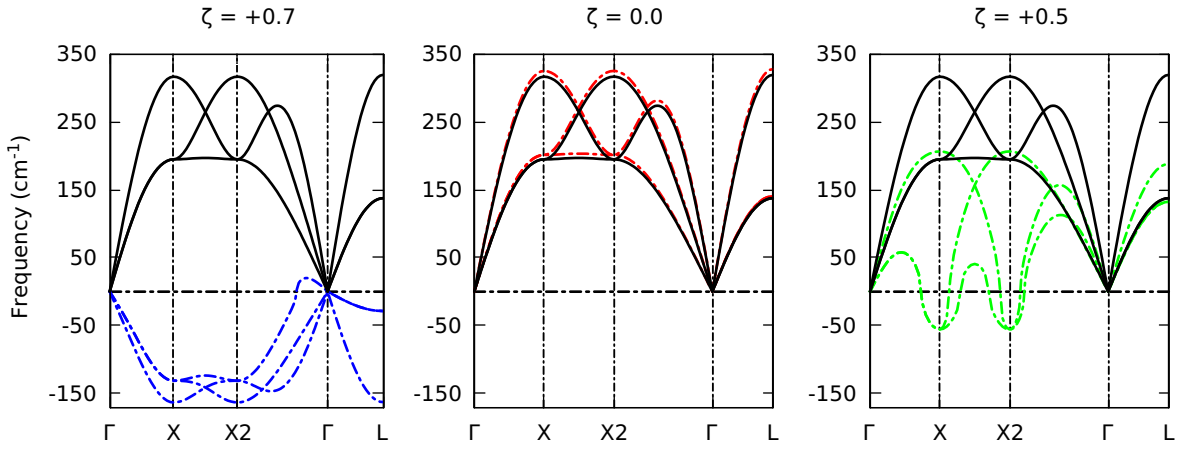


Figure 4.11: Phonon dispersion of Al using different initial values of randomization of the phonon parameters before fit: left (-0.2), right (+0.5). Black curves indicate harmonic phonons, while red dotted lines indicate TDPH phonons at 300K.

We observed that the TDPH algorithm always converges to the same final phonon parameters irrespective of the choice of the initial randomization, with the only cost being additional computing time ( 10% in the case of Al). This is particularly useful when comparing FCs from various methods using the same sampling of the PES (e.g. Section 4.7.3) or when the initial guess of the FCs is unknown a priori (e.g., with a machine learning force field). In the latter case, finding the right balance between underfitting and overfitting while training a machine learning model to make predictions constitute a difficult task. In the first principles characterization of material properties, one can finetune the model's predictions to be physically meaningful by incorporating physical intuition, often through descriptors, into the machine learning algorithms. This ensures that the model is not overfitting to the training data and can generalize to new parts of the chemical space. In the TDPH method, once the crystal symmetry is defined, the phonon parameters provide a sufficient description of the dynamical matrices, and TDPH can converge these parameters to their final values (even when initially randomized) by fitting to ab initio forces. The randomization of phonon parameters may indicate how far the initial atomic forces are from their optimal values.

## 4.8 Comparison of TDPH to other anharmonic methods

### 4.8.1 Computational details

Here we compare TDPH with other anharmonic phonon renormalization methods (PRM): the velocity autocorrelation function (VACF) method of Zhang-Sun-Wentzcovitch, [28, 122], and the self-consistent phonon (SCPH) method of Tadano-Tsuneyuki [96]. DFT calculations were performed using generalized gradient approximation (GGA) with the Perdew-Burke-Ernzerhof (PBE) exchange-correlation functional and Vanderbilt ultrasoft pseudopotentials for the interaction between valence and ionic core. Plane-wave basis were used to expand the Kohn-Sham electronic wavefunction limited with a cutoff energy of 30 Ry and Monkhorst-Pack **k**-points grid the depends on the size of the supercell (8×8×8 for 8 atoms supercell in TDPH and VACF and 4×4×4 for 32 atoms supercell in SCPH calculations.) Both TDPH and VACF results were obtained from the same trajectory generated using AIMD and stochastic velocity rescaling thermostat [70] at 775 K and 1 fs time step. Also, both TDPH (Thermal2+D3Q code [84]) and VACF (phq code [122]) are fully implemented in the Quantum espresso package.

There are multiple stages to the SCPH technique in the ALAMODE code, starting with creating training data and ending with solving the SCP equation for phonons. Using the same parameters as in TDPH and VACF above, AIMD is run for the 2×2×2 supercell (32 atoms) of the conventional fcc Al unit cell. A total of 100 independent AIMD configurations were extracted from the last 3000 steps of the 3,700 and then each atom is displaced randomly by 1 A in all directions. Finally, single point DFT calculation is performed on the 100 displaced configurations and used as a training set to extract force constants using the Elastic-net [10][123] technique based on the optimization equation

$$\Phi^{enet} = \frac{1}{2N_c}||\mathbf{F}^{DFT} - \mathbb{A}\Phi||_2^2 + ab||\Phi||_1 + \frac{1}{2}a(1-b)||\Phi||_2^2 \tag{4.12}$$

where $a$ and $b$ are hyperparameters obtained from cross-validation.

### 4.8.2 Results

In Figure 4.12, we report the phonon spectra of Al computed with TDPH, VACF, and SCPH methods along the high-symmetry direction within the first Brillouin zone (1BZ). In all three methods, effective harmonic force constant matrices (and dynamical matrices) are built by explicitly accounting for temperature dependence and subsequently diagonalized to obtain phonon spectra and other vibrational and thermodynamic properties. The TDPH and VACF methods yield renormalized phonons at a temperature of 775 K in close agreement because both methods use the same trajectory or sampling of the PES. Specifically, TDPH fits force-constants force contents to ab initio force-displacement data, while VACF relies on atomic displacement/velocity projected to harmonic polarization vectors. Noticeable deviation of the SCPH results in phonon dispersion observed along X-W, which is attributable to a different sampling of the PES and the renormalization of phonons by 4th-order force constants in the SCPH technique. In Figure 4.13 , the DOS of SCPH is rescaled by a factor of 0.5 to account for the bigger supercell (32-atom supercell in SCPH compared to 16-atom supercell in TDPH and VACF). Except for the small broadening of the peak between 200 $cm^{-1}$ and

250 $cm^{-1}$ in SCPH, all three approaches provide comparable density of states (DOS) with identical peak positions. Generally, all three methods give similar results that agree with each other.

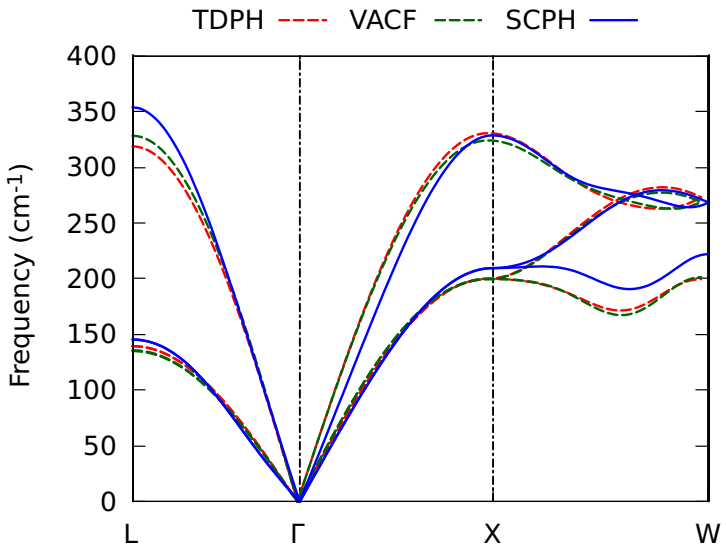


Figure 4.12: Anharmonic phonon spectra of fcc Al at 775 K using three different phonon renormalization methods. Dispersion curves computed from TDPH, VACF, and SCPH are depicted by red dashed lines, green dashed lines, and blue solid lines, respectively.

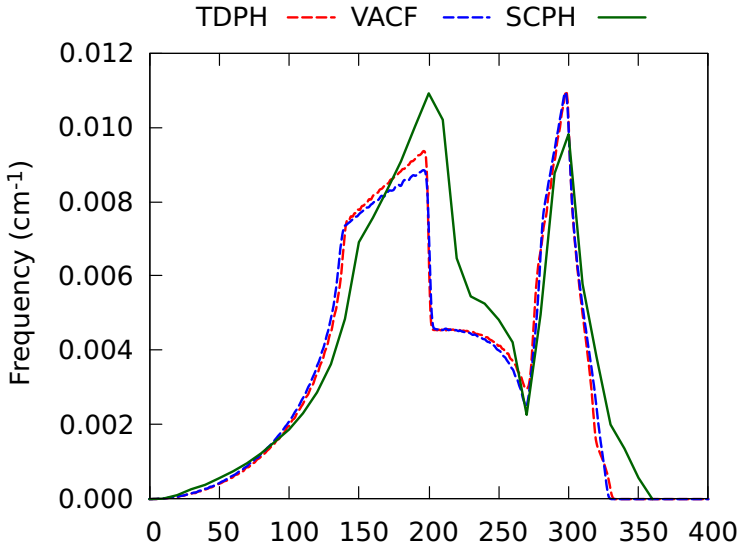


Figure 4.13: Phonon dispersion curve of fcc Al at 775 K using TDPH (red), VACF (green) and SCPH (blue). Although the SCPH result is rescaled by a factor 0.5, the three methods give DOS with qualitatively similar trend.

### 4.8.3 Performance

We compare the performance of three anharmonic phonon method codes using fcc Al as an example: SCPH in the `ALAMODE code` , VACF in the `phq code`, and TDPH in the `D3Q` + `thermal2 code`. The TDPH method is considerably more efficient than the other two. Table 4.3 shows that the minimization time for VACF and SCPH are two orders of magnitude longer than that for TDPH. The SCPH time includes 4-fold cross-validation for the elastic net, optimization of force constants, and the solution of the self-consistent equation for phonons. Pre- and post-processing time in all three cases is excluded. However, The most computationally expensive part of all the three methods is the time to sample the DFT potential energy surface ($5^{th}$ column of Table 4.3). SCPH has the advantage that the finite temperature phonons can be obtained at all temperatures once the training data is generated.

Table 4.3: Comparison of the performance of TDPH, VACF, and SCPH methods in fcc Al. $\mathtt{t}_{\mathtt{DFT-PES}}$ is the total time to generate trajectory or sample the potential energy surface in hours, and $\mathtt{t}_{\mathtt{method}}$ is the time required to obtain renormalized phonons at 775 K.

| Method | # of atoms in supercell | $\mathtt{t}_{\mathtt{DFT-PES}}$ (h) | $\mathtt{t}_{\mathtt{method}}$ (s) |
|---|---|---|---|
| TDPH | 8 | 117 | 3 |
| VACF | 8 | 117 | 112 |
| SCPH | 32 | 3008 | 394 |

### 4.8.4 Conclusion

We have compared the results and performance of 3 different anharmonic phonon methods codes using fcc Aluminum as a test case. The results for the phonon dispersion and density of states obtained using the SCPH implemented in `ALAMODE code`, the VACF method implemented in the `phq code`, and our new TDPH method implemented the `D3Q` + `thermal2 code` of QUANTUM ESPRESSO , are in close agreement with each other. We find that TDPH outperform the other two methods, but the most resource consuming aspect remains sampling the PES.

## 4.9 Summary

The temperature-dependent phonon (TDPH) method builds effective harmonic potential that accounts for anharmonicity non-perturbatively. It relies on decomposing dynamical matrices into a symmetrized basis at each **q**-point in reciprocal space, ensuring an irreducible set of phonon parameters is used to represent the phonon dispersion. The trial harmonic force constants are fitted via harmonic forces to ab initio force-displacement data in a supercell, obtained from molecular or Langevin dynamics, where the residual force is minimized using the Modified Levenberg-Marquardt method. Convergence tests evaluate the efficiency of TDPH by studying phonon frequencies, comparing results for different supercell sizes, and examining the dependence of sampling efficiency on different ensembles. TDPH scales favorably with large supercells of highly symmetric materials and converges despite different initial randomization of phonon parameters. Compared to other anharmonic methods, in

Section 4.8, TDPH outperforms VACF and SCPH. Overall, TDPH demonstrates robustness, efficiency, and universality across different dynamical methods, making it a promising approach for understanding anharmonic properties in materials. The chapters that follow will focus on application of the TDPH method to materials that exhibit weak and strong anharmonicity.

# 5 – Anharmonic correction to QHA phonons in Al

## 5.1 Introduction

Although fcc Aluminum exhibits weak anharmonicity, it is desirable to understand the degree to which quasiharmonicity and intrinsic anharmonicity affects phonon frequencies. Within the harmonic approximation, the effect of temperature is absent and phonons have infinite lifetimes. Quasiharmonic approximation (QHA) introduces temperature dependence via volume (thermal expansion) which tends to shift phonons as temperature is increased. QHA is the most popular *ab initio* method of computing thermodynamic properties of materials [20]. Due to its simple structure and large number of experimental and theoretical studies of its properties, fcc Aluminum is used to demonstrate the effectiveness of computational techniques [3, 124, 125, 126]. In many materials, including Aluminum, phonons become softer at higher temperature as observed in several experimental and theoretical studies [3]. To what degree do the anharmonic phonon frequencies change from their harmonic and quasiharmonic values at higher temperature? To answer this we apply both QHA and TDPH method to Aluminum and compare the results to experiment.

## 5.2 Computational details

DFT calculations were performed with ultrasoft pseudopotentials [127] and generalized gradient approximation (GGA) with Perdew, Burke and Ernzerhof (PBE) exchange-correlation energy [128], implemented in Quantum espressopackage [116, 129]. The plane wave cutoff energy for Al is 30 Ry and Monkhorst-Pack [130] k-points grid of $8 \times 8 \times 8$. A cold smearing [131] width of 0.05 Ry was used. Harmonic FCs were computed using DFPT [18] on a $2 \times 2 \times 2$ $\mathbf{q}$-grid. *Ab initio* MD simulations were performed using NVT ensemble with supercell size commensurate with the phonon grid (i.e. $2 \times 2 \times 2$ $\mathbf{q}$ containing 8 atoms). Temperature is controlled with stochastic velocity rescaling method [70] and a time step of 1 fs. We tested the variation of phonons with larger time step up to 100 fs, and the effects on TDPH phonons is not significant.

For the QHA calculations, 9 lattice volumes were chosen with five different volumes corresponding to the temperatures of 273 K, 293 K, 571 K, 752 K and 903 K, obtained from the experimental data of Ref. [2] (See Table 5.1 and Fig. 5.4). QHA calculation and post-processing are performed with the Quantum espresso anharmonic code [84]

## 5.3 Results and discussion

### 5.3.1 Evolution of phonons with temperature

The phonon dispersions calculated at 298 K using QHA and TDPH agree fairly well with each other, as shown in Fig. 5.2. The small difference indicates that thermal expansion is the dominant effect over anharmonicity at that temperature (see Appendix B). This is expected, given that 298 K is lower than the Debye temperature of aluminum of 433K (i.e $\approx 0.6\theta_D$) and the atomic vibrations from equilibrium can be represented fairly well with harmonic potential. However, at 752K ($\approx 1.8\theta_D$), there is clear separation of QHA from the anharmonic shift. Essentially, QHA phonons are softer, and TDPH gives a better prediction that lies between the harmonic and QHA results. We note here that the TDPH result contains both quasiharmonic and anharmonic corrections:

$$\omega_{\mathtt{tdph}}(V,T) = \omega_{\mathtt{har}}(V) + \Delta\omega_{\mathtt{qha}}(V(T)) + \Delta\omega_{\mathtt{anh}}(V,T). \tag{5.1}$$

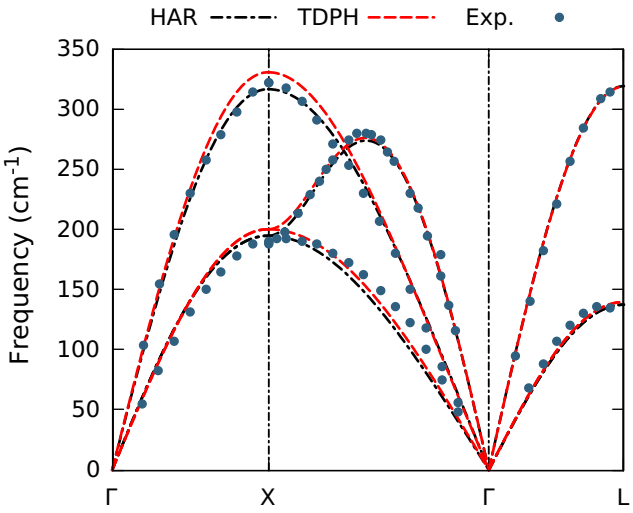


Figure 5.1: Phonon dispersion of Al computed using the TDPH method at 300K, plotted with measured values from inelastic neutron scattering experiment (steel blue circles) at 80 and 300 K [1].

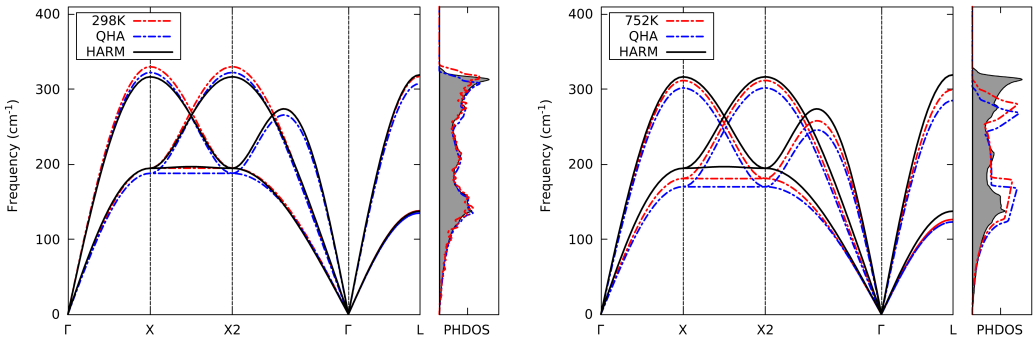


(a) (b)

Figure 5.2: Harmonic (HARM), quasiharmonic (QHA) and anharmonic (TDPH) phonon dispersion of Al at (a) 298 K (b) 775 K . The TDPH result is obtained by fitting the QHA force constants to finite temperature *ab initio* MD forces.

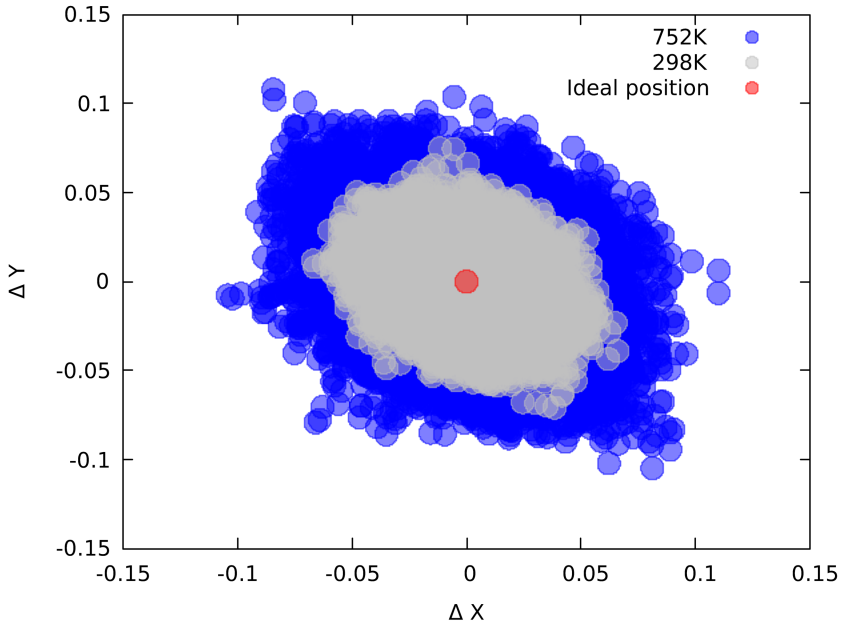


Figure 5.3: A two-dimensional projection of the trajectory of a typical atomic displacement in a $2 \times 2 \times 2$ supercell of fcc Al during AIMD at 298 K and 775 K.

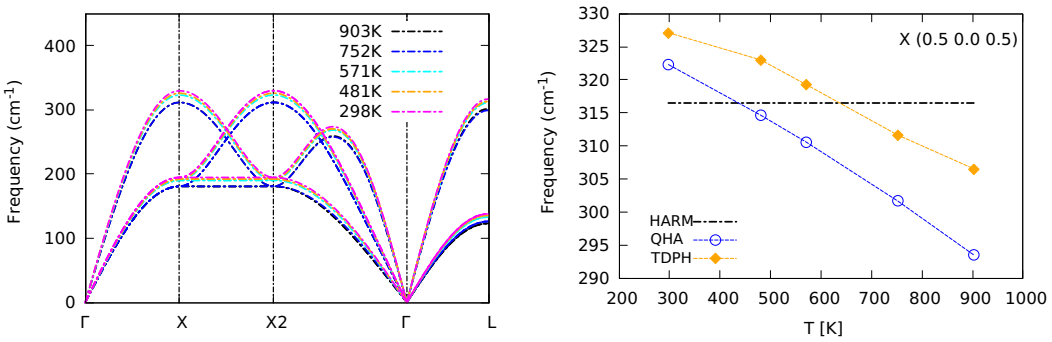


(a) (b)

Figure 5.4: The TDPH method gives the temperature dependence of phonons in Al, considering both anharmonic and quasiharmonic effects (using experimental lattice constants from Ref. [2] (a) phonon dispersion (b) Evolution of phonons at finite temperature, **X**(0.5, 0.0, 0.5).

### 5.3.2 Anharmonic correction to QHA free energy

We compute the effect of anharmonicity on the thermal expansion of Al by computing the free energy using quasiharmonic approximation (QHA) and temperature dependent phonon method (TDPH). The TDPH free energy is essentially the QHA free energy with renormalized phonons from TDPH (see Figure 5.5). The procedure involves TDPH calculation at each temperature to build effective force constants that depend explicitly on temperature, using QHA force constants as the initial guess. The free energy in QHA is given by

$$F(V,T) = E_0 + k_B T \sum_{\mathbf{q},s} \ln\left(2\sinh(\frac{\hbar\omega_{\mathbf{q},s}(V)}{2k_B T})\right), \tag{5.2}$$

where $E_0$ is the static DFT energy, $\omega_{\mathbf{q},s}$ is the harmonic frequency, $T$ is temperature and $k_B$ is the Boltzmann constant.

This approach has a difficulty because the volume-temperature equation of state used (VT-EOS) for the TDPH simulation may not be equal to the final one. This problem could be solved self-consistently, but we observe that a single-shot correction, starting from the standard QHA VT-EOS can produce a significant correction while remaining fully *ab initio*.

In Figure 5.7 at low temperature (100 K and 300 K), the lattice volume corresponding to the minima of the free energy changes slightly, an indication of weak anharmonicity. At 700 K, the TDPH correction to the QHA equilibrium volume is more significant, indicating the importance of including anharmonic effects at higher temperature. Following the flowchart of Figure 5.5, which involves minimizing the quasiharmonic free energy to find the volume at a given temperature but with TDPH force constant instead of QHA force constants, provides a systemic and efficient way of accounting for intrinsic anharmonicity non-self-consistently. We report in Figure **??** that using this procedure, we observe lattice volume that agrees closely with experimental measurements above 500 K, where anharmonic effects become prominent beyond the Debye temperature, and the TDPH results start to deviate from the QHA.

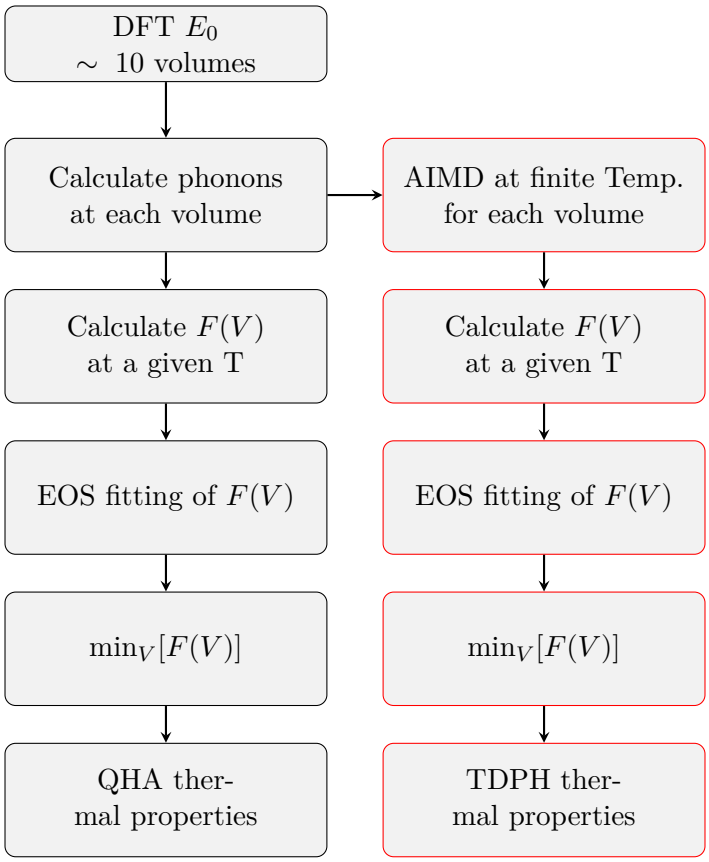


Figure 5.5: The free energy of crystals calculated using two different approaches. On the left, standard QHA approach is employed, while on the right, the TDPH method is used, which explicitly takes into account the temperature dependence of phonons at each QHA volume.

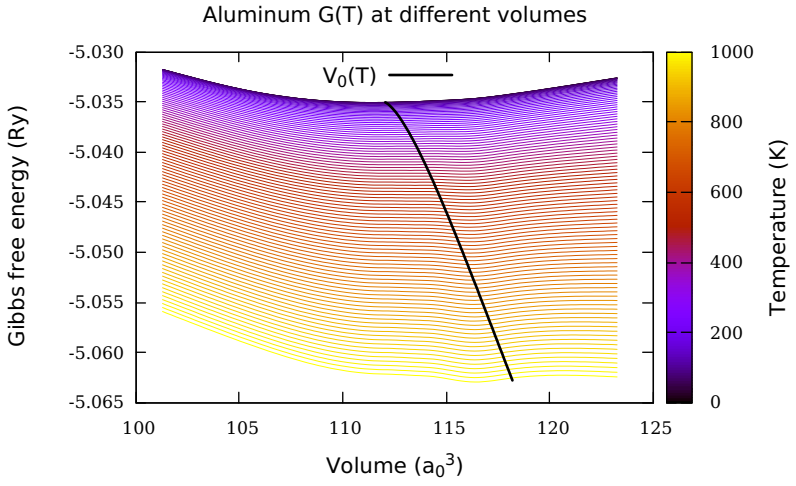


Figure 5.6: The Helmholtz free energy of Al from QHA with TDPH renormalized phonon spectra. The solid line joined the minima of each curve.

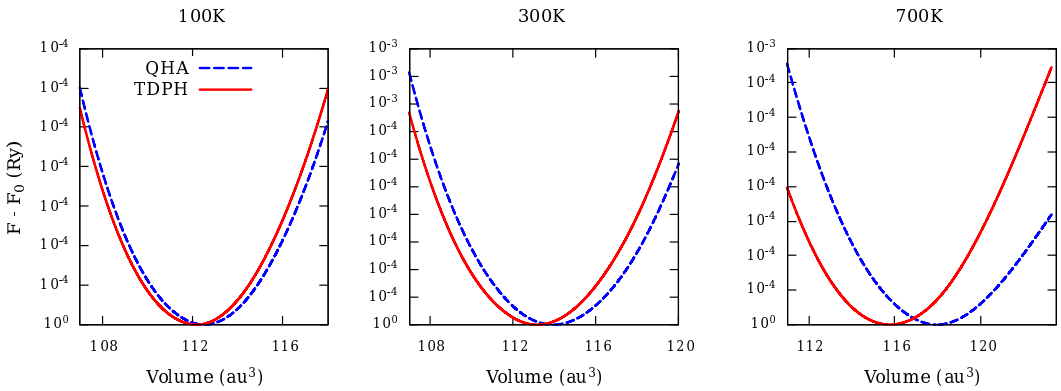


Figure 5.7: The free energy of Al per unit cell vs. lattice volume computed using quasiharmonic approximation (QHA) and temperature-dependent phonon method (TDPH).

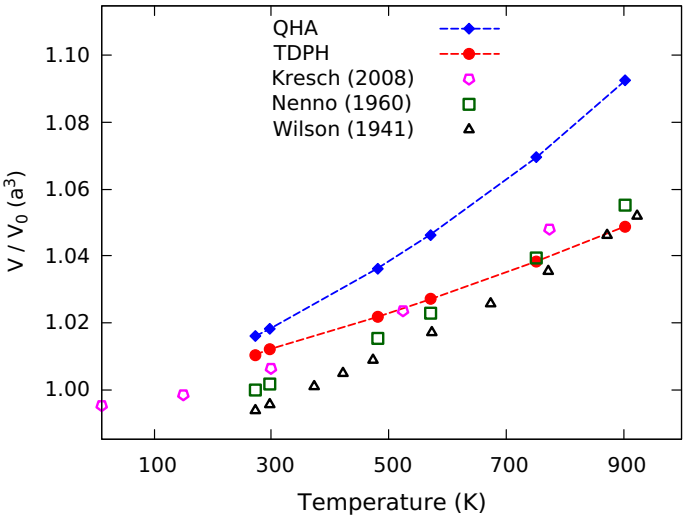


Figure 5.8: Latice volume vs. temperature in Al computed using quasiharmonic approximation (QHA) and temperature-dependent phonon method (TDPH). Open symbols are experimental measurements reported by Kresch *et al,* [3], Nenno *et al,* [2] and Wilson [4]

Table 5.1: Comparison of the temperature dependence of lattice constant in Al using QHA, TDPH and experimental results from Ref. [2]. $a_{TDPH}$ is obtained from the minimum of the QHA free energy with renormalized phonons from TDPH.

| T(K) | $a_{EXP}$ | $a_{QHA}$ | $a_{TDPH}$ |
|---|---|---|---|
| 298.15 | 4.04962 | 4.07282 | 4.06131 |
| 481.15 | 4.06801 | 4.09353 | 4.07637 |
| 571.15 | 4.07788 | 4.10484 | 4.08338 |
| 752.15 | 4.09991 | 4.12999 | 4.09839 |
| 903.15 | 4.12039 | 4.15388 | 4.11210 |

## 5.4 Conclusion

The vibrational and thermal properties of fcc Aluminum have been calculated from first principles using the TDPH method, beyond the typical QHA used in lattice dynamics. Applying TDPH to QHA FCs leads to a blue shift of the phonon spectra (Figure 5.2), a consequence of intrinsic anharmonicity. We also computed the effect of anharmonicity on the free energy of Al and found a considerable divergence from QHA at higher temperature (Figure 5.7).

# 6 – High-temperature BCC phase of Zirconium

## 6.1 Introduction

Ti, Zr, and Hf have hexagonal closed-packed (hcp) crystal structure at ambient conditions which transform to body-centered cubic (bcc) structure at 1155 K, 1136 K, and 2030 K, respectively [132]. *Ab initio* calculation of their phonon spectra in bcc structure shows dynamical instability within (quasi)harmonic approximation [132]. When compressed at room temperature, hcp Zr ($\alpha$-phase) transformed to hexagonal ($\omega$-phase) at 17 GPa and subsequently to bcc ($\beta$-phase) above 35 GPa. However, there is a temperature-induced $\alpha \rightarrow \beta$ phase transition around 1136 K at 0 GPa [133]. The high-temperature $\beta$-Zr is entropically stabilized and therefore strongly anharmonic. Here, we will test the validity of TDPH by examining the role of anharmonicity in stabilizing the experimentally observed high temperature bcc phase of Zr. Two methods of computing renormalized phonons will be employed, namely TDPH method of Section 4.1, and force-force autocorrelation method introduced by Moressi et al. [6]

## 6.2 Computational details

DFT calculations were performed with ultrasoft pseudopotentials [127] and generalized gradient approximation (GGA) with Perdew, Burke and Ernzerhof (PBE) exchange-correlation energy [128], implemented in Quantum espressopackage [116, 129]. The plane wave cutoff energy for Zr is 100 Ry and Monkhorst-Pack [130] k-points grid of $8 \times 8 \times 8$. A cold smearing [131] width of 0.05 Ry was used. Harmonic FCs were computed using DFPT [18] on a $2 \times 2 \times 2$ $\mathbf{q}$-grid. Both *Ab initio* MD and LD simulations were performed using NVT ensemble with supercell size commensurate with the phonon grid. Temperature is controlled with stochastic velocity rescaling method [70] in MD and a time step of 1 fs for both dynamics.

We tested the variation of phonons with larger with different values of Langevin damping ($0.5\gamma$, $2\gamma$, and $2\gamma$ ), and selected the optimal one.

For the calculation of FCs with <ff>[6] correlators, we used 6,000 configurations, neglecting the first 1000 snapshots as equilibration steps and binning the last snapshots into 5.

Post-processings are performed with homemade codes, scripts, and the Quantum espresso anharmonic code [84]

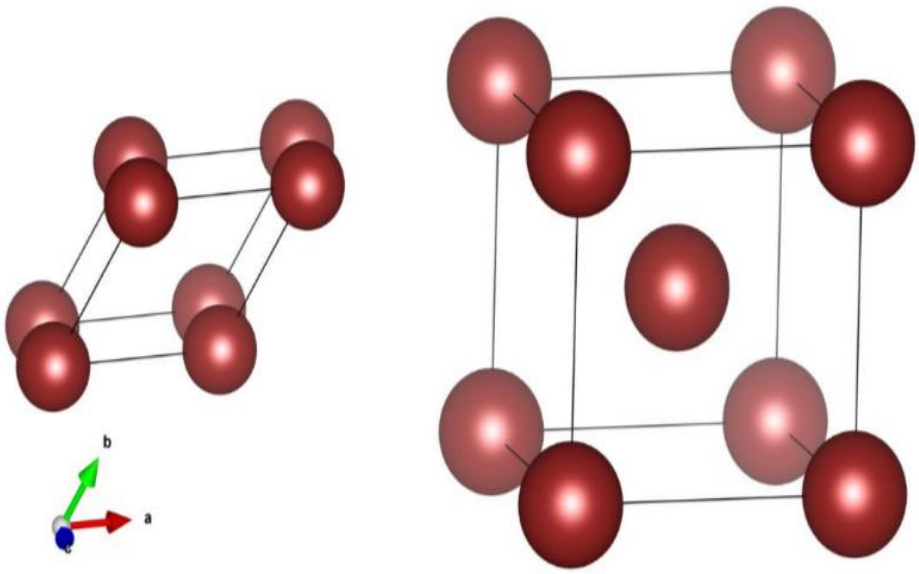


Figure 6.1: (*Left*)Primitive unit cell of Zr. (*Right* Conventional unit cell of Zr.)

## 6.3 Results and discussion

### 6.3.1 Temperature-dependent phonon spectra

Figure 6.2 shows the harmonic phonons in BBC Zr, indicating dynamical instability due to imaginary frequencies. As shown in Figure 6.4, we obtain stable phonons for the BCC phase of Zr at temperatures much below the experimentally measured transition temperature of 1136 K [132]. This results from the fact that TDPH phonons are always positive definite, regardless of the temperature. In this regard, TDPH is similar SCPH method [96]. Accurate prediction of transition temperature would require higher-order components in the BO surface expansion, omitted in the TDPH.

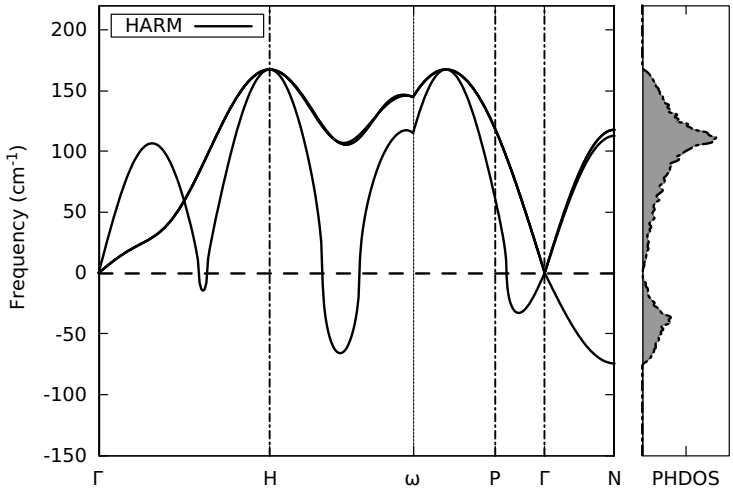


Figure 6.2: Harmonic phonon dispersion and density of states of bcc Zr, with soft modes at $\omega$- and $\Gamma$-points computed using DFPT at the GGA-PBE level.

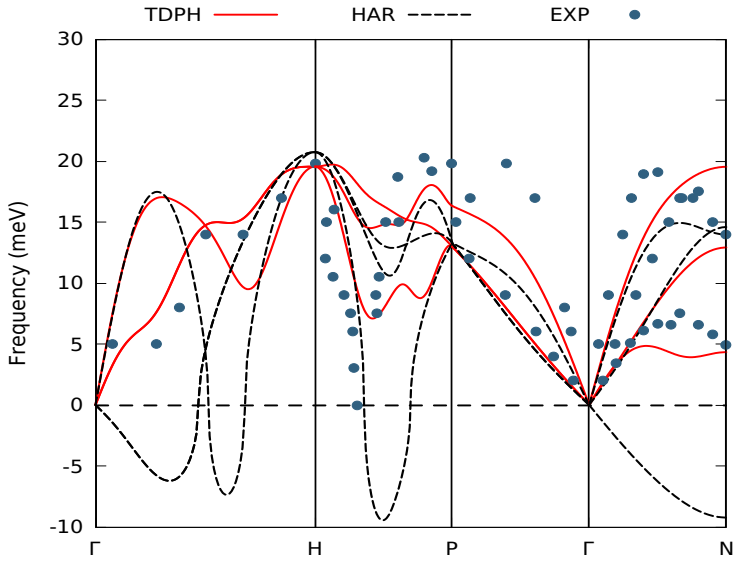


Figure 6.3: Comparison of the phonon dispersion of bcc Zr at 1200 K computed using TDPH (red solid line), harmonic approximation using DFPT (black dashed line), and experimental neutron scattering measurements (steel blue circles) [5].

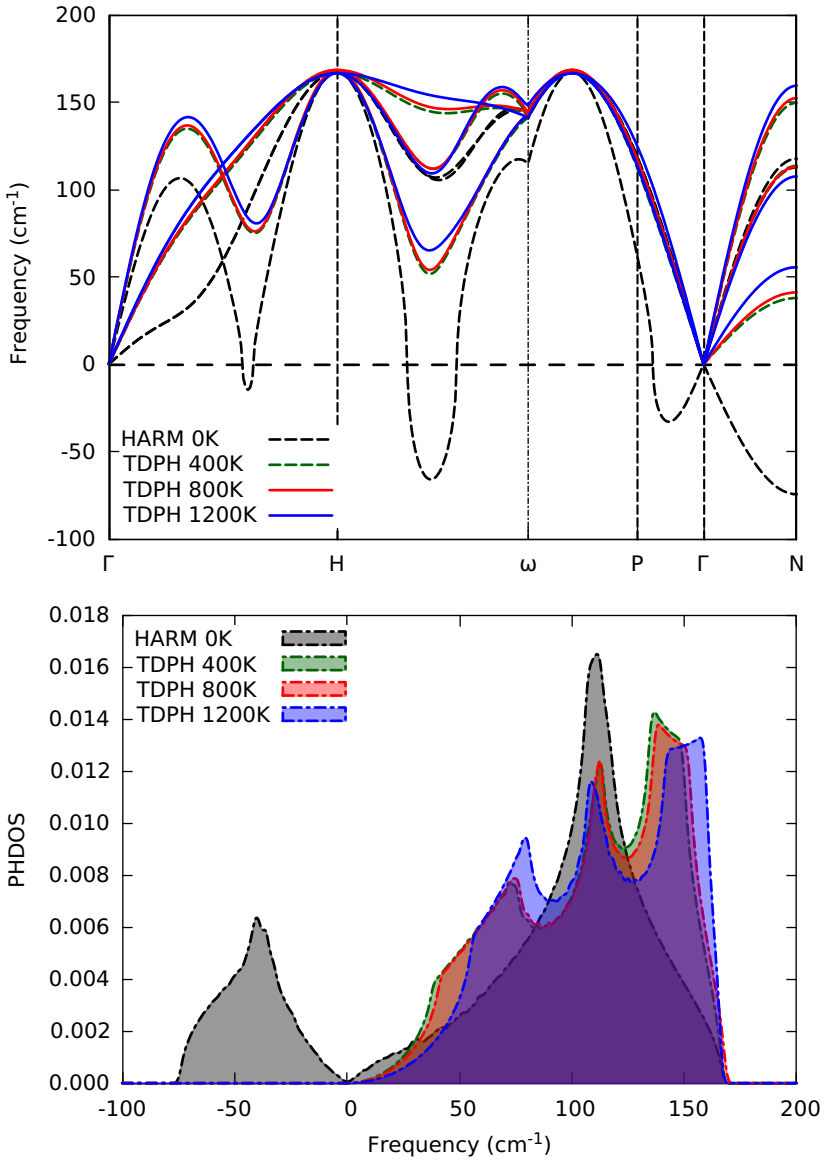


Figure 6.4: Comparison of TDPH phonon dispersion (top) and density of states (down) of BBC Zr at 400 K (dark-green), 800 K (red), 1200 K (blue), and 0K (black lines).

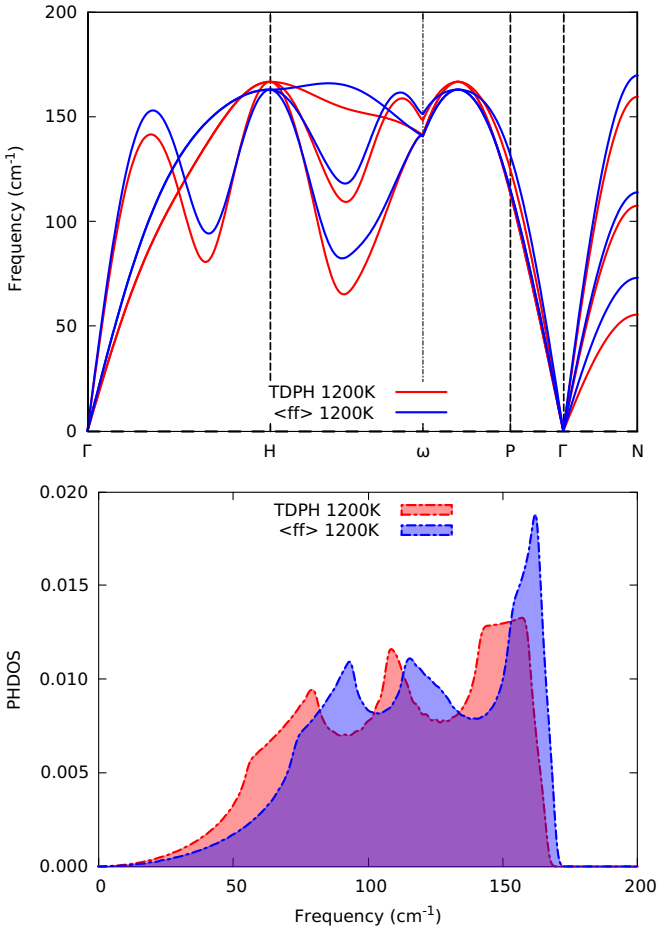


Figure 6.5: Comparison of temperature-dependent phonon dispersion and density of states, at 1200K from TDPH and force-force correlators method, $< \texttt{ff} >$, described in Ref. [6].

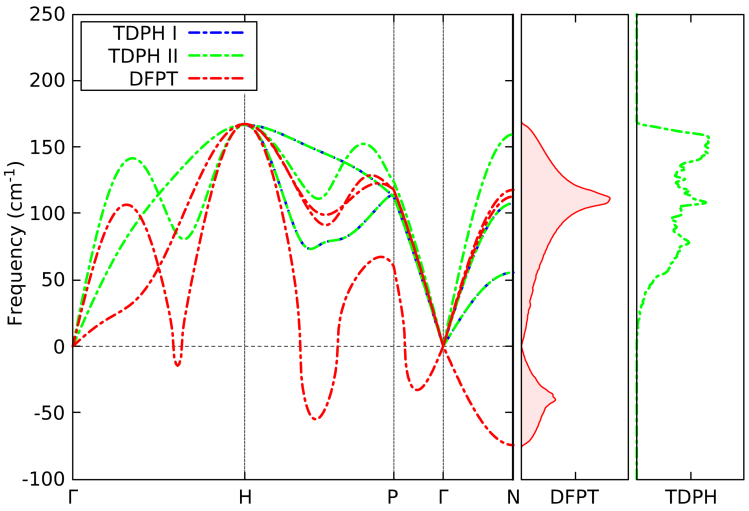


Figure 6.6: TDPH method applied to dynamically unstable bcc phase of Zr at 1200K, using initial force constants from DFPT (blue dash lines) and force-force correlators (green dashed lines) from Ref. [6]. Orange dashed lines represent harmonic phonons from DFPT.

Figure 6.6 shows how the TDPH works with two different initial guesses of the FCs: DFPT (blue-dashed lines) and the force-force correlator method of Ref. [6] (green-dashed lines) represented as `TDPH I` and `TDPH II`, respectively. A comparison of phonons using TDPH vs force-force correlators method for Al and $SrTiO_3$ is given in Appendix C. Irrespective of the initial guess of the FCs, the TDPH method always gives converged results, consistent with the temperature at which the PES is sampled.

## 6.4 Conclusion

We have shown that the BCC structure of Zr dynamically stabilizes at high temperatures through the temperature-dependent phonon method. At temperatures above absolute zero, the atoms in a real system do not occupy perfect lattice positions, which profoundly impacts the material's properties and contributes significantly to stabilizing high temperature phases. This also suggests that the dynamical stability of a lattice cannot be reliably determined using force constants at T = 0 K from DFT calculations for some systems. We have also demonstrated that the TDPH method can give converge phonons at finite temperature regardless of the initial guess of the force constants.

# 7 – Phonon Anharmonicity in $SrTiO_3$

Part of this Chapter appeared in the Journal article: Garba, I. B., Morresi, T., Bouillaguet, C., Casula, M., & Paulatto, L. *Journal of Physics: Condensed Matter (2023).*

## 7.1 Introduction

Transition metal oxides are materials with distinctive properties with a wide range of applications. Among them, $SrTiO_3$ has been the subject of intensive research as a prototypical $ABO_3$ oxide perovskite material with an interesting phase diagram and also as a host of the two-dimensional electron gas in $SrTiO_3/LaAlO_3$ interface [134], whose origin has not been fully resolved. Greater knowledge of the lattice dynamics of $SrTiO_3$ can offer valuable insight. At room temperature, $SrTiO_3$ has a cubic structure (space group: $Pm\bar{3}m$ No. 221), which transforms to low symmetry tetragonal phase (space group: $I4/mcm$ No. 140), below $T_c = 105$ K [135]. Most perovskite materials have structures that do not conform to the high symmetry cubic aristotype. They often form distorted low symmetric structures at low temperatures, which tranform to the ideal cubic phase upon heating (or compression). Displacement of atoms or groups of atoms in the perovskite structure dictates the type of distortion [136]. Polar displacement of an A or B cation, for example, is often related to zone center instabilty, which results in ferroelectricity, whereas tilting of the $BO_6$-octahedral tilt is typically related to zone-boundary instabilty, which results in transformation to tetragonal structure. *Ab initio* lattice dynamics can provide atomic insight into these transformations.

$SrTiO_3$ is used as a model for testing of new theoretical techniques [10, 137, 138, 12, 139, 13, 140]. First-principles method based on conventional harmonic and quasiharmonic approximation shows that $SrTiO_3$ is dynamically unstable, with soft modes at Γ, **R** and **M**-points (see Figure 7.4). The antiferrodistortive (AFD) **R**-mode is associated with symmetry lowering cubic-to-tetragonal structural phase transition, while the **Γ**-mode is ferroelectric (FE). The FE transition can be modulated by strain and substitutions doping [141].

Studies of the AFD mode began in the 60s with seminal work of Unoki and Sakudo [142] that relate the $TiO_6$ octahedral rotation to **R**-mode softening. Early reports on the dynamical properties of $SrTiO_3$ conducted in the 1990s provided rather conflicting reports on the dynamical instability in the BZ. Sai and Vanderbilt [143] applied the frozen phonon method using LDA, showing the AFD mode's hardening and the FE mode's softening with temperature. Wahl et al. [138] applied the same frozen-phonon method with GGA and HSE functional and showed imaginary frequencies at the Γ-point and real frequencies with LDA.

Subsequent results by LaSota et al. [144] using DFPT with linear augmented plane wave (LAPW) and LDA showed imaginary soft modes at the **M**-, **R**, and Γ-points in the BZ.

Evarestov et al. [145] demonstrated the functional dependency of the AFD mode adopting PBE, hybrid PBE0, and B3PW with various basis sets (PW and LCAO). These investigations, however, did not consider detailed microscopic descriptions of anharmonic effects on the FE and AFD modes beyond (quasi) harmonic approximation. Also, perturbative anharmonic method cannot be applied due to presence of imaginary modes in the BZ of the $SrTiO_3$.

Previous studies indicated that anharmonic effects renormalize phonons and predict the cubic-tetragonal $T_c$ [10], enhance accurate prediction of carrier mobility [114], thermal conductivity [140] and band-gap dependence on temperature [13].

Here, we applied the TDPH method to compute renormalized phonons and lattice thermal conductivity in $SrTiO_3$.

## 7.2 Computational Details

DFT calculations were performed using the QUANTUM ESPRESSO package [146, 117], employing optimized norm-conserving Vanderbilt pseudopotentials (NCPP) [128, 147] and ultrasoft pseudopotentials (USPP) [127]. Electronic exchange and correlation are approximated with PBEsol [148] in $SrTiO_3$. A cut-off energy of 100 Ry and 75 Ry were used for the NCPP and USPP, respectively, with a $4 \times 4 \times 4$ Monkhorst-Pack [130] k-point grid for Brillouin zone integration. For supercell calculations, k-point grids were down-scaled proportionally. Additional calculations of structural, electronic and phonon properties were performed using LDA [50], for comparison. The harmonic phonon spectra and FCs were computed using DFPT [18], including long-range contributions to the dynamical matrices for polar $SrTiO_3$. In all cases, phonon **q**-grid were commensurate with supercell size, and strict convergence was employed for phonon self-consistency ($10^{-16} Ry$).

The 2nd-order FCs computed on $2\times2\times2$ **q**-grid were interpolated on $4\times4\times4$ grid for the computation of lattice thermal conductivity. acoustic sum rule is applied for both 2nd-order and 3rd-order FCs. The phonon linewidth and lattice thermal conductivity were computed on a $20\times20\times20$ **q**-mesh using *Anharmonic* code of QUANTUM ESPRESSO [84, 149]. The lattice thermal conductivity of $SrTiO_3$ was computed using Boltzmann transport equation (BTE) within the Single-mode relaxation time (SMA) approximation along Cartesian direction $\alpha$ as

$$\kappa_l^{\alpha} = \frac{\hbar^2}{N_0 \Omega \kappa_B T^2} \sum_{\gamma} \nu_{\alpha,\gamma}^2 \omega_{\gamma}^2 n(n+1)\tau_{\gamma} \tag{7.1}$$

where $\hbar, N_0, \Omega, \kappa_B, T, n$ represent Planck constant, total number of **q**-mesh points, unit cell volume, Boltzmann constant, temperature, and Bose-Einstein phonon population. The phonon energy $\omega_{\gamma}$, and group velocity $\nu_{\alpha,\gamma}$ are computed from renormalized 2nd-order FCs using TDPH method.

We perform BOMD as implemented in QUANTUM ESPRESSO [146, 117] using the same calculation parameters as above. We used a $2 \times 2 \times 2$ supercell containing 40 atoms, commensurate with the phonon **q**-grid, while k-point grids were down-scaled proportionally. Temperature is controlled by stochastic velocity rescaling (svr) method [70] to ensure efficient canonical sampling using 1 fs time step. The length of the simulation and number of

MD snapshots were tested and optimal values were used. After equilibration, 500 snapshots sampled over 20,000 steps (equivalent to 20 ps) were sufficient to obtain converged results.

## 7.3 Results and Discussion

### 7.3.1 Structural and electronic properties

$SrTiO_3$ in cubic structure is a represntative of the $ABO_3$ perovskite structure swith space group $Pm\bar{3}m$ symmetry, No. 221. In this structure, Sr cation occupy Wyckoff site 1a(1/2, 1/2, 1/2), Ti cation at 1b(0, 0, 0), and the O anion at 3d(1/2, 0, 0). The optimized PBEsol lattice parameter is 3.899 Å, which is 1.6% smaller than the experimental value of 3.905 [13] at room temperature. As can be seen in Table 7.1, additional LDA and more accurate HSE results are also provided for comparison. Dynamical properties of perovskite are extremely sensitive to structural parameters, which in turn depends choice of the functional. As expected, our LDA and GGA results underestimate the band gap compared to HSE report from Verdi et al. [12]. The FE and AFD instability are present in LDA, PBE and HSE calculations as and do not differ significantly. Thus, using cheaper functional like PBEsol instead of more expensive HSE will be sufficient for accurate estimate of dynamical properties properties.

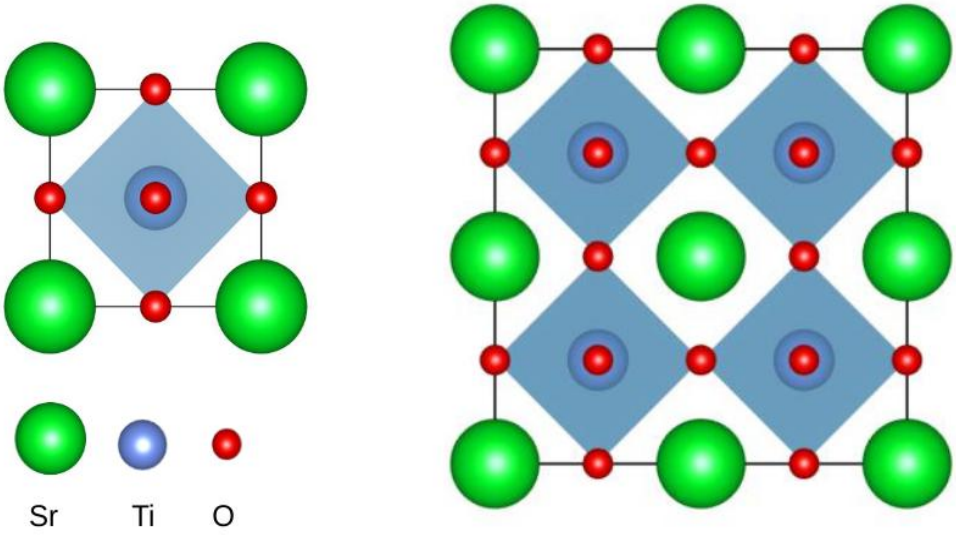


Figure 7.1: (*Left*) Illustration of a typical $ABO_3$ perovskite with $SrTiO_3$ as an exmaple. (*Right*) Supercell (2x2x2) with corner connected BO6 octahedra.

Table 7.1: Lattice parameter, band gap, FE and AFD frequencies in the cubic phase of $SrTiO_3$. For comparison, results from previous calculations [11, 12] and experiments [7, 13] are provided

| | LDA | PBEsol | HSE | Exp. |
|---|---|---|---|---|
| a (Å) | 3.891 | 3.889 | 3.8931 [12] | 3.905 [13] |
| $E_g$ $(eV)$ | 1.827 | 1.829 | 3.01 [11] | 3.160 [13] |
| $\omega_{\mathtt{FE}}$ $(cm^{-1})$ | 147i | 145i | 127i | 91 [7] |
| $\omega_{\mathtt{AFD}}$ $(cm^{-1})$ | 90i | 97i | 68i | 52 [7] |

### 7.3.2 Potential energy surface

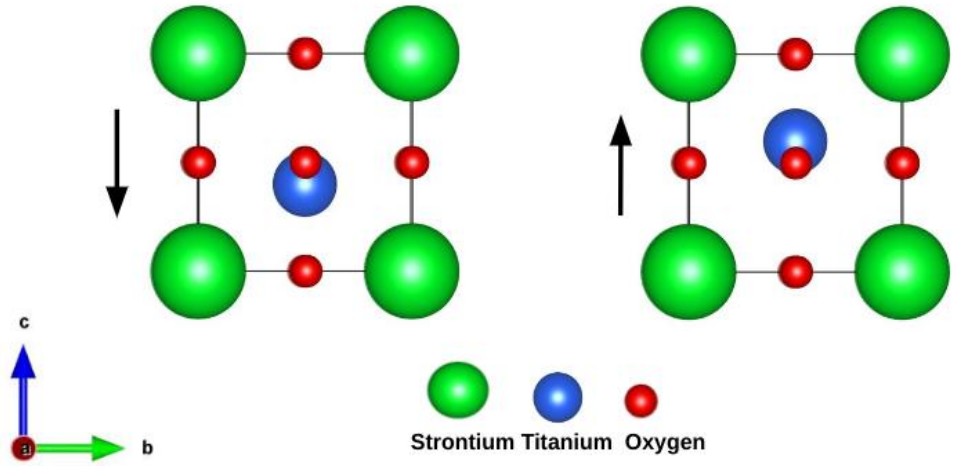


Figure 7.2: Off-centering displacement of Ti atom in the cubic phase of $SrTiO_3$.

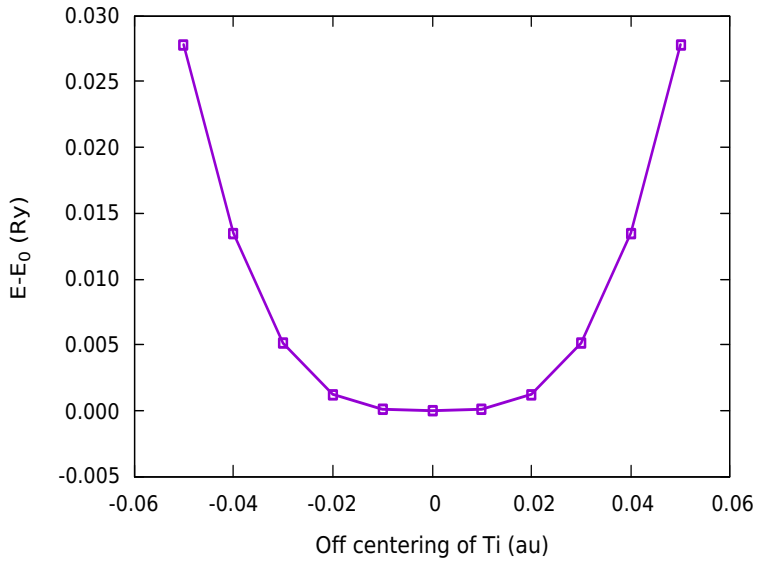


Figure 7.3: Potential energy surface along the off-centering displacement of Ti atom in the cubic phase of $SrTiO_3$.

### 7.3.3 Dynamical stability of high temperature cubic phase

In Figure 7.5, we show the dynamic stabilization of the cubic phase, as indicated by renormalized positive frequencies relative to imaginary modes obtained from harmonic approximation using DFPT. The temperature-dependence of the phonon dispersion and density of states (DOS) in cubic $SrTiO_3$ is shown in Figure 7.6, indicating phonon hardening with increasing temperature from 200 K to 800 K. This effect has also been observed in previous experimental and theoretical studies [139].

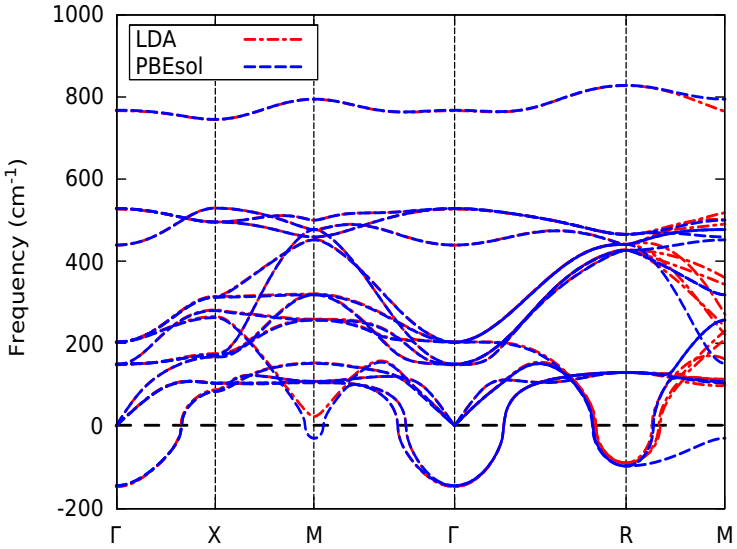


Figure 7.4: Phonon dispersion of cubic phase of $SrTiO_3$ from harmonic approximation using DFPT. Unstable imaginary modes at Γ-point indicate ferroelectric instability, and **R**-point correspond to antiferrodistortive mode. Imaginary modes present using PBEsol at **M**-point disappear in the case LDA, highlighting the significance of the choice of DFT functional.

### 7.3.4 Cubic to tetragonal phase transition

The temperature dependence of the squared frequency of the **R**-mode mode has been used to predict the cubic-to-tetragonal phase transition in $SrTiO_3$ by extrapolating the temperature of the **R**-mode. Figure 7.7 compares TDPH results to experimental measurements and other theoretical methods. Our transition temperature of 75 K (Figure 7.7) is closer to the experimental value of 105 K than SCPH (220 K) [10] and QSCAILD (200 K) [31] methods. A recent attempt to circumvent the functional dependence of the FE and AFD instabilities in $SrTiO_3$ employed the SSCHA method and machine learning force field trained on random-phase approximation (RPA), obtaining a transition temperature of 172 K via Curie-Weiss fit of the AFD mode [12]. The difference could be due to the functional used, as the lattice dynamical properties of ferroelectric materials are particularly sensitive to the DFT functionals. In the specific case of $SrTiO_3$, we prefer to use PBEsol because it is known to be reliable for predicting crystal geometry and dynamics, at reasonable computational cost [55]. But In general, a functional which is better at predicting some properties (e.g. electronic band gap) may be less accurate for others (e.g. lattice parameters). Also, for

some advanced functionals (metaGGA, hybrid), ab-initio forces can be difficult to converge or very expensive. A detailed discussion on functional dependence of soft modes in $SrTiO_3$ is provided in Ref. [12] and [138]

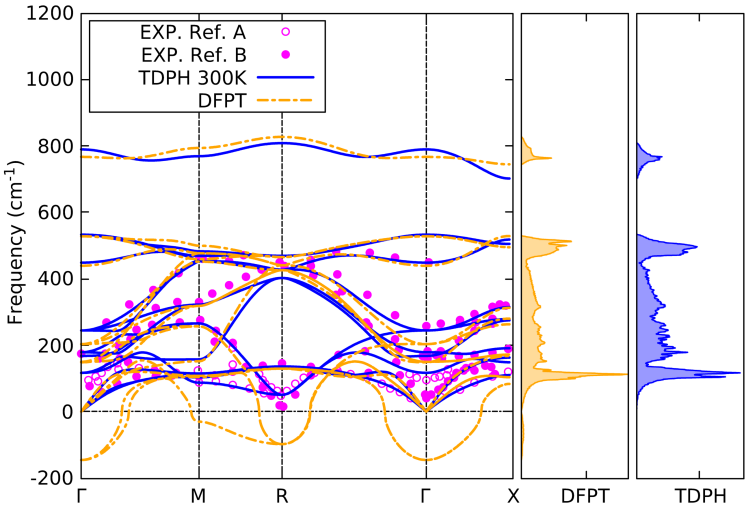


Figure 7.5: Phonon dispersion and DOS of cubic phase of $SrTiO_3$. The dotted orange lines show the results based on the DFPT, and the solid lines represent the finite-temperature phonons obtained with the TDPH scheme at 300 K, consistent with experimental INS results of Ref. A [7] and Ref. B [8].

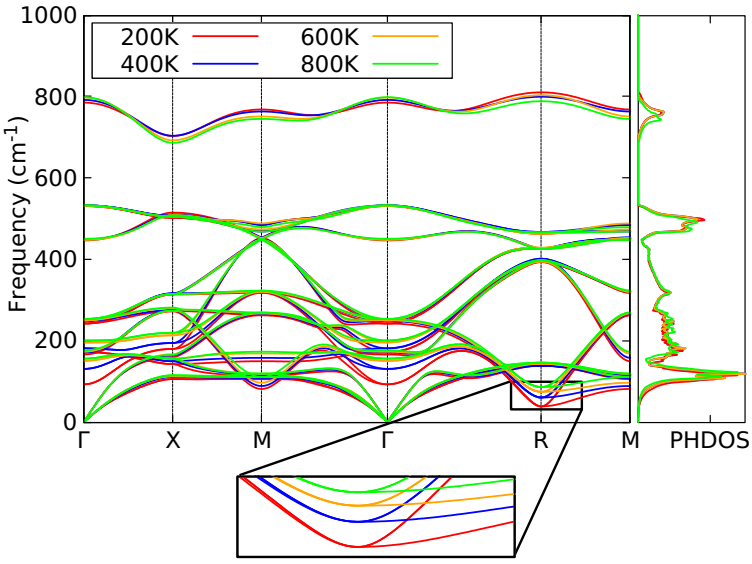


Figure 7.6: Temperature-dependence of phonon dispersion and DOS of cubic $SrTiO_3$ using TDPH method and a zoomed-in region around **R**-point.

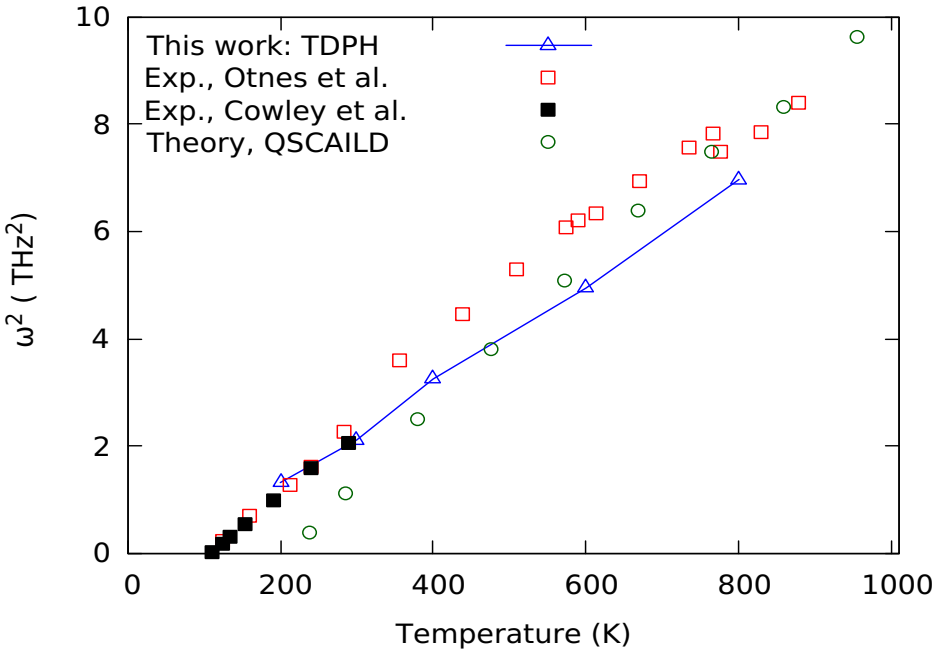


Figure 7.7: Temperature-dependence of the squared frequency of the soft **R**-mode, compared with experimental and QSCAILD results.

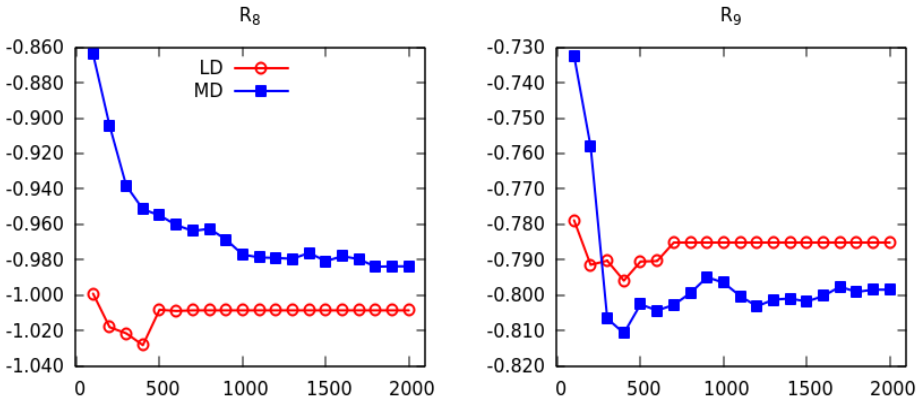


Figure 7.8: Convergence of selected phonon parameters for the AFD **R**-mode in $SrTiO_3$, (i.e. at $\mathbf{q_R} = (0.5\ 0.5\ 0.5)$). There are nine phonon parameters but only two ($\mathbf{R}_8$ and $\mathbf{R}_9$) differ significantly with respect to their initial values.

### 7.3.5 Lattice thermal conductivity

Temperature normalization of phonons can play a significant role in ab initio prediction of thermal transport, particularly in strongly anharmonic materials but also in materials that are often regarded as weakly anharmonic, like Al [43] and Si [150]. The force con-

stants (second- and third-order) are often obtained by zero-temperature DFT calculations in supercells [151] or via linear response and the 2n+1 theorem [18, 85, 84]. The effect of temperature is accounted for through the Bose-Einstein distributions of the phonons inherent in the phonon-phonon scattering rates and the mode-specific heat. Explicit temperature dependence of phonons and force constants is not considered. The temperature dependence of phonons and force constants can now be explicitly determined by more advanced anharmonic phonon techniques. These phonon renormalization approaches allow for the use of Boltzmann transport equation (BTE) to be extended to materials that would not normally be accessible by DFT, such as cubic $SrTiO_3$.

We compute the lattice thermal conductivity of $SrTiO_3$ based on the Boltzmann transport equation (BTE) of phonons in the single mode approximation (SMA) using renormalized 2nd-order FCs from TDPH, and compared to results from SCP theory [10] and experiment [9]. The effect of four-phonon scattering, which has been recently reported to suppress thermal conductivity in $SrTiO_3$ by $15-20\%$ beyond 200 K [152], is not taken into account in our theoretical prediction. Nevertheless, using TDPH-based finite temperature FCs provides a reasonable estimate of thermal conductivity in $SrTiO_3$, which is impossible with harmonic FCs, as shown in Fig. 7.12.

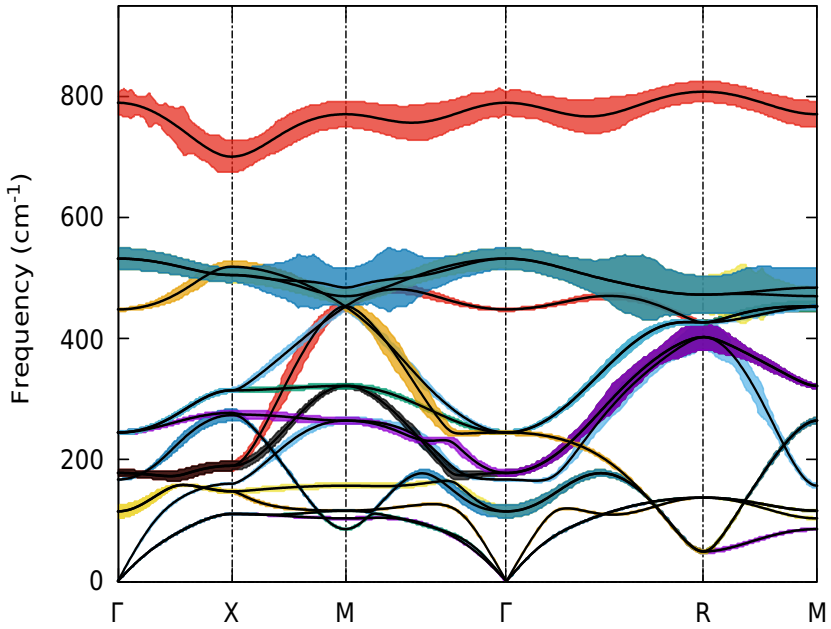


Figure 7.9: Calculated phonon dispersion of $SrTiO_3$. Each of the 15 branches has a width proportional to the anharmonic broadening at 300 K, magnified by a factor of 3 for clarity.

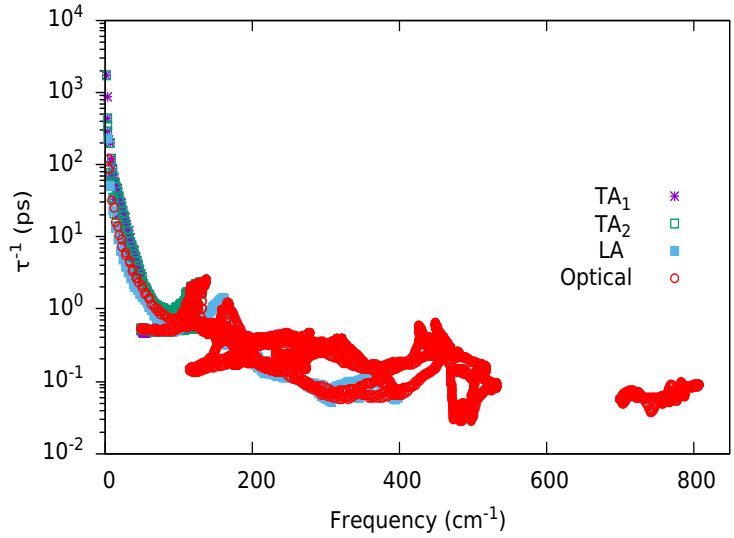


Figure 7.10: Phonon lifetime for the acoustic and optical modes.

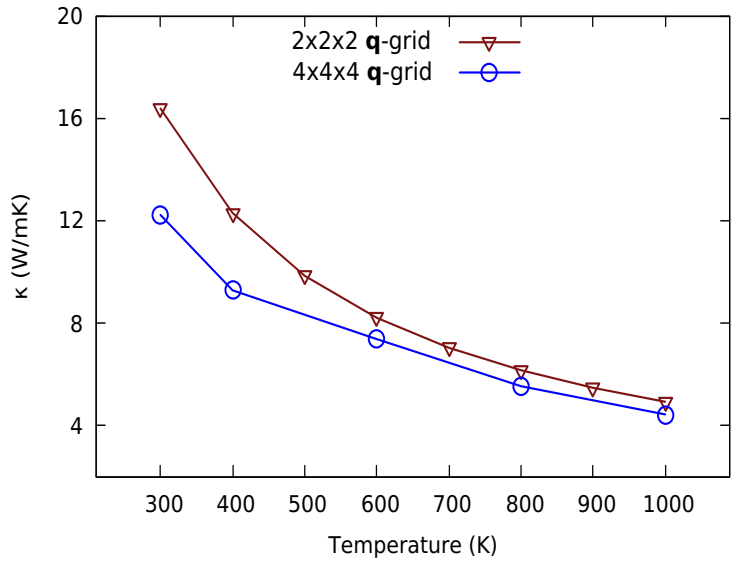


Figure 7.11: Convergence of Lattice thermal conductivity with **q**-grid .

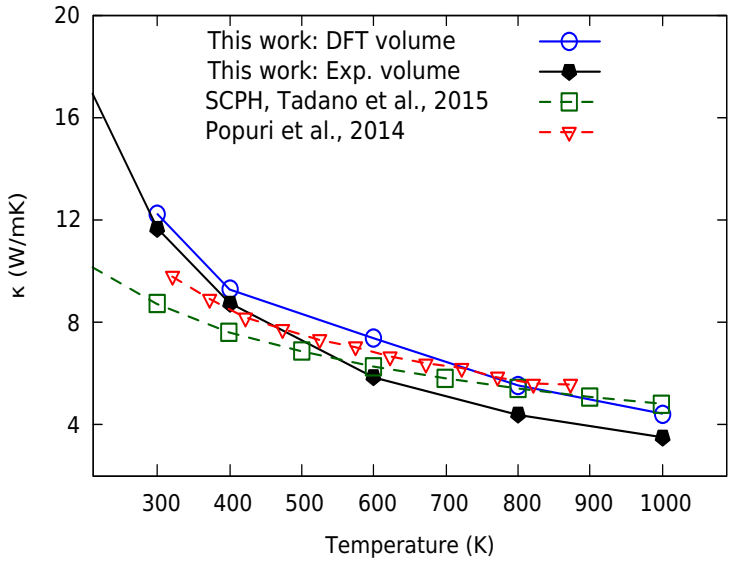


Figure 7.12: Lattice thermal conductivity of cubic $SrTiO_3$ computed from BTE using temperature-dependent 2nd-order FCs and 3rd-order from perturbation theory and $(2n+1)$ theorem (See text for details). Red triangles are experimental data from Popuri et al., [9] and dark-green rectangles are from SCP theory[10]. Blue circles indicate results at equilibrium DFT volume while black pentagon is at experimental volume.

## 7.4 Conclusion

We have performed TDPH calculations to investigate the anharmonic lattice dynamics and provides microscopic insight into the thermal transport and phase transition in $SrTiO_3$. Anharmonic phonon renormalization stabilized the cubic phase at finite temperature, reproducing the experimental phonon dispersion [7], [8]. The softening of the squared $R$-mode (the antiferrodistortive mode) with temperature from 200 K to 800 K agrees qualitatively with experimental results of Cowley *et al.* [110] and Otnes *et al.* [135] and previous theoretical calculation of Ref. [31]. Our predicted transition temperature using the Curie-Weiss fit is 75 K, compared to the experimental value of 105 K. We also determined phonon lifetimes and linewidths from the three-phonon scattering process by building perturbation on top of the TDPH potential, enabling computing the lattice thermal conductivity of $SrTiO_3$ using the Boltzmann transport equation (BTE) within the single-mode relaxation approximation, in good agreement with experiment. We highlight that utilizing finer $\mathbf{q}$-grid for the 2nd-order and 3rd-order FCs can increase agreement with experiment (see Figure 7.11), albeit such calculations beyond $4\times4$ grid were not done due to computational constraints. Overall, our findings underscore the significance of anharmonic phonon renormalization in predicting lattice dynamical and phonon transport properties in $SrTiO_3$.

# 8 – Conclusion and outlook

## 8.1 Conclusion

The aim of this thesis is to provide insight into the lattice dynamics of nuclei in materials and how that affects other properties. We develop a non-perturbative anharmonic method beyond the standard quasiharmonic approximation using a hybrid technique that combines density functional perturbation theory and *ab initio* molecular dynamics simulations. The work presented here includes both method development and application to different class of materials, with a particular focus on the effect of intrinsic anharmonicity on the structural, vibrational, and thermal transport properties of materials.

In Chapter 4, we introduce a reciprocal-space alternative to the temperature-dependent effective potential method (TDEP). Our methodology allows efficient computation of anharmonic effects induced by temperature while retaining the phonon quasiparticle description of phonons. The simplified temperature-dependent phonon (TDPH) method is a significant step forward over previous work. The TDEP method was used in its original formulation to extract an effective force constants matrix that best represents the *ab initio* molecular dynamics atomic forces via fitting [32, 33]. Here we use the symmetry of the crystal to reduce the reciprocal-space **q**-point sampling of phonons to its irreducible wedge and, then, for each **q**-point to reduce the dynamical matrix to its irreducible representations, expressed as a basis of symmetric hermitian dynamical matrices. The irreducible basis coefficients, which we call phonon parameters, are then fitted to *ab initio* forces. Our implementation has been tested on top of different dynamical sampling methods: uncontrolled NVE *ab initio* molecular dynamics, NVT with a stochastic SVR thermostat, and Langevin Dynamics. We have shown that all three methods can produce universally valid temperature-dependent force constants. NVE is more efficient, but with the strong caveat that it is susceptible to a large error from temperature drift. On the other hand, by using the energy auto-correlation time to determine a suitable sampling interval between AIMD steps, the two controlled dynamic methods, i.e., NVT and LD, are similar in efficiency, with the choice of the time step and thermostat parameters playing a crucial role in deciding if one can outperform the other. In our test case, LD yielded the smoothest convergence for the phonon parameters as a function of the number of dynamics steps used for fitting. We have shown that the TDPH method always converges to the same final phonon parameters irrespective of the initial choice of force constants, including randomization of phonon parameters, with negligible computing time.

We demonstrated this technique by computing anharmonic effects in the case of Aluminum, high-temperature BCC phase of Zr, and cubic $SrTiO_3$. These materials have anhar-

monicity that ranges from weak to strong, and therefore provide good test cases to validate the accuracy of the TDPH method, especially in the cases where QHA and perturbative anharmonic methods become invalid.

In Chapter 5, we applied the TDPH method to study anharmonic effects on phonon spectra in Al at fixed volume (corresponding to static DFT minimum) and at temperature dependent volume, extracted from QHA approximation and experiment. We observe an anharmonic correction on the vibrational free energy using TDPH force constants in QHA free energy minimization. In Chapter 6, using Zr as an example of BCC metal stabilized by temperature due to vibrational entropy, we demonstrated how temperature-dependent phonon free energy stabilizes the beta phase. Similar to the SCPH method, TDPH gives positive-definite phonons, regardless of the temperature.

Lastly, in Chapter 7, we study phonon anharmonicity in $SrTiO_3$, a prototypical $ABO_3$ perovskite, with an interesting phase diagram and various technological applications. TDPH method gives renormalized phonons in the cubic phase which match previous literature and experiemntal data. The temperature dependence of the soft antiferrodistortive mode is used to estimate the cubic to the tetragonal transition temperature, $T_c$, via Curie-Weiss fit, in close agreement with the experiment. We also determined phonon lifetimes and linewidths from the three-phonon scattering process using standard zero-temperature anharmonic force constants on top of the TDPH effective potential, enabling computation of the lattice thermal conductivity of cubic $SrTiO_3$ using the Boltzmann transport equation (BTE) within the single-mode relaxation approximation, in good agreement with experiment. Overall, our findings underscore the significance of anharmonic phonon renormalization in predicting lattice dynamical and phonon transport properties of materials.

## 8.2 Future direction

The main feature of the methodology developed in the thesis is that it is application agnostic, which makes it appealing to a wide range of problems in condensed matter and computational materials science, where temperature effects are non-negligible. Although the calculations reported are performed using density functional theory in the generalized gradient approximation, the method can be used in tandem with hybrid functional, higher-level electronic structure methods, path-integral molecular dynamics, or even Quantum Monte Carlo simulation, where an accurate description of electronic correlation and nuclear quantum effects is desirable, such as superconducting metallic hydrides or high-pressure hydrogen phases.

Extending the TDPH method to 3rd and 4th-order terms of the potential energy Taylor expansion will be significant in future work. While the current study gives effective harmonic potential with renormalization that shifts phonon frequency, effective 3rd-order force constants will account for linewidth broadening with explicit temperature dependence, which can result in an accurate prediction of thermal transport properties. [107, 153].

In our preliminary analysis, the TDPH method, when applied to long-range force constants by decomposing the Born effective charges on the symmetrized basis, shows a rather weak temperature dependence in the case of MgO. For this specific case, the temperature dependence of the effective charges could require a considerable change in the electronic structure. Future directions will include testing materials with large temperature-dependence on effective charges or a rigorous approach to perform a multipolar expansion [113] beyond

Gonze's scheme.

Most *ab initio* structure search algorithms [154, 155] are performed at zero temperature, neglecting structures at the saddle points of the Born Oppenheimer energy surface that may be stabilized by temperature. The minimal input required for TDPH makes it suitable for integration into these algorithms, especially in computational high-throughput screening.

# A – Appendix

## A.1 Phonons and autocorrelation in the different dynamic simulations

We compare the phonon dispersion in $SrTiO_3$ using three different methods of sampling the PES: LD, MD-NVT and MD-NVE. In each case, the 1,000 configurations are sampled using $\tau_{\texttt{sampling}} = C(t, t')$, where $C(t, t')$ is the autocorrelation function computed using Wiener–Khinchin theorem

$$C(t, t') = \int_{-\infty}^{\infty} |E|^2 e^{-2\pi i v t} dv, \tag{A.1}$$

where E is the instantaneous energy from *ab initio* simulation. Large deviation of the average temperature of MD-NVE from the target (T = 300 K) in Table A.1 is due to the absence of thermostat, and the small autocorrelation time comes from fast descend of NVE to minima (see text).

Table A.1: Autocorrelation time and average Temperature

| | LD | MD-NVT | MD-NVE |
|---|---|---|---|
| $T_{avr}$(K) | 299 | 298 | 315 |
| C(t,t') | 30 | 12 | 8 |

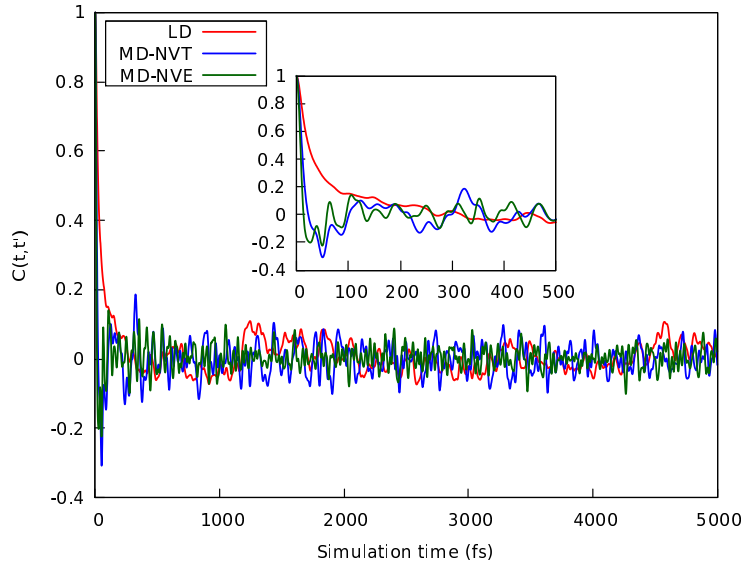


Figure A.1: Comparison of the autocorrelation function of the *ab initio* energy from the three different dynamic simulations in cubic $SrTiO_3$.

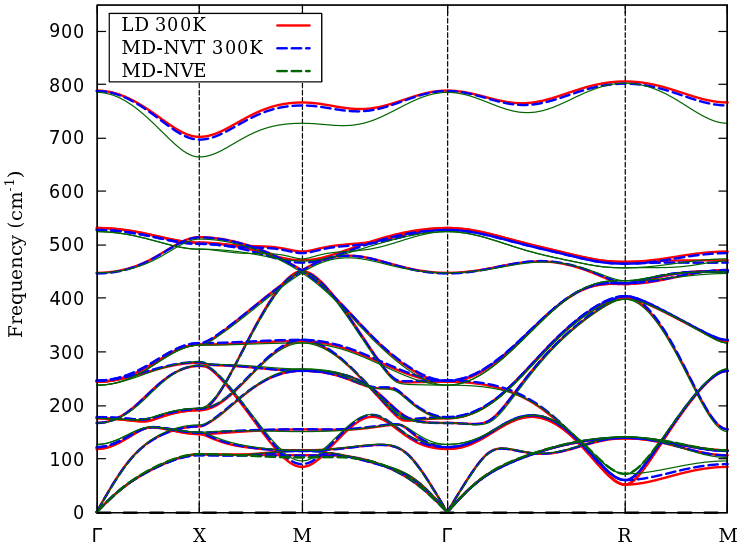


Figure A.2: Comparison of phonon dispersion from the three different dynamic simulations in cubic $SrTiO_3$.

## A.2 Phonons from LD: damping and time step

In the absence of damping ($\gamma = 0$), the Langevin dynamics described by Eq. 3.4 reduces to NVE, and in the absence of deterministic Born-Oppenheimer forces it reduces to Brownian motion. In the intermediate range its behavior depends on the ratio of $\gamma$ and the time step

($\Delta t$), with a large range of acceptable good values which can be determined by testing and computing the correlation time of $V$, on a case by case basis. Different time steps were used to compute the phonons $SrTiO3_3$ at finite temperatures. We rationalized the results in terms of temperature fluctuation from its target value and autocorrelation time of the energy. The phonon dispersions are displayed in A.3, using four different LD simulation time steps ($\Delta t$ = 1, 2.5 5, 10 fs). Among the four, $\Delta t$= 10 fs appears to stand out due to its ability to provide rapid exploration of phase space but at the expense of resolving the smallest (fastest) vibrational mode. Table A.2 also shows that $\Delta t$= 10 fs have the largest deviation to the target temperature, 300 K, when compared to the other 3. Figure A.4 illustrates the autocorrelation time of $V$ vs. the time step, with values of 2.5 and 5.0 fs being optimal from a computational standpoint. However, when comparing LD to other dynamic simulations or ensembles (e.g., MD-NVT or MD-NVE), all parameters are set to be the same, in which case $\Delta t$ = 1 fs is used.

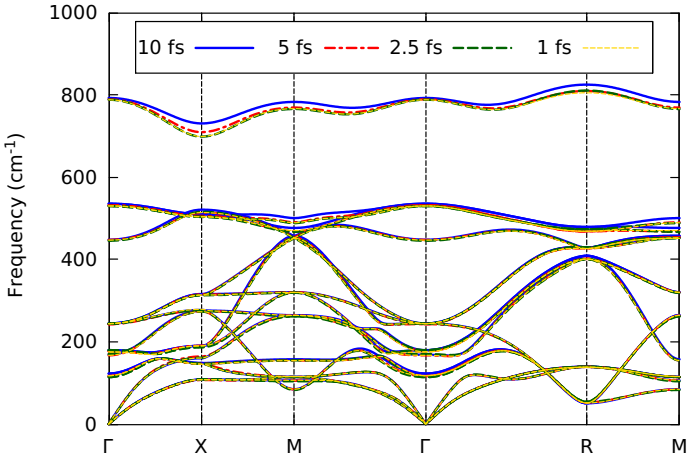


Figure A.3: Comparison of TDPH dispersion of $SrTiO3_3$ from LD with four different time steps: 10 fs (blue), 5 fs (red), 2.5 fs (dark-green), and 1 fs (golden).

Table A.2: Autocorrelation time and average Temperature using different LD time step

| $\Delta t$ (fs) | C(t',t) | $\chi^2$ | T (K) |
|---|---|---|---|
| 1.0 | 30 | 0.0068527681 | 299.00 |
| 2.5 | 16 | 0.0063913829 | 299.56 |
| 5.0 | 5 | 0.0064582700 | 299.03 |
| 10.0 | 3 | 0.0075531266 | 298.84 |

## A.3 Fitting with Energy vs Forces

In Section 4.2 we described the TDPH fitting steps using atomic forces where we defined the harmonic forces using harmonic force constants and atomic displacements as

$$\mathbf{F}^{H}_{i,\alpha} = -\sum_{j\beta} \phi^{\alpha\beta}_{ij} \mathbf{u}^{\beta}_{j} \tag{A.2}$$

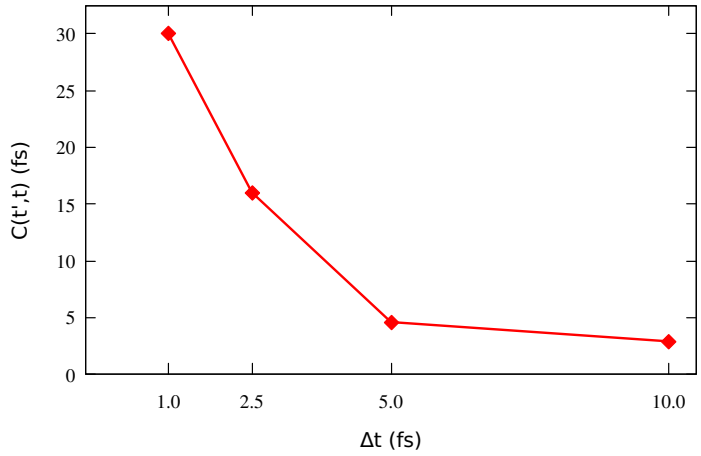


Figure A.4: Autocorrelation time (C(t',t)) vs time step ($\Delta t$) in LD simulation of $SrTiO_3$. $\Delta t = 2.5$ and 5.0 fs are computationally optimal.

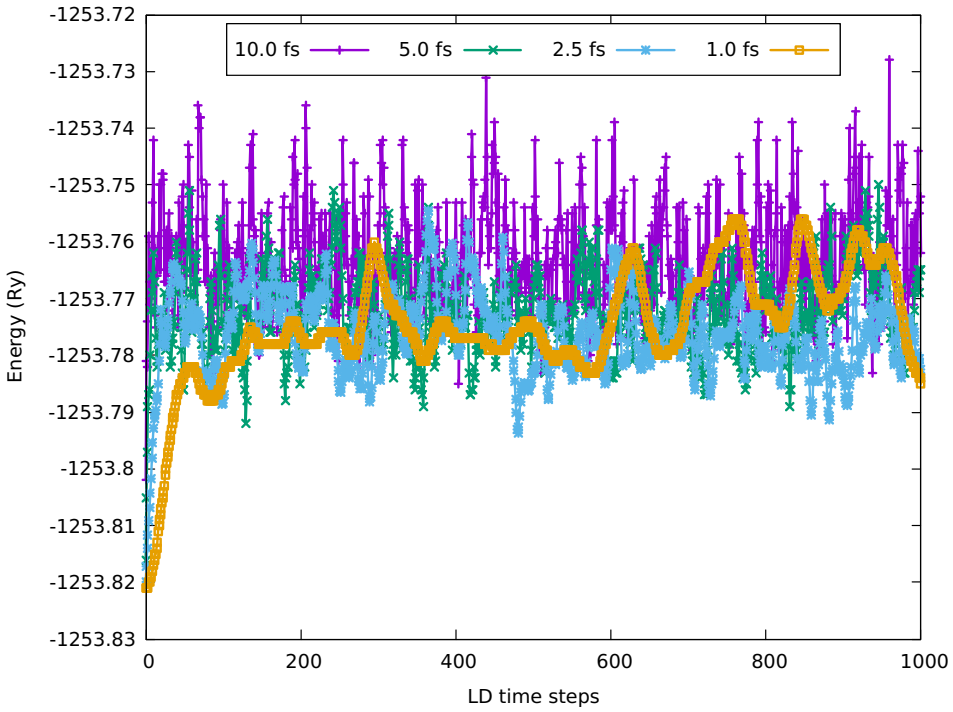


Figure A.5: *Ab initio* total energy from LD simulation with different time steps

We can define the harmonic energy, $E^H$, in similar fashion as

$$E^H = \sum_{ij,\alpha\beta} \phi_{ij}^{\alpha\beta} u_i^\alpha u_j^\beta. \tag{A.3}$$

It is important to keep in mind that whereas $\mathbf{F}^H$ can be specified for each degree of freedom, $E^H$ can only be obtained for a configuration. Therefore, it is more efficient to use $\mathbf{F}^H$ since it considerably reduces the number of calculations required to achieve convergence. We tested the TDPH method on FCC Al at 300K with these two methods and compared the results. In Figure A.7, the phonon dispersion and DOS are presented. The results for TDPH energy and forces extracted at 300 K are closer to each other than to harmonic approximation at 0 K using DFPT.

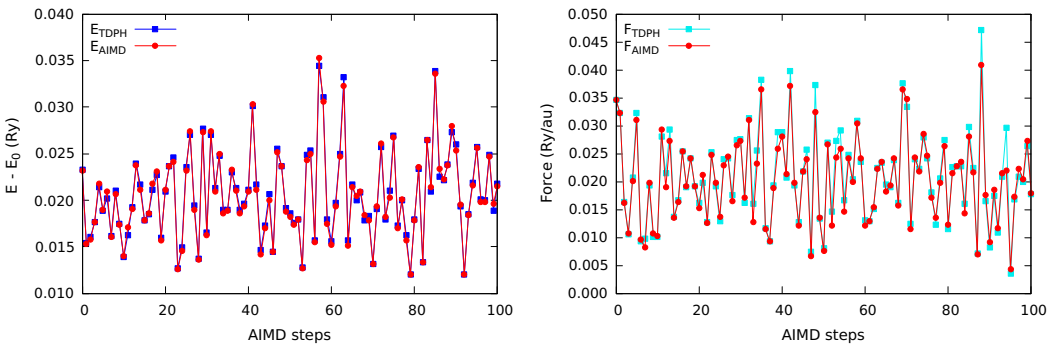


(a) (b)

Figure A.6: Comparison of TDPH and AIMD (a) energy (b) forces at 300 K.

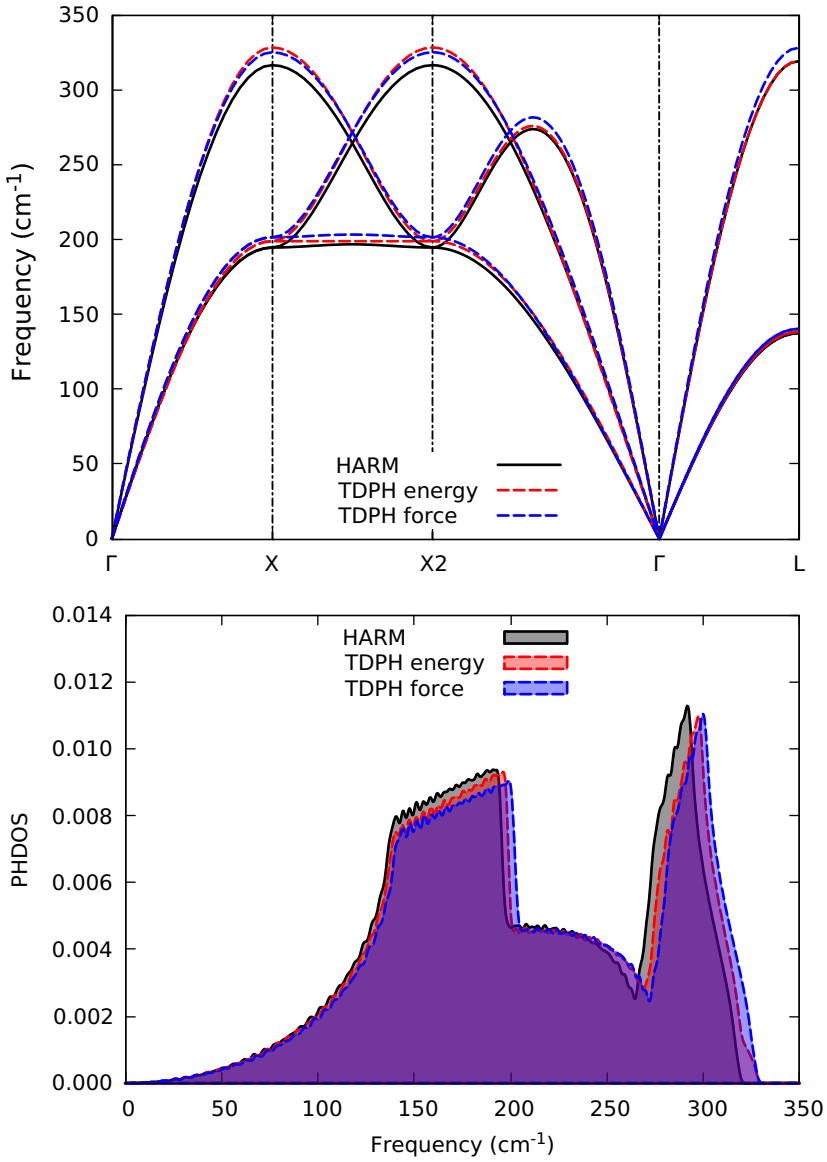


Figure A.7: Phonon dispersion (*top*) and DOS (*bottom*) computed using using TDPH energy (red) and forces (blue) at 300 K, compared with harmonic phonons using DFPT.

## A.4 TDPH input description

`TDPH` is part of the `D3Q+thermal2` anharmonic code of QUANTUM ESPRESSO. It reads a set of initial dynamical matrices for a given system and optimizes the harmonic force constants over a series of images that can be the output of a molecular dynamics calculation performed with QUANTUM ESPRESSO, or a Langevin Dynamics calculation from PIOUD code. The code will expect that the size of the supercell of the dynamics simulation is the same as that of the force constants. All pre-and post-processing, including re-centering force-constants, is

performed with the help of tools in `D3Q+thermal2`.

Table A.3: TDPH input description

| Input | Description |
|---|---|
| ai | CHARACTER, "md" or "pioud": "md" if the sampling comes from *ab initio* molecular dynamics using the standard QUANTUM ESPRESSO dynamics engine (i.e. using calculation='md' in the pw.x input) or "ld" for Langevin dynamics based on the Bussi and Parrinello's algorithm engine. |
| fmd | CHARACTER, "md.out": File from standard QUANTUM ESPRESSO dynamics engine. |
| ftau, fforce, ftoten | CHARACTER, default "positions.dat" "forces.dat", "sigma.dat": Output files from LD containing atomic positions in Angstrom, atomic forces in Hartree per Angstrom, and potential energy Hartree atomic units. |
| file_mat2 | CHARACTER, default "mat2R": File containing initial force constants. Must be periodic(i.e. generated with nf = 0 using d3_q2r.x). |
| nfirst, nskip, nmax | INTEGER, default 1, 100, 5000: When reading MD or LD trajectory files, read one every nskip steps starting from nfirst until nmax configurations are read (i.e. from nfirst to nfirst+nskip×(nmax−1)). |
| fit_type | CHARACTER, forces: The fitting method described in the text. |
| minimization | CHARACTER, ph, ph+zstar or global: These choices define the which TDPH minimization method to employ. ph will minimize short-range FCs and add long-range FCs if present (as they are). ph+zstar decompose both short and long-range FCs, minimize and subsequently recompose the TDPH FCs. global is experimental. |
| e0 | REAL: Equilibrium total energy from DFT before AIMD steps. |
| thr | REAL, DEFAULT=1.d-12: file from QUANTUM ESPRESSO containing initial atomic coordinates and |
| randomization | REAL: Adds or subtracts random numbers to initial phonon parameters. |

# B – Publications

The following is a compilation of journal articles, conference talks and posters that have been published, featuring portions of the thesis.

## B.1 Publications in peer reviewed journals

1. Garba, I. B., Morresi, T., Bouillaguet, C., Casula, M. & Paulatto, L., (2023). Reciprocal space temperature-dependent phonons method from ab-initio dynamics. Journal of Physics: Condensed Matter 35, 395402.

## B.2 International conferences (Talk)

1. Anharmonic phonons from minimal symmetrized basis. American Physical Society Annual Meeting (APS 2023 | Virtual) March 20 - 22, 2023.

2. Lattice dynamics of strongly anharmonic materials. Journées de la Matière Condensée, (JMC) Condensed Matter Physics Division of the French Physical Society (SFP) 2022, Lyon - France, August 22 - 26th, 2022.

3. Temperature-dependent phonons from ab initio molecular dynamics and density functional perturbation theory Poster at American Physical Society Annual Meeting (APS 2022), Chicago IL, 2022, March 14 - 19th, 2022.

## B.3 International conferences (Poster)

1. Reciprocal space approach to temperature-dependent phonons. 17th International Conference on Phonon Scattering in Condensed Matter, Phonons 2023, Paris - France, July 2 - 7th, 2023.

2. Young Researcher's Workshop on Machine Learning for Materials 2022, ICTP-SISSA Trieste, Italy, May 9 - 13th, 2022.

3. Paris International School on Advanced Computational Materials Science (PISACMS), 29th Aug - 5th Sep, 2021.

# Bibliography


[1] R. Stedman & G. Nilsson; "Dispersion Relations for Phonons in Aluminum at 80 and 300°K"; Phys. Rev. **145**, p. 492–500 (1966). vi, 46

[2] S. Nenno & K. JW; "Detection and determination of equilibrium vacancy concentrations in aluminum"; Journal of the Physical Society of Japan **15**, p. 220–226 (1960). vi, ix, 45, 48, 50

[3] M. Kresch, M. Lucas, O. Delaire, J. Lin & B. Fultz; "Phonons in aluminum at high temperatures studied by inelastic neutron scattering"; Physical Review B **77**, p. 024 301 (2008). vi, 45, 50

[4] A. Wilson; "The thermal expansion of aluminium from 0 to 650 C"; Proceedings of the Physical Society **53**, p. 235 (1941). vi, 50

[5] A. Heiming, W. Petry, J. Trampenau, M. Alba, C. Herzig, H. R. Schober & G. Vogl; "Phonon dispersion of the bcc phase of group-IV metals. II. bcc zirconium, a model case of dynamical precursors of martensitic transitions"; Phys. Rev. B **43**, p. 10 948–10 962 (1991). vi, 55

[6] T. Morresi, L. Paulatto, R. Vuilleumier & M. Casula; "Probing anharmonic phonons by quantum correlators: A path integral approach"; The Journal of Chemical Physics **154**, p. 224 108 (2021). vi, vii, 2, 13, 14, 20, 21, 22, 26, 35, 36, 53, 57, 58

[7] W. Stirling; "Neutron inelastic scattering study of the lattice dynamics of strontium titanate: harmonic models"; Journal of Physics C: Solid State Physics **5**, p. 2711 (1972). vii, ix, 61, 62, 64, 68

[8] R. Cowley, W. Buyers & G. Dolling; "Relationship of normal modes of vibration of strontium titanate and its antiferroelectric phase transition at 110 K"; Solid State Communications **7**, p. 181–184 (1969). vii, 64, 68

[9] S. R. Popuri, A. Scott, R. Downie, M. Hall, E. Suard, R. Decourt, M. Pollet & J.-W. Bos; "Glass-like thermal conductivity in SrTiO 3 thermoelectrics induced by A-site vacancies"; Rsc Advances **4**, p. 33 720–33 723 (2014). vii, 66, 68

[10] T. Tadano & S. Tsuneyuki; "Self-consistent phonon calculations of lattice dynamical properties in cubic $SrTiO_3$ with first-principles anharmonic force constants"; Phys. Rev. B **92**, p. 054 301 (2015). https://link.aps.org/doi/10.1103/PhysRevB.92.054301. vii, 2, 23, 41, 59, 60, 63, 66, 68

[11] C. Mitra, C. Lin, J. Robertson & A. A. Demkov; "Electronic structure of oxygen vacancies in $SrTiO_3$ and $LaAlO_3$"; Phys. Rev. B **86**, p. 155 105 (2012). https://link.aps.org/doi/10.1103/PhysRevB.86.155105. ix, 61, 62

[12] C. Verdi, L. Ranalli, C. Franchini & G. Kresse; "Quantum paraelectricity and structural phase transitions in strontium titanate beyond density functional theory"; Physical Review Materials **7**, p. L030 801 (2023). ix, 59, 61, 62, 63, 64

[13] Y.-N. Wu, W. A. Saidi, J. K. Wuenschell, T. Tadano, P. Ohodnicki, B. Chorpening & Y. Duan; "Anharmonicity explains temperature renormalization effects of the band gap in SrTiO3"; The Journal of Physical Chemistry Letters **11**, p. 2518–2523 (2020). ix, 59, 60, 61, 62

[14] P. Hohenberg & W. Kohn; "Inhomogeneous Electron Gas"; Phys. Rev. **136**, p. B864–B871 (1964). https://link.aps.org/doi/10.1103/PhysRev.136.B864. 1

[15] M. Born & K. Huang; *Dynamical Theory of Crystal Lattices* (Oxford University Press, Oxford) (1954). 1, 14, 30

[16] M. Dove; "Introduction to the theory of lattice dynamics"; École thématique de la Société Française de la Neutronique **12**, p. 123–159 (2011). 1, 14

[17] H. Wendel & R. M. Martin; "Charge density and structural properties of covalent semiconductors"; Physical Review Letters **40**, p. 950 (1978). 1

[18] S. Baroni, S. de Gironcoli, A. Dal Corso & P. Giannozzi; "Phonons and related crystal properties from density-functional perturbation theory"; Rev. Mod. Phys. **73**, p. 515–562 (2001). https://link.aps.org/doi/10.1103/RevModPhys.73.515. 1, 30, 45, 53, 60, 66

[19] P. Carrier, R. Wentzcovitch & J. Tsuchiya; "First-principles prediction of crystal structures at high temperatures using the quasiharmonic approximation"; Physical Review B **76**, p. 064 116 (2007). 2, 16, 17

[20] S. Baroni, P. Giannozzi & E. Isaev; "Density-functional perturbation theory for quasi-harmonic calculations"; Reviews in Mineralogy and Geochemistry **71**, p. 39–57 (2010). 2, 16, 17, 45

[21] M. Born & D. Hooton; "Statistische dynamik mehrfach periodischer systeme"; Zeitschrift für Physik **142**, p. 201–218 (1955). 2, 19

[22] D. Hooton; "The use of a model in anharmonic lattice dynamics"; Philosophical Magazine **3**, p. 49–54 (1958). 2, 19

[23] N. Boccara & G. Sarma; "Theorie microscopique des transitions s' accompagnant d'une modification de la structure cristalline"; Physics Physique Fizika **1**, p. 219 (1965). 2, 19

[24] T. R. Koehler; "Theory of the self-consistent harmonic approximation with application to solid neon"; Physical Review Letters **17**, p. 89 (1966). 2, 19

[25] A. J. McGaughey & J. M. Larkin; "Predicting phonon properties from equilibrium molecular dynamics simulations"; Annual review of heat transfer **17** (2014). 2, 20

[26] J. Turney, E. Landry, A. McGaughey & C. Amon; "Predicting phonon properties and thermal conductivity from anharmonic lattice dynamics calculations and molecular dynamics simulations"; Physical Review B **79**, p. 064 301 (2009). 2, 11, 20

[27] N. de Koker; "Thermal conductivity of MgO periclase from equilibrium first principles molecular dynamics"; Physical Review Letters **103**, p. 125 902 (2009). 2, 20, 21

[28] D.-B. Zhang, T. Sun & R. M. Wentzcovitch; "Phonon quasiparticles and anharmonic free energy in complex systems"; Physical review letters **112**, p. 058 501 (2014). 2, 20, 21, 41

[29] P. Souvatzis, O. Eriksson, M. Katsnelson & S. Rudin; "Entropy driven stabilization of energetically unstable crystal structures explained from first principles theory"; Physical review letters **100**, p. 095 901 (2008). 2, 20, 22

[30] A. van Roekeghem, J. Carrete & N. Mingo; "Anomalous thermal conductivity and suppression of negative thermal expansion in ScF 3"; Physical Review B **94**, p. 020 303 (2016). 2, 23

[31] A. van Roekeghem, J. Carrete & N. Mingo; "Quantum self-consistent ab-initio lattice dynamics"; Computer Physics Communications **263**, p. 107 945 (2021). 2, 23, 63, 68

[32] K. Esfarjani & H. T. Stokes; "Method to extract anharmonic force constants from first principles calculations"; Physical Review B **77**, p. 144 112 (2008). 2, 3, 20, 25, 69

[33] O. Hellman, I. Abrikosov & S. Simak; "Lattice dynamics of anharmonic solids from first principles"; Physical Review B **84**, p. 180 301 (2011). 2, 3, 20, 25, 69

[34] F. Yang, O. Hellman, M. Lucas, H. Smith, C. Saunders, Y. Xiao, P. Chow & B. Fultz; "Temperature dependence of phonons in Pd 3 Fe through the Curie temperature"; Physical Review B **98**, p. 024 301 (2018). 2, 26

[35] F. Zhou, W. Nielson, Y. Xia, V. Ozoliņš *et al.*; "Compressive sensing lattice dynamics. I. General formalism"; Physical Review B **100**, p. 184 308 (2019). 2, 20

[36] B. Monserrat, N. D. Drummond & R. J. Needs; "Anharmonic vibrational properties in periodic systems: energy, electron-phonon coupling, and stress"; Phys. Rev. B **87**, p. 144 302 (2013). 2

[37] M. Zacharias, G. Volonakis, F. Giustino & J. Even; "Anharmonic lattice dynamics via the special displacement method"; Phys. Rev. B **108**, p. 035 155 (2023). https://link.aps.org/doi/10.1103/PhysRevB.108.035155. 2

[38] I. Errea, M. Calandra & F. Mauri; "Anharmonic free energies and phonon dispersions from the stochastic self-consistent harmonic approximation: Application to platinum and palladium hydrides"; Physical Review B **89**, p. 064 302 (2014). 2, 20, 23, 26, 27

[39] G. Bussi & M. Parrinello; "Accurate sampling using Langevin dynamics"; Physical Review E **75**, p. 056 707 (2007). 2, 13, 14, 26, 35

[40] T. Morresi, R. Vuilleumier & M. Casula; "Hydrogen phase-IV characterization by full account of quantum anharmonicity"; Physical Review B **106**, p. 054 109 (2022). 2

[41] K. Esfarjani & Y. Liang; "Thermodynamics of anharmonic lattices from first principles"; dans "Nanoscale Energy Transport", 2053-2563; p. 7–1 to 7–35 (IOP Publishing) (2020); ISBN 978-0-7503-1738-2. https://dx.doi.org/10.1088/978-0-7503-1738-2ch7. 2, 19

[42] B. Wei, Q. Sun, C. Li & J. Hong; "Phonon anharmonicity: a pertinent review of recent progress and perspective"; Science China Physics, Mechanics & Astronomy **64**, p. 1–34 (2021). 2

[43] I. B. Garba, T. Morresi, C. Bouillaguet, M. Casula & L. Paulatto; "Reciprocal space temperature-dependent phonons method from ab-initio dynamics"; Journal of Physics: Condensed Matter **35**, p. 395 402 (2023). https://dx.doi.org/10.1088/1361-648X/acdbf9. 3, 65

[44] M. Born & R. Oppenheimer; "Zur Quantentheorie der Molekeln"; Annalen der Physik **389**, p. 457 – 484 (1927). 5

[45] L. H. Thomas; "The calculation of atomic fields"; Mathematical Proceedings of the Cambridge Philosophical Society **23**, p. 542–548 (1927). 6

[46] E. Fermi; "Un metodo statistico per la determinazione di alcune priorieta deH'atome"; Rend. Accad. Naz. Lincei **6**, p. 602–607 (1927). 6

[47] D. P. A. M.; "Note on exchange phenomena in the Thomas-Fermi atom"; Proc. Cambridge Phil. Roy. Soc. **26**, p. 376–385 (1930). 6

[48] R. M. Martin; *Electronic structure: basic theory and practical methods* (Cambridge university press) (2020). 7

[49] R. O. Jones & O. Gunnarsson; "The density functional formalism, its applications and prospects"; Reviews of Modern Physics **61**, p. 689 (1989). 9

[50] A. Zunger; "Self-interaction correction to density-functional approximations for many-electron systems"; Physical Review B **23**, p. 5048 (1981). 9, 60

[51] J. P. Perdew & Y. Wang; "Accurate and simple analytic representation of the electron-gas correlation energy"; Physical review B **45**, p. 13 244 (1992). 9

[52] J. P. Perdew, K. Burke & M. Ernzerhof; "Generalized gradient approximation made simple"; Physical review letters **77**, p. 3865 (1996). 9

[53] D. M. Ceperley & B. J. Alder; "Ground state of the electron gas by a stochastic method"; Physical review letters **45**, p. 566 (1980). 9

[54] J. P. Perdew, K. Burke & M. Ernzerhof; "Generalized gradient approximation made simple"; Physical review letters **77**, p. 3865 (1996). 9

[55] Z. Wu & R. E. Cohen; "More accurate generalized gradient approximation for solids"; Physical Review B **73**, p. 235 116 (2006). 9

[56] V. Anisimov & O. Gunnarsson; "Density-functional calculation of effective Coulomb interactions in metals"; Physical Review B **43**, p. 7570 (1991). 9

[57] V. I. Anisimov & A. Lichtenstein; "First-principles calculations of the electronic structure and spectra of strongly correlated systems: the LDA+ U method"; Journal of Physics: Condensed Matter **9**, p. 767 (1997). 9

[58] A. Georges & G. Kotliar; "Hubbard model in infinite dimensions"; Physical Review B **45**, p. 6479 (1992). 9

[59] A. Georges, G. Kotliar, W. Krauth & M. J. Rozenberg; "Dynamical mean-field theory of strongly correlated fermion systems and the limit of infinite dimensions"; Reviews of Modern Physics **68**, p. 13 (1996). 9

[60] M. Cococcioni & S. De Gironcoli; "Linear response approach to the calculation of the effective interaction parameters in the LDA+ U method"; Physical Review B **71**, p. 035 105 (2005). 9

[61] C. Humphreys; "Electron-energy-loss spectra and the structural stability of nickel oxide: An LSDA+ U study"; Physical Review B **57**, p. 1505 (1998). 9

[62] M. P. Allen & D. J. Tildesley; *Computer simulation of liquids* (Oxford university press) (2017). 11, 12, 13

[63] R. Kubo; "The fluctuation-dissipation theorem"; Reports on progress in physics **29**, p. 255 (1966). 11, 13

[64] F. Ercolessi & J. B. Adams; "Interatomic potentials from first-principles calculations: the force-matching method"; Europhysics Letters **26**, p. 583 (1994). 11

[65] R. Car & M. Parrinello; "Unified Approach for Molecular Dynamics and Density-Functional Theory"; Phys. Rev. Lett. **55**, p. 2471–2474 (1985). https://link.aps.org/doi/10.1103/PhysRevLett.55.2471. 11

[66] H. J. Berendsen, J. v. Postma, W. F. Van Gunsteren, A. DiNola & J. R. Haak; "Molecular dynamics with coupling to an external bath"; The Journal of chemical physics **81**, p. 3684–3690 (1984). 12

[67] H. C. Andersen; "Molecular dynamics simulations at constant pressure and/or temperature"; The Journal of chemical physics **72**, p. 2384–2393 (1980). 12

[68] S. Nosé; "A unified formulation of the constant temperature molecular dynamics methods"; The Journal of chemical physics **81**, p. 511–519 (1984). 12

[69] W. G. Hoover; "Canonical dynamics: Equilibrium phase-space distributions"; Physical review A **31**, p. 1695 (1985). 12

[70] G. Bussi, D. Donadio & M. Parrinello; "Canonical sampling through velocity rescaling"; The Journal of chemical physics **126**, p. 014 101 (2007). 12, 35, 41, 45, 53, 60

[71] J. Thijssen; *Computational physics* (Cambridge university press) (2007). 13

[72] H. Risken; "Fokker-planck equation"; dans "The Fokker-Planck Equation", p. 63–95 (Springer) (1996). 13

[73] F. Mouhat, S. Sorella, R. Vuilleumier, A. M. Saitta & M. Casula; "Fully quantum description of the Zundel ion: combining variational quantum Monte Carlo with path integral Langevin dynamics"; Journal of chemical theory and computation **13**, p. 2400–2417 (2017). 14, 31, 36

[74] P. DeCicco & F. Johnson; "The quantum theory of lattice dynamics. IV"; Proceedings of the Royal Society of London. A. Mathematical and Physical Sciences **310**, p. 111–119 (1969). 14

[75] R. M. Pick, M. H. Cohen & R. M. Martin; "Microscopic theory of force constants in the adiabatic approximation"; Physical Review B **1**, p. 910 (1970). 14

[76] D. C. Wallace & H. Callen; "Thermodynamics of crystals"; American Journal of Physics **40**, p. 1718–1719 (1972). 16

[77] S. Biernacki & M. Scheffler; "Negative thermal expansion of diamond and zinc-blende semiconductors"; Phys. Rev. Lett. **63**, p. 290–293 (1989). https://link.aps.org/doi/10.1103/PhysRevLett.63.290. 17

[78] A. Fleszar & X. Gonze; "First-principles thermodynamical properties of semiconductors"; Phys. Rev. Lett. **64**, p. 2961–2961 (1990). https://link.aps.org/doi/10.1103/PhysRevLett.64.2961. 17

[79] P. Pavone, K. Karch, O. Schütt, D. Strauch, W. Windl, P. Giannozzi & S. Baroni; "Ab initio lattice dynamics of diamond"; Phys. Rev. B **48**, p. 3156–3163 (1993). https://link.aps.org/doi/10.1103/PhysRevB.48.3156. 17

[80] L.-F. Huang, X.-Z. Lu, E. Tennessen & J. M. Rondinelli; "An efficient ab-initio quasiharmonic approach for the thermodynamics of solids"; Computational Materials Science **120**, p. 84–93 (2016). ISSN 0927-0256. https://www.sciencedirect.com/science/article/pii/S0927025616301719. 17

[81] P. Nath, D. Usanmaz, D. Hicks, C. Oses, M. Fornari, M. B. Nardelli, C. Toher & S. Curtarolo; "AFLOW-QHA3P: Robust and automated method to compute thermodynamic properties of solids"; Physical Review Materials **3**, p. 073 801 (2019). 17

[82] R. A. Cowley; "Anharmonic crystals"; Reports on Progress in Physics **31**, p. 123 (1968). 18

[83] A. Maradudin & A. Fein; "Scattering of neutrons by an anharmonic crystal"; Physical Review **128**, p. 2589 (1962). 18, 27

[84] L. Paulatto, F. Mauri & M. Lazzeri; "Anharmonic properties from a generalized third-order ab initio approach: Theory and applications to graphite and graphene"; Physical Review B **87**, p. 214 303 (2013). 18, 19, 31, 41, 45, 53, 60, 66

[85] X. Gonze & J.-P. Vigneron; "Density-functional approach to nonlinear-response coefficients of solids"; Physical Review B **39**, p. 13 120 (1989). 18, 66

[86] M. Lazzeri & S. de Gironcoli; "First-principles study of the thermal expansion of Be"; Phys. Rev. B **65**, p. 245 402 (2002). https://link.aps.org/doi/10.1103/PhysRevB.65.245402. 18

[87] W. Li, J. Carrete, N. A. Katcho & N. Mingo; "ShengBTE: A solver of the Boltzmann transport equation for phonons"; Computer Physics Communications **185**, p. 1747–1758 (2014). ISSN 0010-4655. https://www.sciencedirect.com/science/article/pii/S0010465514000484. 18, 19

[88] A. Togo, L. Chaput & I. Tanaka; "Distributions of phonon lifetimes in Brillouin zones"; Phys. Rev. B **91**, p. 094 306 (2015). 18, 19

[89] R. Peierls; "Zur kinetischen theorie der wärmeleitung in kristallen"; Annalen der Physik **395**, p. 1055–1101 (1929). 18

[90] M. Omini & A. Sparavigna; "An iterative approach to the phonon Boltzmann equation in the theory of thermal conductivity"; Physica B: Condensed Matter **212**, p. 101–112 (1995). 19

[91] P. Klemens; "The thermal conductivity of dielectric solids at low temperatures (theoretical)"; Proceedings of the Royal Society of London. Series A. Mathematical and Physical Sciences **208**, p. 108–133 (1951). 19

[92] J. M. Ziman; *Electrons and Phonons* (Oxford University Press) (1960). 19

[93] T. Feng, L. Lindsay & X. Ruan; "Four-phonon scattering significantly reduces intrinsic thermal conductivity of solids"; Phys. Rev. B **96**, p. 161 201 (2017). https://link.aps.org/doi/10.1103/PhysRevB.96.161201. 19

[94] L. Lindsay, C. Hua, X. Ruan & S. Lee; "Survey of ab initio phonon thermal transport"; Materials Today Physics **7**, p. 106–120 (2018). ISSN 2542-5293. https://www.sciencedirect.com/science/article/pii/S254252931830141X. 19

[95] L. Lindsay, A. Katre, A. Cepellotti & N. Mingo; "Perspective on ab initio phonon thermal transport"; Journal of Applied Physics **126**, p. 050 902 (2019). ISSN 0021-8979. https://doi.org/10.1063/1.5108651; https://pubs.aip.org/aip/jap/article-pdf/doi/10.1063/1.5108651/14853757/050902_1_online.pdf. 19

[96] T. Tadano, Y. Gohda & S. Tsuneyuki; "Anharmonic force constants extracted from first-principles molecular dynamics: applications to heat transfer simulations"; Journal of Physics: Condensed Matter **26**, p. 225 402 (2014). 19, 20, 25, 41, 54

[97] Z. Zhang & R. M. Wentzcovitch; "Ab initio anharmonic thermodynamic properties of cubic Ca Si O 3 perovskite"; Physical Review B **103**, p. 104 108 (2021). 21

[98] Y. Lu, T. Sun & D.-B. Zhang; "Lattice anharmonicity, phonon dispersion, and thermal conductivity of PbTe studied by the phonon quasiparticle approach"; Phys. Rev. B **97**, p. 174 304 (2018). https://link.aps.org/doi/10.1103/PhysRevB.97.174304. 21

[99] Y. Lu, F.-w. Zheng, Y. Yang, P. Zhang & D.-B. Zhang; "Phase stabilities of *Cmcm* and *Pnma* SnSe studied by phonon quasiparticle approach"; Phys. Rev. B **100**, p. 054 304 (2019). https://link.aps.org/doi/10.1103/PhysRevB.100.054304. 21

[100] A. Pereverzev & T. D. Sewell; "Obtaining the Hessian from the force covariance matrix: Application to crystalline explosives PETN and RDX"; The Journal of Chemical Physics **142**, p. 134 110 (2015). ISSN 0021-9606. 21

[101] M. Martinez, M.-P. Gaigeot, D. Borgis & R. Vuilleumier; "Extracting effective normal modes from equilibrium dynamics at finite temperature"; The Journal of chemical physics **125** (2006). 21

[102] K. Nakano, T. Morresi, M. Casula, R. Maezono & S. Sorella; "Atomic forces by quantum Monte Carlo: Application to phonon dispersion calculations"; Phys. Rev. B **103**, p. L121 110 (2021). https://link.aps.org/doi/10.1103/PhysRevB.103.L121110. 22

[103] N. Antolin, O. D. Restrepo & W. Windl; "Fast free-energy calculations for unstable high-temperature phases"; Phys. Rev. B **86**, p. 054 119 (2012). https://link.aps.org/doi/10.1103/PhysRevB.86.054119. 22

[104] L. Monacelli, R. Bianco, M. Cherubini, M. Calandra, I. Errea & F. Mauri; "The stochastic self-consistent harmonic approximation: calculating vibrational properties of materials with full quantum and anharmonic effects"; Journal of Physics: Condensed Matter **33**, p. 363 001 (2021). 23

[105] F. Bottin, J. Bieder & J. Bouchet; "A-TDEP: temperature dependent effective potential for ABINIT–lattice dynamic properties including anharmonicity"; Computer Physics Communications **254**, p. 107 301 (2020). 25

[106] O. Hellman, P. Steneteg, I. A. Abrikosov & S. I. Simak; "Temperature dependent effective potential method for accurate free energy calculations of solids"; Physical Review B **87**, p. 104 111 (2013). 25

[107] O. Hellman & I. A. Abrikosov; "Temperature-dependent effective third-order interatomic force constants from first principles"; Physical Review B **88**, p. 144 301 (2013). 25, 70

[108] D. West & S. Estreicher; "First-principles calculations of vibrational lifetimes and decay channels: Hydrogen-related modes in Si"; Physical review letters **96**, p. 115 504 (2006). 26

[109] Grosso & Pastori Parravicini; *Solid State Physics* (Elsevier) (2000). 28

[110] W. Cochran & R. Cowley; "Dielectric constants and lattice vibrations"; Journal of Physics and Chemistry of Solids **23**, p. 447–450 (1962). 30, 68

[111] X. Gonze, J.-C. Charlier, D. Allan & M. Teter; "Interatomic force constants from first principles: The case of $\alpha$-quartz"; Physical Review B **50**, p. 13 035 (1994). 30

[112] P. Giannozzi, S. De Gironcoli, P. Pavone & S. Baroni; "Ab initio calculation of phonon dispersions in semiconductors"; Physical Review B **43**, p. 7231 (1991). 30

[113] M. Royo, K. R. Hahn & M. Stengel; "Using high multipolar orders to reconstruct the sound velocity in piezoelectrics from lattice dynamics"; Physical Review Letters **125**, p. 217 602 (2020). 30, 70

[114] J.-J. Zhou, O. Hellman & M. Bernardi; "Electron-phonon scattering in the presence of soft modes and electron mobility in SrTiO 3 perovskite from first principles"; Physical review letters **121**, p. 226 603 (2018). 30, 60

[115] F. Zhou, B. Sadigh, D. **A**berg, Y. Xia, V. Ozoliņš *et al.*; "Compressive sensing lattice dynamics. II. Efficient phonon calculations and long-range interactions"; Physical Review B **100**, p. 184 309 (2019). 30

[116] P. Giannozzi, S. Baroni, N. Bonini, M. Calandra, R. Car, C. Cavazzoni, D. Ceresoli, G. L. Chiarotti, M. Cococcioni, I. Dabo, A. Dal Corso, S. de Gironcoli, S. Fabris, G. Fratesi, R. Gebauer, U. Gerstmann, C. Gougoussis, A. Kokalj, M. Lazzeri, L. Martin-Samos, N. Marzari, F. Mauri, R. Mazzarello, S. Paolini, A. Pasquarello, L. Paulatto, C. Sbraccia, S. Scandolo, G. Sclauzero, A. P. Seitsonen, A. Smogunov, P. Umari & R. M. Wentzcovitch; "QUANTUM ESPRESSO: a modular and open-source software project for quantum simulations of materials"; Journal of Physics: Condensed Matter **21**, p. 395 502 (19pp) (2009)http://www.quantum-espresso.org. 31, 45, 53

[117] P. Giannozzi, O. Andreussi, T. Brumme, O. Bunau, M. B. Nardelli, M. Calandra, R. Car, C. Cavazzoni, D. Ceresoli, M. Cococcioni *et al.*; "Advanced capabilities for materials modelling with Quantum ESPRESSO"; Journal of Physics: Condensed Matter **29**, p. 465 901 (2017). 31, 60

[118] D. W. Marquardt; "An Algorithm for Least-Squares Estimation of Nonlinear Parameters"; Journal of the Society for Industrial and Applied Mathematics **11**, p. 431–441 (1963). 32

[119] C. Bouillaguet; "Personal commucation on upraged LMDIF algorithm"; Sorbonne Université, CNRS, LIP6, F-75005 Paris, France (2022). 32

[120] S. G. Moustafa, A. J. Schultz & D. A. Kofke; "Effects of thermostatting in molecular dynamics on anharmonic properties of crystals: Application to fcc Al at high pressure and temperature"; The Journal of chemical physics **149**, p. 124 109 (2018). 38

[121] K. Esfarjani, G. Chen & H. T. Stokes; "Heat transport in silicon from first-principles calculations"; Physical Review B **84**, p. 085 204 (2011). 39

[122] Z. Zhang, D.-B. Zhang, T. Sun & R. M. Wentzcovitch; "phq: A Fortran code to compute phonon quasiparticle properties and dispersions"; Computer Physics Communications **243**, p. 110–120 (2019). 41

[123] T. Hastie, R. Tibshirani, J. H. Friedman & J. H. Friedman; *The elements of statistical learning: data mining, inference, and prediction*; tome 2 (Springer) (2009). 41

[124] A. Glensk, B. Grabowski, T. Hickel & J. Neugebauer; "Understanding anharmonicity in fcc materials: From its origin to ab initio strategies beyond the quasiharmonic approximation"; Physical review letters **114**, p. 195 901 (2015). 45

[125] D. J. Adams, L. Wang, G. Steinle-Neumann, D. Passerone & S. V. Churakov; "Anharmonic effects on the dynamics of solid aluminium from ab initio simulations"; Journal of Physics: Condensed Matter **33**, p. 175 501 (2021). 45

[126] V. Ladygin, P. Y. Korotaev, A. Yanilkin & A. Shapeev; "Lattice dynamics simulation using machine learning interatomic potentials"; Computational Materials Science **172**, p. 109 333 (2020). 45

[127] D. Vanderbilt; "Soft self-consistent pseudopotentials in a generalized eigenvalue formalism"; Physical review B **41**, p. 7892 (1990). 45, 53, 60

[128] J. P. Perdew, K. Burke & M. Ernzerhof; "Generalized gradient approximation made simple"; Physical review letters **77**, p. 3865 (1996). 45, 53, 60

[129] P. Giannozzi, O. Andreussi, T. Brumme, O. Bunau, M. B. Nardelli, M. Calandra, R. Car, C. Cavazzoni, D. Ceresoli, M. Cococcioni, N. Colonna, I. Carnimeo, A. D. Corso, S. de Gironcoli, P. Delugas, R. A. D. Jr, A. Ferretti, A. Floris, G. Fratesi, G. Fugallo, R. Gebauer, U. Gerstmann, F. Giustino, T. Gorni, J. Jia, M. Kawamura, H.-Y. Ko, A. Kokalj, E. Küçükbenli, M. Lazzeri, M. Marsili, N. Marzari, F. Mauri, N. L. Nguyen, H.-V. Nguyen, A. O. de-la Roza, L. Paulatto, S. Poncé, D. Rocca, R. Sabatini, B. Santra, M. Schlipf, A. P. Seitsonen, A. Smogunov, I. Timrov, T. Thonhauser, P. Umari, N. Vast, X. Wu & S. Baroni; "Advanced capabilities for materials modelling with QUANTUM ESPRESSO"; Journal of Physics: Condensed Matter **29**, p. 465 901 (2017)http://stacks.iop.org/0953-8984/29/i=46/a=465901. 45, 53

[130] H. J. Monkhorst & J. D. Pack; "Special points for Brillouin-zone integrations"; Physical review B **13**, p. 5188 (1976). 45, 53, 60

[131] N. Marzari, D. Vanderbilt, A. De Vita & M. Payne; "Thermal contraction and disordering of the Al (110) surface"; Physical review letters **82**, p. 3296 (1999). 45, 53

[132] G. Grimvall, B. Magyari-Köpe, V. Ozoliņš & K. A. Persson; "Lattice instabilities in metallic elements"; Reviews of Modern Physics **84**, p. 945 (2012). 53, 54

[133] S. Anzellini, F. m. c. Bottin, J. Bouchet & A. Dewaele; "Phase transitions and equation of state of zirconium under high pressure"; Phys. Rev. B **102**, p. 184 105 (2020). https://link.aps.org/doi/10.1103/PhysRevB.102.184105. 53

[134] A. Ohtomo & H. Hwang; "A high-mobility electron gas at the LaAlO3/SrTiO3 heterointerface"; Nature **427**, p. 423–426 (2004). 59

[135] K. Otnes, T. Riste, G. Shirane & J. Feder; "Temperature dependence of the soft mode in SrTiO3 above the 105 K transition"; Solid State Communications **9**, p. 1103–1106 (1971). 59, 68

[136] R. X. Yang, J. M. Skelton, E. L. Da Silva, J. M. Frost & A. Walsh; "Assessment of dynamic structural instabilities across 24 cubic inorganic halide perovskites"; The Journal of chemical physics **152** (2020). 59

[137] E. Heifets & V. Trepakov; "Calculations for antiferrodistortive phase of SrTiO3 perovskite: hybrid density functional study"; Journal of Physics: Condensed Matter **18**, p. 4845 (2006). 59

[138] R. Wahl, D. Vogtenhuber & G. Kresse; "SrTiO 3 and BaTiO 3 revisited using the projector augmented wave method: Performance of hybrid and semilocal functionals"; Physical Review B **78**, p. 104 116 (2008). 59, 64

[139] X. He, D. Bansal, B. Winn, S. Chi, L. Boatner & O. Delaire; "Anharmonic eigenvectors and acoustic phonon disappearance in quantum paraelectric SrTiO3"; Physical review letters **124**, p. 145 901 (2020). 59, 63

[140] Q. Wang, Z. Zeng & Y. Chen; "Revisiting phonon transport in perovskite SrTiO 3: Anharmonic phonon renormalization and four-phonon scattering"; Physical Review B **104**, p. 235 205 (2021). 59, 60

[141] J. Haeni, P. Irvin, W. Chang, R. Uecker, P. Reiche, Y. Li, S. Choudhury, W. Tian, M. Hawley, B. Craigo *et al.*; "Room-temperature ferroelectricity in strained SrTiO3"; Nature **430**, p. 758–761 (2004). 59

[142] H. Unoki & T. Sakudo; "Electron spin resonance of Fe3+ in SrTiO3 with special reference to the 110 K phase transition"; Journal of the Physical Society of Japan **23**, p. 546–552 (1967). 59

[143] N. Sai & D. Vanderbilt; "First-principles study of ferroelectric and antiferrodistortive instabilities in tetragonal $SrTiO_3$"; Phys. Rev. B **62**, p. 13 942–13 950 (2000). https://link.aps.org/doi/10.1103/PhysRevB.62.13942. 59

[144] C. Lasota, C.-Z. Wang, R. Yu & H. Krakauer; "Ab initio linear response study of SrTiO3"; Ferroelectrics **194**, p. 109–118 (1997). https://doi.org/10.1080/00150199708016086. 59

[145] R. A. Evarestov, E. Blokhin, D. Gryaznov, E. A. Kotomin & J. Maier; "Phonon calculations in cubic and tetragonal phases of $SrTiO_3$: A comparative LCAO and plane-wave study"; Phys. Rev. B **83**, p. 134 108 (2011). https://link.aps.org/doi/10.1103/PhysRevB.83.134108. 60

[146] P. Giannozzi, S. Baroni, N. Bonini, M. Calandra, R. Car, C. Cavazzoni, D. Ceresoli, G. L. Chiarotti, M. Cococcioni, I. Dabo *et al.*; "QUANTUM

ESPRESSO: a modular and open-source software project for quantum simulations of materials"; Journal of physics: Condensed matter **21**, p. 395 502 (2009). 60

[147] D. Hamann; "Optimized norm-conserving Vanderbilt pseudopotentials"; Physical Review B **88**, p. 085 117 (2013). 60

[148] J. P. Perdew, A. Ruzsinszky, G. I. Csonka, O. A. Vydrov, G. E. Scuseria, L. A. Constantin, X. Zhou & K. Burke; "Restoring the density-gradient expansion for exchange in solids and surfaces"; Physical review letters **100**, p. 136 406 (2008). 60

[149] G. Fugallo, M. Lazzeri, L. Paulatto & F. Mauri; "Ab initio variational approach for evaluating lattice thermal conductivity"; Phys. Rev. B **88**, p. 045 430 (2013). https://link.aps.org/doi/10.1103/PhysRevB.88.045430. 60

[150] D. S. Kim, O. Hellman, N. Shulumba, C. N. Saunders, J. Y. Y. Lin, H. L. Smith, J. E. Herriman, J. L. Niedziela, D. L. Abernathy, C. W. Li & B. Fultz; "Temperature-dependent phonon lifetimes and thermal conductivity of silicon by inelastic neutron scattering and ab initio calculations"; Phys. Rev. B **102**, p. 174 311 (2020). https://link.aps.org/doi/10.1103/PhysRevB.102.174311. 65

[151] K. Kunc & R. Martin; "Ab initio calculation of phonon spectra"; ed. JT Devreese, VE Van Doren and PE Van Camp, Plenum Press, New York p. 65 (1983). 66

[152] Q. Wang, Z. Zeng & Y. Chen; "Revisiting phonon transport in perovskite SrTiO 3: Anharmonic phonon renormalization and four-phonon scattering"; Physical Review B **104**, p. 235 205 (2021). 66

[153] B. Fu, G. Tang & A. J. McGaughey; "Finite-temperature force constants are essential for accurately predicting the thermal conductivity of rutile TiO 2"; Physical Review Materials **6**, p. 015 401 (2022). 70

[154] Y. Wang, J. Lv, L. Zhu & Y. Ma; "CALYPSO: A method for crystal structure prediction"; Computer Physics Communications **183**, p. 2063–2070 (2012). ISSN 0010-4655. https://www.sciencedirect.com/science/article/pii/S0010465512001762. 71

[155] C. J. Pickard & R. J. Needs; "Ab initio random structure searching"; Journal of Physics: Condensed Matter **23**, p. 053 201 (2011). https://dx.doi.org/10.1088/0953-8984/23/5/053201. 71

[156] M. Bom & T. Von Karman; "Uber schwingungen in Raumgittern"; Physik. Z **13**, p. 297–309 (1912).

[157] W. Kohn & L. J. Sham; "Self-consistent equations including exchange and correlation effects"; Physical review **140**, p. A1133 (1965).

[158] W. Kohn & L. J. Sham; "Self-Consistent Equations Including Exchange and Correlation Effects"; Phys. Rev. **140**, p. A1133–A1138 (1965). https://link.aps.org/doi/10.1103/PhysRev.140.A1133.

[159] I. Timrov, N. Marzari & M. Cococcioni; "Hubbard parameters from density-functional perturbation theory"; Physical Review B **98**, p. 085 127 (2018).

[160] S. Labidi, J. Zeroual, M. Labidi, K. Klaa & R. Bensalem; "Structural electronic and optical properties of MgO, CaO and SrO binary compounds: comparison study"; **257**, p. 123–126 (2017).

[161] D. A. Andersson, S. I. Simak, B. Johansson, I. A. Abrikosov & N. V. Skorodumova; "Modeling of CeO2, Ce2O3, and CeO2-x in the LDA+U formalism"; Phys. Rev. B **75**, p. 035 109 (2007). https://link.aps.org/doi/10.1103/PhysRevB.75.035109.

[162] V. I. Anisimov, J. Zaanen & O. K. Andersen; "Band theory and Mott insulators: Hubbard U instead of Stoner I"; Physical Review B **44**, p. 943 (1991).

[163] M. Ernzerhof & G. E. Scuseria; "Assessment of the Perdew–Burke–Ernzerhof exchange-correlation functional"; The Journal of Chemical Physics **110**, p. 5029–5036 (1999). https://doi.org/10.1063/1.478401.

[164] Y. Zhao & D. G. Truhlar; "Calculation of semiconductor band gaps with the M06-L density functional"; The Journal of chemical physics **130**, p. 074 103 (2009).

[165] G. Kotliar, S. Y. Savrasov, K. Haule, V. S. Oudovenko, O. Parcollet & C. Marianetti; "Electronic structure calculations with dynamical mean-field theory"; Reviews of Modern Physics **78**, p. 865 (2006).

[166] H. Jiang, R. I. Gomez-Abal, P. Rinke & M. Scheffler; "First-principles modeling of localized d states with the G W@ LDA+ U approach"; Physical Review B **82**, p. 045 108 (2010).

[167] A. Togo & I. Tanaka; "First principles phonon calculations in materials science"; Scripta Materialia **108**, p. 1–5 (2015).

[168] H. J. Kulik; "Perspective: Treating electron over-delocalization with the DFT+ U method"; The Journal of chemical physics **142**, p. 240 901 (2015).

[169] R. Whited, C. J. Flaten & W. Walker; "Exciton thermoreflectance of MgO and CaO"; Solid State Communications **13**, p. 1903–1905 (1973).

[170] J. E. Jaffe, J. A. Snyder, Z. Lin & A. C. Hess; "LDA and GGA calculations for high-pressure phase transitions in ZnO and MgO"; Physical Review B **62**, p. 1660 (2000).

[171] S. Labidi, J. Zeroual, M. Labidi, K. Klaa & R. Bensalem; "Structural electronic and optical properties of MgO, CaO and SrO binary compounds: comparison study"; dans "Solid State Phenomena", , tome 257p. 123–126 (Trans Tech Publ) (2017).

[172] A. R. Oganov, M. J. Gillan & G. D. Price; "Ab initio lattice dynamics and structural stability of MgO"; The Journal of chemical physics **118**, p. 10 174–10 182 (2003).

[173] K. F. Garrity, J. W. Bennett, K. M. Rabe & D. Vanderbilt; "Pseudopotentials for high-throughput DFT calculations"; Computational Materials Science **81**, p. 446–452 (2014).

[174] A. Debernardi, S. Baroni & E. Molinari; "Anharmonic phonon lifetimes in semiconductors from density-functional perturbation theory"; Physical review letters **75**, p. 1819 (1995).

[175] T. Taniuchi & T. Tsuchiya; "The melting points of MgO up to 4 TPa predicted based on ab initio thermodynamic integration molecular dynamics"; Journal of Physics: Condensed Matter **30**, p. 114 003 (2018).

[176] B. Himmetoglu, A. Floris, S. De Gironcoli & M. Cococcioni; "Hubbard-corrected DFT energy functionals: The LDA+ U description of correlated systems"; International Journal of Quantum Chemistry **114**, p. 14–49 (2014).

[177] F. Zhou, W. Nielson, Y. Xia & V. Ozoliņš; "Lattice Anharmonicity and Thermal Conductivity from Compressive Sensing of First-Principles Calculations"; Phys. Rev. Lett. **113**, p. 185 501 (2014). https://link.aps.org/doi/10.1103/PhysRevLett.113.185501.

[178] A. P. Bartók, J. Kermode, N. Bernstein & G. Csányi; "Machine learning a general-purpose interatomic potential for silicon"; Physical Review X **8**, p. 041 048 (2018).

[179] M. Cococcioni & S. De Gironcoli; "Linear response approach to the calculation of the effective interaction parameters in the LDA+ U method"; Physical Review B **71**, p. 035 105 (2005).

[180] A. Floris, S. de Gironcoli, E. K. U. Gross & M. Cococcioni; "Vibrational properties of MnO and NiO from DFT $+U$-based density functional perturbation theory"; Phys. Rev. B **84**, p. 161 102 (2011). https://link.aps.org/doi/10.1103/PhysRevB.84.161102.

[181] Y. Sun, M. Cococcioni & R. M. Wentzcovitch; "LDA $+U_{sc}$ calculations of phase relations in FeO"; Phys. Rev. Materials **4**, p. 063 605 (2020). https://link.aps.org/doi/10.1103/PhysRevMaterials.4.063605.

[182] F. Eriksson, E. Fransson & P. Erhart; "The Hiphive Package for the Extraction of High-Order Force Constants by Machine Learning"; Advanced Theory and Simulations **2**, p. 1800 184 (2019).

[183] F. Knoop, T. A. R. Purcell, M. Scheffler & C. Carbogno; "Anharmonicity measure for materials"; Phys. Rev. Materials **4**, p. 083 809 (2020). https://link.aps.org/doi/10.1103/PhysRevMaterials.4.083809.

[184] T. Lanigan-Atkins, S. Yang, J. L. Niedziela, D. Bansal, A. F. May, A. A. Puretzky, J. Lin, D. M. Pajerowski, T. Hong, S. Chi *et al.*; "Extended anharmonic collapse of phonon dispersions in SnS and SnSe"; Nature communications **11**, p. 1–9 (2020).

[185] W. Cochran & R. Cowley; "Dielectric constants and lattice vibrations"; Journal of Physics and Chemistry of Solids **23**, p. 447–450 (1962).

[186] Z. Han, X. Yang, W. Li, T. Feng & X. Ruan; "FourPhonon: An extension module to ShengBTE for computing four-phonon scattering rates and thermal conductivity"; Computer Physics Communications **270**, p. 108 179 (2022).

[187] A. Togo & I. Tanaka; "First principles phonon calculations in materials science"; Scripta Materialia **108**, p. 1–5 (2015). ISSN 1359-6462. https://www.sciencedirect.com/science/article/pii/S1359646215003127.

[188] T. Feng & X. Ruan; "Quantum mechanical prediction of four-phonon scattering rates and reduced thermal conductivity of solids"; Physical Review B **93**, p. 045 202 (2016).

[189] G. Grimvall, B. Magyari-Köpe, V. Ozoliņš & K. A. Persson; "Lattice instabilities in metallic elements"; Reviews of Modern Physics **84**, p. 945 (2012).

[190] D. Marx & J. Hutter; *Ab initio molecular dynamics: basic theory and advanced methods* (Cambridge University Press) (2009).

[191] M. Ceriotti, M. Parrinello, T. E. Markland & D. E. Manolopoulos; "Efficient stochastic thermostatting of path integral molecular dynamics"; The Journal of chemical physics **133**, p. 124 104 (2010).

[192] M. Ceriotti, D. E. Manolopoulos & M. Parrinello; "Accelerating the convergence of path integral dynamics with a generalized Langevin equation"; The Journal of chemical physics **134**, p. 084 104 (2011).

[193] X. Gonze; "Adiabatic density-functional perturbation theory"; Physical Review A **52**, p. 1096 (1995).

[194] A. Debernardi, S. Baroni & E. Molinari; "Anharmonic Phonon Lifetimes in Semiconductors from Density-Functional Perturbation Theory"; Phys. Rev. Lett. **75**, p. 1819–1822 (1995). https://link.aps.org/doi/10.1103/PhysRevLett.75.1819.

[195] M. Ceriotti, G. Bussi & M. Parrinello; "Nuclear quantum effects in solids using a colored-noise thermostat"; Physical review letters **103**, p. 030 603 (2009).

[196] J. J. More, B. S. Garbow & K. E. Hillstrom; "User guide for MINPACK-1. [In FORTRAN]"; (1980). https://www.osti.gov/biblio/6997568.

[197] G. Deinzer, G. Birner & D. Strauch; "Ab initio calculation of the linewidth of various phonon modes in germanium and silicon"; Phys. Rev. B **67**, p. 144 304 (2003). https://link.aps.org/doi/10.1103/PhysRevB.67.144304.

[198] F. Ercolessi & J. B. Adams; "Interatomic Potentials from First-Principles Calculations: The Force-Matching Method"; Europhysics Letters **26**, p. 583 (1994). https://dx.doi.org/10.1209/0295-5075/26/8/005.

**Ibrahim Buba GARBA** **5/09/2023**

## Sujet : Caractérisation ab initio des materiaux anharmoniques

**Résumé** : La prédiction précise des propriétés thermodynamiques et de transport des matériaux à partir des premiers principes nécessite une compréhension de l'anharmonicité résultant de l'interaction phonon-phonon. L'approximation quasiharmonique standard néglige la dépendance explicite de la température des phonons et est invalide à haute température, en particulier près d'une transition de phase, ou même à basse température si le profil d'énergie est peu profond ou si la nature quantique des noyaux ne peut être ignorée, ce qui justifie la nécessité de méthodes anharmoniques. De plus, le traitement perturbatif de l'anharmonicité peut être problématique en présence de phonons imaginaires, sans état fondamental approprié sur lequel une expansion perturbative peut être construite. Nous présentons une méthode de calcul des phonons anharmoniques dans laquelle la seule hypothèse semble être la forme des matrices dynamiques. À partir d'une géométrie cristalline donnée et d'une grille de q-points dans la zone irréductible de Brillouin, nous définissons une matrice dynamique d'essai à l'aide d'une base orthonormée symétrisée dont les valeurs peuvent être générées aléatoirement. Les matrices dynamiques d'essai sont optimisées en s'adaptant à la dynamique moléculaire ab-initio standard échantillonnée des forces et à la dynamique de Langevin, sur la base de la méthode du potentiel effectif dépendant de la température. A titre d'exemple, nous l'appliquons pour étudier la renormalisation anharmonique des phonons dans des matériaux faiblement et fortement anharmoniques, reproduisant l'effet de la température sur les fréquences des phonons, la stabilisation des phases à haute température dans les métaux et la transition de phase en ferroélectrique, en bon accord avec l'expérience.

**Mots clés** : l'anharmonicité, lattice dynamics, phonons, ab initio, transition de phase, modélisation des matériaux

## Subject : Ab initio Characterization of Anharmonic Materials

**Abstract**: Accurate prediction of thermodynamic and transport properties of materials from first principles requires an understanding of anharmonicity resulting from phonon-phonon interaction. The standard quasiharmonic approximation neglect explicit temperature dependence of phonons and is invalid at high temperature, especially near a phase transition, or even at low temperatures if the energy profile is shallow or if the quantum nature of nuclei cannot be disregarded, which warrants the need for anharmonic methods. Furthermore, the perturbative treatment of anharmonicity can be problematic in the presence of imaginary phonons, with no suitable ground state upon which a perturbative expansion can be built. We present a method of computing anharmonic phonons in which the only assumption appears to be the form of the dynamical matrices. Starting from a given crystal geometry and a grid of q-points in the irreducible Brillouin zone, we define a trial dynamical matrix using an orthonormal symmetrized basis whose values can be randomly generated. The trial dynamical matrices are optimized by fitting to forces sampled from standard ab initio molecular dynamics and with Langevin dynamics, based on the temperature-dependent effective potential method. By way of example, we apply it to study anharmonic phonon renormalization in weakly and strongly anharmonic materials, reproducing the temperature effect on phonon frequencies, stabilization of high-temperature phases in metals, and phase transition in ferroelectrics, in good agreement with the experiment.

**Keywords** : Lattice dynamics, phonons, anharmonicity, phase transition, ab initio, materials modelling